



Thick turbulent gas disks with magnetocentrifugal winds in active galactic nuclei

Bernd Vollmer, Marc Schartmann, Léonard Burtscher, Frédéric Marin,
Sebastian Hönig, Richard Davies, René Goosmann

► To cite this version:

Bernd Vollmer, Marc Schartmann, Léonard Burtscher, Frédéric Marin, Sebastian Hönig, et al.. Thick turbulent gas disks with magnetocentrifugal winds in active galactic nuclei: Model infrared emission and optical polarization. *Astronomy and Astrophysics - A&A*, 2018, 615, pp.A164. 10.1051/0004-6361/201731133 . hal-02919306

HAL Id: hal-02919306

<https://hal.science/hal-02919306>

Submitted on 22 Aug 2020

HAL is a multi-disciplinary open access archive for the deposit and dissemination of scientific research documents, whether they are published or not. The documents may come from teaching and research institutions in France or abroad, or from public or private research centers.

L'archive ouverte pluridisciplinaire **HAL**, est destinée au dépôt et à la diffusion de documents scientifiques de niveau recherche, publiés ou non, émanant des établissements d'enseignement et de recherche français ou étrangers, des laboratoires publics ou privés.

Thick turbulent gas disks with magnetocentrifugal winds in active galactic nuclei

Model infrared emission and optical polarization

B. Vollmer¹, M. Schartmann^{2,3,4}, L. Burtscher^{2,5}, F. Marin¹, S. Hönig⁶, R. Davies², and R. Goosmann¹

¹ Observatoire astronomique de Strasbourg, Université de Strasbourg, CNRS, UMR 7550, 11 rue de l'Université,
67000 Strasbourg, France
e-mail: Bernd.Vollmer@astro.unistra.fr

² Max-Planck-Institut für extraterrestrische Physik, Postfach 1312, Gießenbachstr., 85741 Garching, Germany

³ University Observatory Munich, Scheinerstraße 1, 81679 München, Germany

⁴ Centre for Astrophysics and Supercomputing, Swinburne University of Technology, PO Box 218, Hawthorn,
Victoria 3122, Australia

⁵ Sterrewacht Leiden, Universiteit Leiden, Niels-Bohr-Weg 2, 2300 CA Leiden, The Netherlands

⁶ Department of Physics and Astronomy, University of Southampton, Southampton SO17 1BJ, UK

Received 9 May 2017 / Accepted 16 March 2017

ABSTRACT

Infrared high-resolution imaging and interferometry show that the dust distribution is frequently elongated along the polar direction of an AGN. In addition, interferometric mm line observations have revealed a bipolar outflow in a direction nearly perpendicular to the nuclear disk. To explain these findings, we developed a model scenario for the inner ~ 30 pc of an AGN. The structure of the gas within this region is entirely determined by the gas inflow from larger scales. We assumed a rotating thick gas disk between about one and ten parsec. External gas accretion adds mass and injects energy via gas compression into this gas disk and drives turbulence. We extended the description of a massive turbulent thick gas disk developed in a recent paper by adding a magnetocentrifugal wind. Our disks are assumed to be strongly magnetized via equipartition between the turbulent gas pressure and the energy density of the magnetic field. In a second step, we built 3D density cubes based on the analytical model, illuminated them with a central source, and made radiative transfer calculations. In a third step, we calculated mid-infrared (MIR) visibility amplitudes and compared them to available interferometric observations. We show that magnetocentrifugal winds starting from a thin and thick gas disk are viable in active galaxy centers. The magnetic field associated with this thick gas disk plays a major role in driving a magnetocentrifugal wind at a distance of ~ 1 pc from the central black hole. Once the wind is launched, it is responsible for the transport of angular momentum and the gas disk can become thin. A magnetocentrifugal wind is also expected above the thin magnetized gas disk. The structure and outflow rate of this wind is determined by the properties of the thick gas disk. The outflow scenario can account for the elongated dust structures, outer edges of the thin maser disks, and molecular outflows observed in local AGN. The models reproduce the observed terminal wind velocities, the scatter of the MIR – intrinsic X-ray correlation, and point source fractions. An application of the model to the Circinus galaxy and NGC 1068 shows that the infrared spectral energy distribution, available MIR interferometric observations, and optical polarization can be reproduced in a satisfactory way, provided that (i) a puff-up at the inner edge of the thin disk is present and (ii) a local screen with an optical depth of $\tau_V \sim 20$ in form of a local gas filament and/or a warp of the thick disk hide a significant fraction of both nuclei. Our thick disk, wind, thin disk model is thus a promising scenario for local Seyfert galaxies.

Key words. galaxies: active – galaxies: nuclei – galaxies: Seyfert

1. Introduction

The standard paradigm of type 1 and type 2 active galactic nuclei (AGN) postulates that obscuration by circum-nuclear dust in a torus geometry is responsible for the observed dichotomy (see Netzer 2015 for a recent review). In type 1 sources the torus is seen face-on, whereas in type 2 sources it is seen edge-on. The torus unification model has been successful in explaining a number of observations including the detection of polarized broad lines (e.g., Ramos Almeida et al. 2016), the collimation of ionization cones (e.g., Fischer et al. 2013), its correspondence with the fraction of obscured sources (e.g., Maiolino & Rieke 1995), and the overall spectral energy distribution (SED) from the near-to far-infrared (e.g., Netzer et al. 2016). However, it is not clear at which distance the obscuring material is sitting and which

physical configuration it has. Whereas Elitzur (2006) prefers a slow wind as the torus that is located very close to the central black hole near the broad line region, Vollmer et al. (2008) advocate a thick accretion disk at a distance of several parsec. Additional obscuration by galactic structure at kpc scales cannot be excluded either (e.g., Matt 2000; Prieto et al. 2014).

VLT SINFONI H_2 (Hicks et al. 2009) and interferometric CO/HCN/HCO⁺ observations (Sani et al. 2012; Lin et al. 2016; García-Burillo et al. 2016; Gallimore et al. 2016) show that there are massive rotating thick molecular gas disks sitting at distances of 10–50 pc from the central black hole. These gas disks contain dust which obscures the central engine if seen edge-on.

On the other hand, VLBI radio continuum observations of nearby AGN led to the discovery of thin molecular maser disks at distance below ~ 1 pc (Greenhill et al. 1995, 1996, 2003). To

insure velocity coherence, the velocity dispersion of the disk must be low, meaning that the disk has to be thin. The massive thick molecular gas disk thus apparently becomes thin at distances around ~ 1 pc from the central black hole (Greenhill 1998; Fig. 8 of Greenhill et al. 2003).

A challenge to the unification theory is that type 1 and type 2 AGNs essentially follow the same mid-infrared (MIR) – intrinsic X-ray relation from low to high luminosities (e.g., Asmus et al. 2015). Much of the uncertainty about the geometry and dynamics of the torus comes from the fact that the circum-nuclear dust in AGNs is usually unresolved in single-dish high-resolution images – a deficiency that infrared interferometry has partly solved in the last decade (see, e.g., Burtcher et al. 2013, 2016). MIR interferometric observations of nearby AGN reveal the geometry of warm (~ 300 K) dust at scales of a few tenths to a few parsec. The best studied cases are the Circinus galaxy (Tristram et al. 2014) and NGC 1068 (López-Gonzaga et al. 2014). Moreover, detailed interferometric MIR observations of NGC 3783 (Hönig et al. 2013) and NGC 424 (Hönig et al. 2012) are available. These observations revealed that the bulk of the MIR emission comes from extended elongated structures along the polar axis of the AGN, in other words, in the direction of the ionization cone. In the case of the Circinus galaxy and NGC 1068 thin elongated structures with the same geometry as the maser disks are observed in addition to the polar extended emission. Most recently, López-Gonzaga et al. (2016) found that five of the seven MIR structures in local AGNs observed with MIR interferometry are significantly elongated, all in polar direction. Polar dust emission with orientation consistent with that found by interferometry was also observed in high-resolution MIR imaging (Asmus et al. 2016). The fact that the polar emission, which is less prone to geometrical extinction, dominates the total MIR emission is consistent with the tight MIR – X-ray relation (Hönig & Kishimoto 2017).

The most appealing physical configuration which can explain the molecular line, maser, and MIR observations is a structure containing three components: (i) an outer thick gas disk which is observed in molecular lines (HCN, HCO⁺), (ii) an inner thin disk which is the source of maser emission, and (iii) a polar wind which is responsible for the bulk of the MIR emission. This wind might be even molecular as advocated by Gallimore et al. (2016) for NGC 1068 who interpreted the velocities of maser clouds that did not follow the overall rotation pattern as a disk outflow.

Our view of an AGN is from outside in. A certain amount of gas is located at scales of approximately one to a few tens of parsecs into which a certain amount of energy is injected by external accretion. This energy injection leads to turbulence which makes the gas disk thick. Since the injection timescale is smaller than the turbulent dissipation timescale, the gas that rotated within ~ 10 pc is adiabatically compressed. The enhanced turbulence leads to overpressured gas clouds that cannot collapse, that is, star formation is suppressed (Vollmer & Davies 2013). The gas mass and turbulent velocity dispersion set the mass accretion rate of the thick gas disk (typically $\sim 1 M_{\odot} \text{ yr}^{-1}$), which is determined by the external mass supply. At a certain radius, the poloidal magnetic fields associated with the thick gas disk are bent outward and a magnetocentrifugal wind is launched (Blandford & Payne 1982). The wind takes angular momentum away from the disk, permitting it to become thin. Mass flux conservation leads to an about two times smaller mass accretion rate of the thin disk compared to the thick gas disk, that is, about half of the thick disk mass accretion rate is expelled by the wind. Further in, a broad line region (BLR) wind is expected (e.g., Gaskell 2009). The final accretion rate onto the central black hole is thus at least

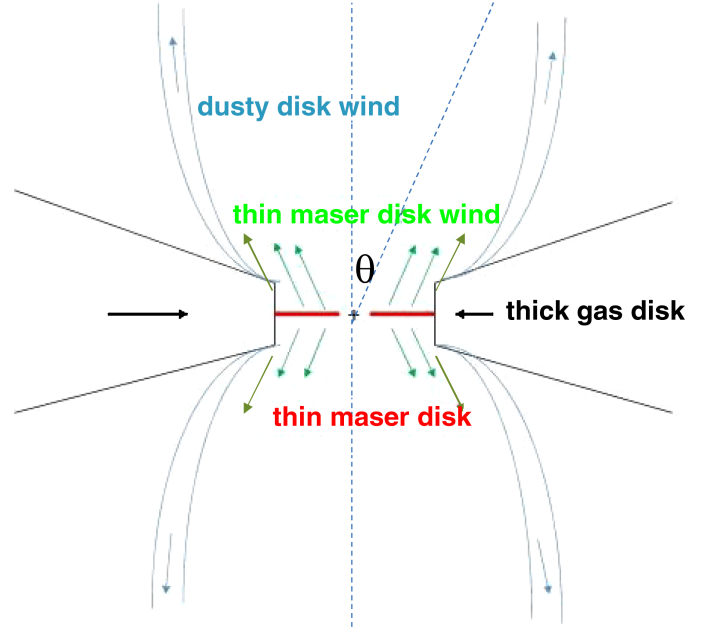


Fig. 1. Schematic ingredients of the model. The dusty disk wind corresponds to the magnetocentrifugal wind. The wind emanates from the thin and thick disks with a half-opening angle θ .

four times smaller than the mass accretion rate of the thick gas disk. This final accretion rate \dot{M}_{final} sets the AGN luminosity.

In this article we elaborate on a simple analytical model which takes into account these three components and links them physically. We note that we are mainly interested in the thick gas disk and the transition between the thick and thin gas disks involving a magnetocentrifugal wind. The detailed geometry of the inner thin gas disk is not subject of this article. The role of radiation pressure, which is not an explicit part of our model, is depicted in Sect. 2.1. The models of the thick and thin gas disks are described in Sects. 2.2 and 2.3, the wind model in Sect. 2.4. The link between the components is explained in Sect. 2.5 and an expression for the critical radius where the wind sets in is given in Sect. 2.6. The model parameters are given in Sect. 2.7. The conditions under which these winds are viable are explored in Sect. 2.8. Their terminal wind speeds are presented in Sect. 2.9. Axisymmetric (Sect. 3) and nonaxisymmetric (Sect. 5.2.3) 3D density distributions are computed and a full radiative transfer model is applied to the model cubes (Sect. 3.2). The model IR luminosities, central extinctions, and SEDs are compared to observations in Sects. 4.1–4.3. To compare our models with MIR interferometric observations, we compute the expected visibilities from the model MIR images (Sect. 5.1). The models are then applied to the Circinus galaxy and NGC 1068 (Sect. 5.2). The influence of our model geometry on the optical polarization is investigated in Sect. 6. Finally, we give our conclusions in Sect. 7.

2. The model

Our analytical model consists of three different structures: (i) a thick turbulent clumpy gas disk, (ii) a magnetocentrifugal wind, and (iii) a thin gas disk (Fig. 1). In addition, it is expected that a wind also emanates from the thin gas disk. The thick gas disk is fed by externally infalling gas. The external mass accretion and energy injection rates are so high that the disk has to increase its viscosity to be able to cope with the gas inflow. By increasing

its viscosity, the disk becomes thick. The poloidal magnetic field is dragged with the radial flow and, eventually bends at an angle of $\sim 30^\circ$ at the radius, where the magnetocentrifugal wind sets in (Blandford & Payne 1982). Since the wind takes over the angular momentum transfer, the gas disk can become thin at smaller radii. We show in Sect. 2.3 that a magnetocentrifugal wind arises naturally from a magnetized thin accretion disk around a massive black hole.

For the radial distribution of the magnetocentrifugal wind, we assumed that the wind starts at the inner edge of the thick disk and continues over the thin maser disk. Radiation pressure pushes the part of the wind which is located well above the thin disk to larger radii, increasing the wind angle with respect to the disk vertical. Potentially this can lead to a more radial or equatorial wind (see, e.g., Fig. 7 of Chan & Krolik 2017). We can only speculate that the subsequent radial bending of vertical magnetic field lines at the inner edge of the thick disk leads to a wind angle that is sufficient for the launching of a magnetocentrifugal wind at this position ($\gtrsim 30^\circ$). Such a bending of the magnetic field lines is plausible, because at the point where the wind is launched above the thick disk the radiation pressure is in approximate equilibrium with the energy density of the magnetic field (see Sect. 2.7). A detailed analysis of this issue is beyond the scope of this article. The existence of a magnetocentrifugal wind is consistent with the finding of Das et al. (2006), that in the narrow line region (NLR) wind of NGC 1068 the outflow velocity cannot be simply accounted for by radiative forces driving the gas clouds.

The wind outflow rate is estimated at the inner edge of the thick gas disk. We thus assumed that it is not much different across the thin maser disk. The physical parameters of the thick disk are determined by the external mass accretion rate, the gas surface density, and the turbulent velocity dispersion. The magnetocentrifugal wind sets in at a radius r_{wind} . At $r < r_{\text{wind}}$ the disk becomes thin, because the wind extracts the angular momentum from the disk making mass accretion possible. The critical radius r_{wind} is set by mass flux conservation:

$$\dot{M}_{\text{thick disk}} - \dot{M}_{\text{wind}} - \dot{M}_{\text{thin disk}} = 0, \quad (1)$$

where $\dot{M}_{\text{thick disk}}$, \dot{M}_{wind} , and $\dot{M}_{\text{thin disk}}$ are the mass accretion rates of the thick accretion disk, the magnetocentrifugal wind, and the thin accretion disk.

2.1. Radiation pressure

Another cause for the onset of a wind is radiation pressure. For an optically thick medium the outward force exerted by radiation is $F = L/c$, where L is the luminosity and c the light speed. If the near-infrared optical depth of the gas τ_{NIR} is higher than unity, the force becomes $F = \tau_{\text{NIR}} L/c$ (e.g., Roth et al. 2012). We assumed that the magnetocentrifugal wind has a hollow cone structure with an optical depth τ_v of a few. The NIR optical depth is thus smaller than unity. The magnetohydrodynamic (MHD) equation of motion of the gas in the presence of radiation pressure is

$$\rho \frac{dv}{dt} = -\rho \nabla \Phi - \nabla p + \frac{1}{4\pi} (\nabla \times \mathbf{B}) \times \mathbf{B} + \frac{L\rho\kappa}{4\pi R^2 c} \quad (2)$$

where \mathbf{B} is the magnetic field, v the gas velocity, ρ the gas density, Φ the gravitational potential, p the gas pressure, and κ the dust absorption coefficient. We assumed that in the wind

region the large-scale magnetic field and thus magnetic tension dominates:

$$\frac{1}{4\pi} (\nabla \times \mathbf{B}) \times \mathbf{B} \sim \frac{1}{4\pi} (\mathbf{B} \cdot \nabla) \mathbf{B}. \quad (3)$$

As stated by Roth et al. (2012), modeling the force from radiation pressure, and predicting by what factor it exceeds L/c , becomes a difficult problem to tackle analytically in the absence of spherical symmetry.

The semianalytic model developed by Everett (2005) includes magnetic acceleration and radiative acceleration of a continuous self-similar wind launched from an accretion disk. In this model the central continuum radiation first encounters a purely magnetocentrifugally accelerated wind, which is referred to as a “shield”. The shield was introduced as a separate component in order to cleanly differentiate the effect of shielding from radiative acceleration; radiative driving of the shield was therefore not considered. Beyond that shield is an optically thin, radiatively and magnetically accelerated wind; the radiation coming from an underlying thin gas disk. Everett (2005) considered radiative acceleration by bound-free (“continuum driving”) and bound-bound (“line driving”). They find that shielding by a magnetocentrifugal wind can increase the efficiency of a radiatively driven wind. For luminosities smaller than a tenth of the Eddington luminosity, magnetic driving dominates the mass outflow rate. Keating et al. (2012) added the continuum opacity of interstellar medium (ISM) dust grains to the model of Everett (2005) and produced IR SEDs for a wide range of parameter space. They found that models with high column densities, Eddington ratios, and black hole masses were able to adequately approximate the general shape and amount of power expected in the IR as observed in a composite of optically luminous Sloan Digital Sky Survey quasars.

Roth et al. (2012) use 3D Monte Carlo radiative transfer calculations to determine the radiation force on dusty gas residing within approximately 30 parsecs from an accreting supermassive black hole. Static smooth and clumpy thick gas disk distributions were considered. In the absence of a coupling between the radiative transfer calculation and a hydrodynamic solver in a time-dependent calculation, they could not determine the dynamics of the gas. Roth et al. (2012) find that these dust-driven winds can carry momentum fluxes of 1–5 times L/c and can correspond to mass-loss rates of 10–100 $M_\odot \text{ yr}^{-1}$ for a $10^8 M_\odot$ black hole radiating at or near its Eddington limit.

Wada (2012) use a 3D, multiphase hydrodynamic model including radiative feedback from the central source, that is, radiation pressure on the dusty gas and the X-ray heating of cold, warm, and hot ionized gas to study the dynamics of a thick gas and dust disk located in the inner 30 pc around the central black hole. Only the radial component of the central radiation flux was considered for radiative heating and pressure. Wada (2012) show that a geometrically and optically thick torus with a biconical outflow ($v_{\text{outflow}} \sim 100 \text{ km s}^{-1}$) can be naturally formed in the central region extending tens of parsecs around a low-luminosity AGN.

Chan & Krolik (2016, 2017) perform 3D, time-dependent radiative magnetohydrodynamics simulations of AGN tori featuring quality radiation transfer and simultaneous evolution of gas and radiation. The simulations solved the magnetohydrodynamics equations simultaneously with the infrared and ultraviolet radiative transfer equations. Their thick gas torus achieved a quasi-steady state lasting for more than an orbit at the inner edge, and potentially for much longer. The associated central wind is propelled by IR and UV radiation. Despite the gas torus

being magnetized, the outflow is not a magnetocentrifugal wind because meandering loops of magnetic fields in the outflow are too weak to exert much force.

The physical model of Dorodnitsyn et al. (2016) describes the time-evolution of a 3D distribution of gas and dust in the gravitational field of a supermassive black hole, adopting radiation hydrodynamics in axial symmetry (2.5D calculations on a uniform cylindrical grid). Radiation input from X-ray and UV illumination was taken into account. Dorodnitsyn et al. (2016) show that in the absence of strong viscosity the conversion of external UV and X-ray into IR radiation becomes important at Eddington ratios in excess of 0.01. Gas located closer to the black hole escapes in the form of a fast thermally driven wind with a characteristic velocity of 100–1000 km s⁻¹. An IR-driven wind exists farther away from the black hole. For times in excess of a few 10⁴ yr, the wind outflow rates are $\dot{M}_{\text{wind}} \lesssim 0.1 M_{\odot} \text{ yr}^{-1}$.

In the following we argue that for our massive, highly turbulent gas disks with strong magnetic fields (under the assumption of energy equipartition between the gas pressure and the energy density of the magnetic field) the magnetocentrifugal outflow rate exceeds that induced by radiation pressure.

The near-infrared optical depth of the wind is much smaller than unity. Thus, the UV luminosity dominates the radiation pressure in a thin layer of column density $N \sim 5 \times 10^{20} \text{ cm}^{-2}$. Radiation pressure will then radially push the gas and magnetic fields in the wind, until the point of equilibrium between the magnetic tension and radiation pressure. This equilibrium sets the wind opening angle, which is defined as twice the angle between the inner edge of the wind and the polar axis. Since we have assumed energy equipartition between the turbulent kinetic energy density and that of the magnetic field, the strength of the polar magnetic field above the thin disk is significantly smaller than that located above the thick gas disk. Radiation pressure exceeds the magnetic pressure in the region above the thin disk, making the wind more radial (equatorial) there. The wind is expected to bend upward at the inner edge of the thick gas disk creating a hollow cone. The observed elongated polar structures in local AGN (Tristram et al. 2014; Hönig et al. 2012, 2013; Asmus et al. 2016) are in favor of a scenario where magnetic tension dominates already at relatively small wind opening angles. Indeed, the comparison of the magnetic pressure in the wind p_B and the radiation pressure p_{rad} (assuming an optically thick medium) at the critical radius r_{wind} (Table 2) in NGC 1068 and Circinus shows that the radiation pressure is comparable to the magnetic pressure at the critical radius where the wind sets in. Moreover, we argue in Sect. 5 that the observed MIR visibilities are consistent with such a homogeneous wind of column densities $N_{\text{wind}} \sim 5 \times 10^{21} \text{ cm}^{-2}$ ($\tau_V \sim 3$, Fig. 6).

Within the thick disk, the NIR optical depth is high and IR radiation pressure has to be taken into account. The condition for a disk in which radiation pressure dominates is given by Chan & Krolik (2016; Eqs. (15) and (29)):

$$\left(\frac{L_{\text{UV}}}{4\pi R^2 c} \right) \times \left(\frac{2C_{\text{UV}}}{1 - C_{\text{IR}}} \right) \sim \rho v_{\text{rot}}^2, \quad (4)$$

where C_{UV} and C_{IR} are the UV and IR covering fractions, ρ the midplane gas density, and v_{rot} the rotation velocity of the thick gas disk. With the assumed wind and disk opening angles (Fig. 5) we set $C_{\text{UV}} = 1 - \cos(70^\circ)$ and $C_{\text{IR}} = 1 - \cos(30^\circ)$. Furthermore, the gas density is given by $\rho = v_{\text{rot}}^2 / (R^2 \pi G Q)$, where G is the gravitational constant and Q the Toomre parameter. Inserting the disk properties for Circinus and NGC 1068 (Table 1), yields UV luminosities of $L_{\text{UV}} = 5 \times 10^{44} \text{ erg s}^{-1}$ for Circinus

and $L_{\text{UV}} = 6 \times 10^{45} \text{ erg s}^{-1}$ for NGC 1068. These luminosities are about a factor of 20 higher than their actual luminosities (Table 1). We thus conclude that within our massive thick gas disk turbulent gas pressure exceeds by far radiation pressure.

As a further test, we calculated the expected mass outflow rates and terminal velocities for radiation pressure-driven winds (Eqs. (34) and (35) of Chan & Krolik 2016). We find $\dot{M} = 0.06 M_{\odot} \text{ yr}^{-1}$ and $v_{\infty} = 1870 \text{ km s}^{-1}$ for Circinus and $\dot{M} = 0.34 M_{\odot} \text{ yr}^{-1}$ and $v_{\infty} = 3500 \text{ km s}^{-1}$ for NGC 1068. These mass outflow rates are about two times lower, the terminal wind velocities more than three times higher than our values (Table 2). The terminal wind speeds of the radiation-pressure-driven winds are significantly higher than those observed in local AGN by (Müller-Sánchez et al. 2011). The energy density of our model disk is thus dominated by kinematics (turbulence), that of the wind by the magnetic field (Table 2).

We thus conclude that IR radiation pressure does not play a major role in our thick disks, because they are massive and strongly magnetized. In the following we will thus ignore radiation pressure, keeping in mind that it will certainly shape the wind above the thin gas disk and probably even the inner rim of the wind above the thick disk, being responsible for the wind opening angle (Fig. 1). In our model, we assumed a parabolic hollow wind cone with a half-opening angle of $\sim 25^\circ$ at a height of $\sim 4 \text{ pc}$. Magnetocentrifugal winds can be recognized by their relatively low terminal wind speeds (Fig. 4) and high rotation velocities.

2.2. Thick turbulent clumpy gas disk

Gas disks around central galactic black holes contain clumps of high volume densities (e.g., Krolik & Begelman 1988; Güsten et al. 1987). The formation of regions of overdense gas is caused by thermal instabilities and, if present, selfgravity (e.g., Wada et al. 2002)¹. In turbulent galactic disks, gas clumps are of transient nature with lifetimes of about a turbulent crossing time (e.g., Dobbs & Pringle 2013). The governing gas physics of such disks are highly time-dependent and intrinsically stochastic. Over a long-enough timescale, turbulent motion of clumps is expected to redistribute angular momentum in the gas disk like an effective viscosity would do. This allows accretion of gas toward the center and makes it possible to treat the disk as an accretion disk (e.g., Pringle 1981). This gaseous turbulent accretion disk rotates in a given gravitational potential Φ with an angular velocity $\Omega = \sqrt{R^{-1} \frac{d\Phi}{dR}}$, where R is the disk radius.

Vollmer & Davies (2013) develop an analytical model for turbulent clumpy gas disks where the energy to drive turbulence is supplied by external infall or the gain of potential energy by radial gas accretion within the disk. The gas disk is assumed to be stationary ($\partial\Sigma/\partial t = 0$) and the external mass accretion rate to be close to the mass accretion rate within the disk (the external mass accretion rate feeds the disk at its outer edge). The external and disk mass accretion rates averaged over the viscous timescale are assumed to be constant. Within the model, the disk is characterized by the disk mass accretion rate \dot{M} and the Toomre Q parameter which is used as a measure of the gas content of the disk for a given gravitational potential. Vollmer & Davies (2013) suggest that the velocity dispersion of the torus gas is increased through adiabatic compression by the infalling gas. The gas clouds are not assumed to be selfgravitating. The disk velocity

¹ Another possibility consists of supernova-driven turbulence (e.g., Wada et al. 2009).

dispersion is fixed by the mass accretion rate and the gas surface density via the Toomre parameter Q . Turbulence is assumed to be supersonic, creating shocks in the weakly ionized dense molecular gas. For not too high shock velocities ($< 50 \text{ km s}^{-1}$) these shocks will be continuous (C-type). The cloud size is determined by the size of a C-shock at a given velocity dispersion. Typical cloud sizes are $\sim 0.02 \text{ pc}$ at the inner edge of the thick disk and $\sim 0.1 \text{ pc}$ at a radius of 5 pc (Vollmer & Davies 2013).

In such a turbulent clumpy gas disk the area filling factor is

$$\Phi_A = \Phi_V H / r_{cl} = 11.6 \sqrt{\frac{v_{A,0}}{Q v_{turb}}}, \quad (5)$$

where r_{cl} is the cloud radius, $v_{A,0} = 1 \text{ km s}^{-1}$ the Alfvén velocity and v_{turb} the turbulent velocity dispersion of the disk. The Toomre parameter is given by

$$Q = \frac{v_{turb}}{v_{rot}} \frac{M_{dyn}}{M_{gas}}, \quad (6)$$

where v_{rot} is the rotation velocity, M_{dyn} the dynamical mass, and M_{gas} the disk gas mass.

The disk mass accretion rate is given by

$$\dot{M}_{thick \text{ disk}} = 2\pi\nu\Sigma = 2\pi\Phi_A v_{turb} H^2 \rho, \quad (7)$$

where $\nu = \Phi_A v_{turb} H$ is the gas viscosity, $\Sigma = \rho H$ the gas surface density, ρ the gas density, and H the disk thickness. In a disk of constant Q in hydrostatic equilibrium

$$\rho = \Omega^2 / (\pi G Q), \quad (8)$$

where Ω is the angular velocity and G the gravitation constant (e.g., Vollmer & Beckert 2002). This leads to

$$\dot{M}_{thick \text{ disk}} = 2\Phi_A \frac{v_{turb}^3}{GQ}. \quad (9)$$

We parametrized the model with M_{dyn}/M_{gas} and the turbulent velocity of the disk v_{turb} . This leads to the Toomre Q parameter (Eq. (6)), the area filling factor (Eq. (5)), and the disk mass accretion rate (Eq. (9)).

2.3. Launching a wind from a thin disk

Wardle & Koenigl (1993) investigated the vertical structure of magnetized thin accretion disks that power centrifugally driven winds. The magnetic field is coupled to the weakly ionized disk material by ion-neutral and electron-neutral collisions. The resulting strong ambipolar diffusion allows a steady state field configuration to be maintained against radial inflow and azimuthal shearing. They showed that the presence of a magnetocentrifugal wind implies that the thin disk has to be confined by magnetic stresses rather than by the tidal field. These authors derived criteria for viable thin-disk-wind models based on the ratio of the dynamical timescale to the neutral-ion coupling time $\eta = \eta_{in} x_i \rho \Omega^{-1}$, where $\eta_{in} = 3.7 \times 10^{13} \text{ cm}^3 \text{ s}^{-1} \text{ g}^{-1}$ (Draine et al. 1983) is the collision coefficient and x_i the ionization fraction, the ratio of the Alfvén speed to the turbulent velocity or sound speed $a = v_A/c$, and the Mach number associated with the inward radial drift of the neutral gas at the midplane $\epsilon = v_r/c$: (i) $\eta > 1$ insures a pure ambipolar diffusion regime and (ii) $(2\eta)^{-\frac{1}{2}} \lesssim a \lesssim 2 \lesssim \epsilon\eta$ insures (1) that the disk rotates sub-Keplerian, (2) that the disk is confined by magnetic stresses,

(3) the validity of the wind launching criterion, (4) a wind starting point that lies well above the disk scale height.

The ionization fraction is given by

$$x_i = \gamma \left(\frac{\zeta_{CR}}{n_H} \right)^{\frac{1}{2}}, \quad (10)$$

where $\gamma = 600 \text{ cm}^{-\frac{3}{2}} \text{ s}^{\frac{1}{2}}$, $\zeta_{CR} = 2.5 \times 10^{-15} \text{ s}^{-1}$ (Vollmer & Davies 2013), and $n_H = \rho / (2.3 \times m_p)$. With Eq. (8) and $Q = 1$ we obtain

$$\eta = \gamma \eta_{in} \sqrt{\frac{\zeta_{CR} 2.3 m_p}{\pi G Q}} \simeq 4. \quad (11)$$

With an Alfvén speed of $v_A = 1 \text{ km s}^{-1}$ (Vollmer & Davies 2013), a turbulent or sound speed of $c = 1.5 \text{ km s}^{-1}$, and a radial inflow velocity $v_r = 1.5 \text{ km s}^{-1}$, we obtain $a = 0.7$ and $\epsilon = 1$. This set of parameters is close to that of the typical solutions of Wardle & Koenigl (1993) and fulfills all criteria cited above.

Since in the model of Wardle & Koenigl (1993) the transition from a sub-Keplerian quasi-hydrostatic disk to a centrifugally driven outflow occurs naturally, we conclude that radiation pressure is a priori not needed to launch the wind from the thin maser disk. On the other hand, we expect that radiation pressure accelerates the centrifugally launched gas to higher velocities and larger radii until the point where the pressure of the azimuthal magnetic field equals the radiation pressure.

2.4. Magnetocentrifugal wind

Since we want to describe the magnetocentrifugal wind with ideal MHD, we need to assess the role of ambipolar diffusion in the thick gas disk and the wind. According to McKee et al. (2010) the Reynolds number for ambipolar diffusion is

$$R_{AD} = 4\pi\eta_{in}\rho_i\rho_n l v B^{-2}, \quad (12)$$

where $\eta_{in} = 3.7 \times 10^{13} \text{ cm}^3 \text{ g}^{-1} \text{ s}^{-1}$ (McKee et al. 2010) is the ion-neutral coupling coefficient, ρ_i and ρ_n are the ion and neutral densities, respectively, l and v the characteristic length scale and velocity, and B the magnetic field strength. We note that the parameter β which describes the coupling between the gas and the magnetic field (e.g., Pudritz & Norman 1983) is the inverse of the Reynolds number for ambipolar diffusion $\beta = t_{ni}/t_{flow} = R_{AD}^{-1}$, where t_{ni} is the neutral-ion collision timescale and $t_{flow} = l_{flow}/v_{flow}$ the timescale of the flow. Assuming energy equipartition $B^2/(8\pi) = 1/2\rho v^2$, meaning that the wind speed equals the Alfvénic velocity, the Reynolds number is

$$R_{AD} = \eta_{in}\rho_i l v^{-1}. \quad (13)$$

We assumed a degree of ionization

$$x_i = \frac{n_i}{n_n} = \gamma \left(\frac{\zeta_{CR}}{n_H} \right)^{\frac{1}{2}}. \quad (14)$$

For the thick gas disk we assumed a mean density of $n_n = \Omega^2/(\pi G Q) = 10^6 \text{ cm}^{-3}$, a characteristic length scale equal to the disk height $l \sim H \sim 0.5 \text{ pc}$, and a characteristic velocity equal to the velocity dispersion $v = 40 \text{ km s}^{-1}$ (see Table 1). This yields an ionization fraction $x_i = 3 \times 10^{-8}$, an ion density of $\rho_i = 30 \times 3 \times 10^{-8} n_n$ (the factor 30 is due to the heavy ion approximation), and a Reynolds number for ambipolar diffusion

$R_{AD} = 20 \gg 1$. Therefore, ambipolar diffusion does not play an important role² in the thick disk and the approximation of ideal MHD is justified.

For typical wind densities of $n_{\text{wind}} = 10^5 \text{ cm}^{-3}$, wind velocities of $v_{\text{wind}} = 300 \text{ km s}^{-1}$ (see Sect. 2.9), flow lengthscale of $l_{\text{wind}} = 1 \text{ pc}$, and $R_{AD} = 20$ or $\beta = 0.05$, we obtained an ionization fraction $x_i = n_i/n_n = 10^{-6}$. The ionization rate caused by cosmic rays is $x_{i,\text{CR}} = 10^{-7}$. The ten times higher ionization rate, which is required for the application of ideal MHD, can be easily sustained by the X-ray emission of the central engine which directly illuminates the wind (X-ray dominated region XDR; Meijerink & Spaans 2005).

The equations of stationary, axisymmetric, ideal MHD are the conservation of mass, the equation of motion, the induction equation for the evolution of the magnetic field, and the solenoidal condition on the magnetic field:

$$\begin{aligned} \nabla \cdot (\rho \mathbf{v}) &= 0 \\ \rho \mathbf{v} \cdot \nabla \mathbf{v} &= -\nabla p - \rho \nabla \Phi + \frac{1}{4\pi} (\nabla \times \mathbf{B}) \times \mathbf{B} \\ \nabla \times (\mathbf{v} \times \mathbf{B}) &= 0 \\ \nabla \cdot \mathbf{B} &= 0, \end{aligned} \quad (15)$$

where ρ is the gas density, \mathbf{v} the gas velocity, p the gas pressure, Φ the gravitational potential, and \mathbf{B} the magnetic field. The angular momentum equation for an axisymmetric flow is described by the azimuthal component of the equation of motion. For simplicity we ignored stresses that would arise from turbulence and neglect the pressure and gravitational potential (see, e.g., Königl & Pudritz 2000). The solution is thus only valid for the freely flowing part of the wind far away from the gas disk ($z/H \gg 1$)³. With the separation of poloidal and toroidal field components $\mathbf{B} = \mathbf{B}_p + B_t \hat{\mathbf{e}}_t$ and $\mathbf{v} = \mathbf{v}_p + v_t \hat{\mathbf{e}}_t$ we obtain

$$\rho \mathbf{v}_p \cdot \nabla (r v_t) = \frac{1}{4\pi} \mathbf{B}_p \cdot \nabla (r B_t). \quad (16)$$

The induction equation links the velocity field and the magnetic field. Because of axisymmetry, the poloidal velocity vector is parallel to the poloidal component of the magnetic field (Königl & Pudritz 2000), which implies

$$\rho \mathbf{v}_p = k \mathbf{B}_p, \quad (17)$$

with the mass load per unit time and unit magnetic field flux, which is preserved along streamlines from the rotator

$$k = \frac{\rho v_p}{B_p} = \frac{d\dot{M}_{\text{wind}}}{d\Phi}, \quad (18)$$

where $d\dot{M}_{\text{wind}} = \rho v_p dA$ is the mass loss rate of the wind and $d\Phi = B_p dA$ is the magnetic flux. The mass load is determined by the physics of the underlying rotator, in other words, the accretion disk.

The induction equation also determines the field of the flow (Königl & Pudritz 2000)

$$B_t = \frac{\rho r}{k} (\omega - \omega_0), \quad (19)$$

² $R_{AD} = \infty$ corresponds to ideal MHD.

³ Within this approximation the winds above the thin and thick disk have to be regarded separately. The wind structure in the transition region is more complex and its study is beyond the scope of this article.

where $\omega = v_t/r$ is the angular velocity, and ω_0 is the angular velocity at the disk midplane.

The application of Eq. (17) to the momentum equation with $k = \text{const}$ yields a constant angular momentum per unit mass along a streamline

$$l = r v_t - \frac{r B_t}{4\pi k}. \quad (20)$$

This means that the specific angular momentum of a magnetized flow is carried by both the rotating gas and the twisted field. The value of l can be found by

$$r v_t = \frac{lm^2 - r^2 \omega_0}{m^2 - 1}, \quad (21)$$

where $m = v_p/v_A$ is the Alfvén Mach number and $v_A = B_p/\sqrt{4\pi\rho}$.

Once the wind speed equals the Alfvén speed at a point called the Alfvén point, magnetic field lines that are carried and stretched by the wind open up, and all the mass at this point is considered lost from the disk. Another way to look at this process is to think of the magnetic field lines as rods that are attached to the rotating disk at one end, whereas the other ends of the open field lines are radially stretched beyond the Alfvén point. As a result, each field line applies a torque on the disk and spins it down. This torque is proportional to the momentum of the wind at the Alfvén point, to the disk rotation rate, and to the distance of the Alfvén point (the lever arm that applies the torque). The imaginary surface that represents all Alfvén points is called the Alfvén surface and the integral of the mass flux through this surface is the mass loss rate of the disk to the wind. The Alfvén surface is defined by $r = r_A$ on the outflow field lines where $m = 1$ (Eq. (21)). The flow along any field line corotates with the accretion disk until this surface is reached.

From the regularity condition at the Alfvén critical point where the denominator of Eq. (21) vanishes, it follows that

$$l = \omega_0 r_A. \quad (22)$$

The index 0 denotes quantities which are evaluated in the disk plane. The terminal speed of the flow is approximately

$$v_\infty \simeq \sqrt{2} \omega_0 r_A. \quad (23)$$

Michel (1969) found that the terminal speed of a cold MHD wind is on the order of

$$v_\infty \sim \left(\frac{\omega^2 \Phi^2}{\dot{M}_{\text{wind}}} \right)^{\frac{1}{3}}, \quad (24)$$

with the conservation of the magnetic flux $\Phi = B_p r_A^2 = B_{0p} r_0^2$ (Pudritz & Norman 1983).

Combining Eqs. (23) and (24) leads to

$$r_A \sim \frac{v_\infty}{\sqrt{2} \omega_0} = \frac{1}{\sqrt{2}} \left(\frac{\Phi^2}{\omega_0 \dot{M}_{\text{wind}}} \right)^{\frac{1}{3}} = \left(\frac{B_p^2 r_0^4}{\omega_0 \dot{M}_{\text{wind}}} \right)^{\frac{1}{3}}. \quad (25)$$

The mass outflow rate in a high density regime ($\beta \ll 1$) is given by

$$\dot{M}_{\text{wind}} = \int_A \rho \mathbf{v}_p \cdot d\mathbf{A} \sim 4\pi (\rho v_p)_{r_A} r_A^2 \Omega \quad (26)$$

(Pudritz & Norman 1983), where A is the Alfvénic surface and $4\pi\Omega$ the solid angle that it subtends. For a cone with a half-opening angle θ , $\Omega = (1 - \cos(\theta))$. We estimated the gas density at the Alfvénic surface through conservation of mass flux within the thick gas disk and the wind:

$$\rho v_r = 2\rho_A v_p, \quad (27)$$

where v_r is the radial velocity of the disk gas and ρ_A the gas density at the Alfvénic surface. The radial velocity of the thick disk gas is given by the gas viscosity $\nu = v_r R = \Phi_A v_{\text{turb}} H$ and thus $v_r = v_{\text{turb}}^2 / v_{\text{rot}}$. With $v_p \sim v_{\text{rot}}$ this leads to

$$\rho_A = \frac{1}{2} \left(\frac{v_{\text{turb}}}{v_{\text{rot}}} \right)^2 \rho. \quad (28)$$

Inserting Eqs. (25) and (28) into Eq. (26) yields

$$\dot{M}_{\text{wind}} = \left(\xi \frac{1}{2} \left(\frac{v_{\text{turb}}}{v_{\text{rot}}} \right)^2 \rho v_{\text{rot}} B_p^{\frac{4}{3}} r^{\frac{8}{3}} \omega_0^{-\frac{2}{3}} \right)^{\frac{3}{5}}, \quad (29)$$

where $\xi = 4\pi\Omega$.

We assumed that the poloidal regular magnetic field is about a third of the total magnetic field. This is consistent with the fraction of the regular large scale to the total magnetic field in spiral galaxies (e.g., Beck 2015). Energy equipartition between the gas energy density and the total magnetic field yields

$$B_p = \frac{1}{3} \sqrt{4\pi\rho v_{\text{turb}}^2}, \quad (30)$$

where v_{turb} is the turbulent gas velocity dispersion of the accretion disk. The density of the accretion disk in hydrostatic equilibrium and with a constant Toomre Q parameter is given by $\rho = \omega_0^2 / (\pi G Q)$ (e.g., Vollmer & Beckert 2002), where G is the gravitation constant.

Inserting Eq. (30) into Eq. (29) leads to our final expression for the wind mass loss rate:

$$\dot{M}_{\text{wind}} = 2^{\frac{1}{5}} 3^{-\frac{4}{5}} \pi^{-\frac{3}{5}} \xi^{\frac{3}{5}} Q^{-1} G^{-1} v_{\text{rot}} v_{\text{turb}}^2. \quad (31)$$

From Eq. (31) it becomes clear that there is a degeneracy between the factor $\frac{1}{3}$ between the poloidal and the total magnetic field (Eq. (30)) and the solid angle subtended by the wind ξ . An increase of the solid angle, together with an increase of the poloidal magnetic field fraction, leads to the same wind mass loss.

2.5. Linking the wind to the accretion disk

To determine the mass accretion rate of the thin disk, we assume that the wind outflow rates from the thin disk and the inner edge of the thick disk are comparable. Since the solid angle subtended by the wind from the thick disk (see Sect. 2.6) is about three times larger than the solid angle subtended by the wind from the thin disk with a half-opening angle of $\theta \sim 20^\circ$, this implies that the mass flux of the outflow from the inner disk is about three times smaller than that from the inner edge of the thick disk.

To calculate the torque exerted by the wind on the underlying accretion disk, we applied the momentum equation (Eq. (16)) to the accretion disk (see Königl & Pudritz 2000):

$$\frac{\rho v_r}{r_0} \frac{\partial(r_0 v_{\text{rot}})}{\partial r_0} = \frac{B_r}{4\pi r_0} \frac{\partial(r_0 B_t)}{\partial r_0} + \frac{B_z}{4\pi} \frac{\partial B_t}{\partial z}. \quad (32)$$

The specific angular momentum is thus removed from the accretion flow by magnetic torques associated with the radial or vertical shear of the toroidal field. We assumed that for typical field inclination the second term of Eq. (32) dominates. This implies that the magnetic field lines are inclined less than $\sim 60^\circ$ with respect to the disk normal.

Mass conservation in an accretion disk gives the relation between the disk mass accretion rate and the radial velocity

$$\dot{M}_{\text{thin disk}} = -2\pi \Sigma v_r r_0, \quad (33)$$

where $\Sigma = \rho H$ is the gas surface density and H the disk thickness. With Eq. (32) we obtain

$$\dot{M}_{\text{thin disk}} \frac{d(r_0 v_{\text{rot}})}{dr_0} = -r_0^2 B_t B_z. \quad (34)$$

The angular momentum can be carried away by Alfvén waves or, when the magnetic field lines are inclined more than $\sim 30^\circ$ with respect to the disk normal, by a centrifugally driven wind (Blandford & Payne 1982). Thus, the range of inclination angles θ_B between the magnetic field lines and the disk normal is approximately $30^\circ \leq \theta_B \leq 60^\circ$.

Rewriting Eq. (20) as $r B_t = 4\pi k(r v_{\text{rot}} - l)$ and inserting the expressions for k (Eq. (18)) and l (Eq. (22)) yields

$$\dot{M}_{\text{thin disk}} = f_g \dot{M}_{\text{wind}} \left(\frac{r_A}{r_0} \right)^2, \quad (35)$$

where f_g is a geometric factor, which depends on the geometry of the poloidal field. Following Pudritz & Norman (1986) we assume $f_g = \frac{1}{3}$ for a polar wind. This means that if the viscous torques in the disk are relatively unimportant, the angular momentum loss is provided by the magnetocentrifugal wind.

2.6. Where the wind sets in

Within the presented scenario the external mass inflow $\dot{M}_{\text{ext}} = \dot{M}_{\text{disk}}$ and the Toomre parameter Q determine the physical properties of the thick disk (Sect. 2.2). With high \dot{M}_{disk} and Q , the turbulent disk can be relatively thick. The disk is permeated by a magnetic field which has a large-scale regular and a small-scale turbulent magnetic field. The regular field has a poloidal and a toroidal component. At a given radius or distance r_{wind} to the central black hole the angle between the poloidal field lines and the disk normal exceeds 30° and a magnetocentrifugal wind is launched. At $r < r_{\text{wind}}$ the wind provides the transport of angular momentum (see Sect. 2.4) and the disk becomes thin. The mass accretion rate of the thin disk is given by Eq. (35). For simplicity, we assume a sharp transition between the thick and the thin disk at $r = r_{\text{wind}}$. Furthermore, we assumed that the wind outflow rate is the same above the thick and the thin disk and that the Alfvén radii of the thin and thick disk are the same at the transition radius r_{wind} . With Eqs. (25), (30), and (31) this implies that the gas pressures of the thin and thick disk at r_{wind} are the same: $\rho_{\text{thick}} v_{\text{turb, thick}}^2 = \rho_{\text{thin}} v_{\text{turb, thin}}^2$. Using Eq. (8) we obtain $v_{\text{turb, thick}} / v_{\text{turb, thin}} = \Sigma_{\text{thin}} / \Sigma_{\text{thick}} = \sqrt{Q_{\text{thick}} / Q_{\text{thin}}}$.

In the absence of detailed knowledge of the configuration of the magnetic field, we assumed that mass conservation determines the radius r_{wind} where the wind sets in:

$$\dot{M}_{\text{thick disk}} - \dot{M}_{\text{wind}} - \dot{M}_{\text{thin disk}} = 0. \quad (36)$$

A constant turbulent velocity of the thick gas disk is assumed, which is consistent with the SINFONI H₂ observations of

Table 1. Model input parameters.

	D (Mpc)	L_{bol}^a (erg s ⁻¹)	M_{BH} (M_{\odot})	M_*^b ($M_{\odot} \text{ pc}^{-\frac{5}{4}}$)	v_{rot}^c (km s ⁻¹)	v_{turb}^d (km s ⁻¹)	Ω^e	r_{wind}^f (pc)
Circinus	4.2	3×10^{43}	1.6×10^6	1.0×10^6	100	30	0.022	0.53
NGC 1068	14.4	3×10^{44}	8.6×10^6	3.0×10^6	170	50	0.022	1.5

Notes. ^(a)Moorwood et al. (1996); Pier et al. (1994). ^(b)Leading to a flat rotation curve at $R = 3$ pc for Circinus and $R = 5$ pc for NGC 1068. ^(c)Rotation velocity at $r = 10$ pc. ^(d)Assumed turbulent velocity dispersion of the thick disk. ^(e)Assumed solid angle subtended by the wind. ^(f)Outer radii of the thin maser disks (Greenhill et al. 2003, Greenhill & Gwinn 1997).

Table 2. Model results for the thick disk, magnetocentrifugal wind, and the thin disk.

	$M_{\text{gas}}/M_{\text{dyn}}$	Q	Φ_A	B_p^a (mG)	r_A (pc)	$\dot{M}_{\text{thick disk}}$ ($M_{\odot} \text{ yr}^{-1}$)	\dot{M}_{wind} ($M_{\odot} \text{ yr}^{-1}$)	$\dot{M}_{\text{thin disk}}$ ($M_{\odot} \text{ yr}^{-1}$)	$p_B(r_{\text{wind}})$ (erg cm ⁻³)	$p_{\text{rad}}(r_{\text{wind}})$ (erg cm ⁻³)
Circinus	0.010	22	0.45	14	0.85	0.26	0.14	0.12	7.4×10^{-6}	5.1×10^{-6}
NGC 1068	0.016	15	0.42	15	2.4	1.57	0.85	0.73	8.5×10^{-6}	6.2×10^{-6}

Notes. ^(a)Large-scale polar magnetic field in the wind with $B_p = 1/3 B_0$.

Hicks et al. (2009). The observed extent of the thin disk gives $M_{\text{dyn}}/M_{\text{gas}}$ and thus determines Q (Eq. (6)), the mass accretion rate of the thick disk $\dot{M}_{\text{thick disk}}$ (Eq. (9)), wind outflow rate \dot{M}_{wind} (Eq. (31)), the accretion rate of the thin disk $\dot{M}_{\text{thin disk}}$ (Eq. (35)), and the radius r_{wind} (Eq. (36)) where the wind sets in.

The dynamical mass in the galactic center is given by

$$M_{\text{dyn}} = M_{\text{BH}} + M_* r^{\frac{5}{4}}, \quad (37)$$

where M_{BH} is the mass of the central black hole and M_* defines the mass of the central star cluster (Vollmer & Duschl 2001). This parametrization of the dynamical mass leads to an approximately constant rotation curve $v_{\text{rot}} = \sqrt{M_{\text{dyn}} G / r}$ beyond the sphere of the influence of the black hole.

2.7. Model parameters

We applied our model to the two best-studied nearby AGN: the Circinus galaxy ($D = 4.2$ Mpc) and NGC 1068 ($D = 14.4$ Mpc). The input parameters are presented in Table 1. The adopted bolometric luminosities are consistent with the values estimated by Moorwood et al. (1996) for Circinus and Pier et al. (1994) and Hönig et al. (2008) for NGC 1068. Pudritz & Norman (1983) set the solid angle subtended by the wind to $4\pi\Omega = 4\pi 0.1$, which corresponds to a half-opening angle of $\theta = 26^\circ$. In our scenario, this cone is not filled as in the Pudritz & Norman model, but hollow. The solid angle subtended by a hollow cone that reproduces IR interferometric observations is about $4\pi\Omega \sim 0.025$. This corresponds to inner and outer half-opening angles of $\theta_{\text{in}} = 20^\circ$ and $\theta_{\text{out}} = 24^\circ$, comparable to the narrow line region cones of Mrk 1066, NGC 4051, NGC 4151 (Fischer et al. 2013), and NGC 1068 (Müller-Sánchez et al. 2011).

The choice of the turbulent velocities is motivated by Plateau de Bure Interferometer HCN and HCO⁺ observations presented in Sani et al. (2012) and Lin et al. (2016). The observed velocity dispersion of the dense gas (HCN, HCO⁺) is about a factor of 1.5 lower than that derived from SINFONI H₂ observations presented in Davies et al. (2007) and Hicks et al. (2009). The black hole masses are taken from Greenhill et al. (2003) and Lodato & Bertin (2003). The outer radii of the thin maser disks are ~ 0.4 pc

for the Circinus galaxy (Greenhill et al. 2003) and ~ 1.1 pc for NGC 1068 (Greenhill & Gwinn 1997). Since the maser disks seem to be warped these radii are lower limits. In addition, the transition between the thin and the thick disks might not be sharp as assumed by our simple model. We thus adopted $\sim 30\%$ larger radii for the transition between the thin and the thick disk (Table 1). This nicely reproduced the elongated compact components of the MIR interferometric observations (Sect. 5) and is comprised within the model uncertainties.

The resulting parameters of the thick disk, wind, and thin disk models are presented in Table 2. The Toomre Q parameter of the two thick gas disks is $Q \sim 15$ – 20 . This is higher than the values assumed by Vollmer et al. (2008) which were based on gas masses derived from NIR observations of warm H₂ (Davies et al. 2007) with an uncertain conversion factor. The lower gas masses are corroborated by HCN observations of the central 50 pc in nearby AGN (Sani et al. 2012). The area filling factor of gas clouds in the disks is close to one $\Phi_A \sim 0.5$. The wind outflow rates are comparable to the mass accretion rates of the thin disk. The thick and thin disks and magnetocentrifugal winds of the Circinus galaxy and NGC 1068 have very different mass accretion and outflow rates, the mass accretion and outflow rates of NGC 1068 being about 6 times those of the Circinus galaxy. The Alfvén radii of the two galaxies are ~ 1.6 times larger than the critical radii. The situation is different from that in protostellar outflows where this ratio is approximately three. The magnetic field strength of ~ 15 mG at the Alfvén radius is well comparable to the magnetic field strength of the gas and dust torus in NGC 1068 inferred from NIR polarimetric observations (Lopez-Rodriguez et al. 2015).

2.8. Viable magnetocentrifugal disk winds

In the previous section we calculated the Toomre Q parameter, the mass accretion rates of the thick and thin disk, and the wind outflow rate based on the observed outer radius of the thin maser disks. We can now generalize and assume different transition radii r_{wind} between the thick and thin disks. For a given turbulent velocity dispersion v_{turb} , each choice of r_{wind} leads to a Toomre Q parameter and a mass accretion rate of

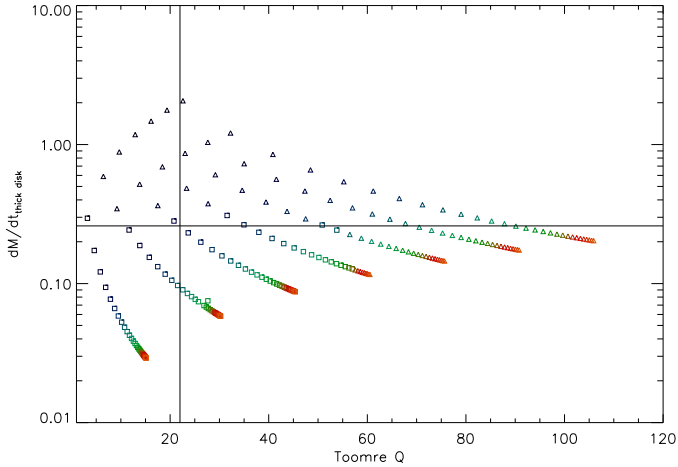


Fig. 2. Circinus galaxy: mass accretion rate of the thick gas disk (in $M_{\odot} \text{ yr}^{-1}$) as a function of the Toomre Q parameter. Each point corresponds to a given critical radius where the wind sets in and the accretion disk becomes thin. Each line corresponds to a velocity dispersion of $v_{\text{turb}} = 10, 20, 30, 40, 50, 60$, and 70 km s^{-1} (from left to right). The critical radii range from 0.2 pc (blue) to 3 pc (red) in steps of 0.1 pc. Triangles: $p_{\text{rad}}/p_{\text{B}} < 0.5$; boxes: $p_{\text{rad}}/p_{\text{B}} \geq 0.5$. The intersection of the solid lines corresponds to the assumed critical radius $r_{\text{wind}} = 0.53 \text{ pc}$ and $v_{\text{turb}} = 30 \text{ km s}^{-1}$.

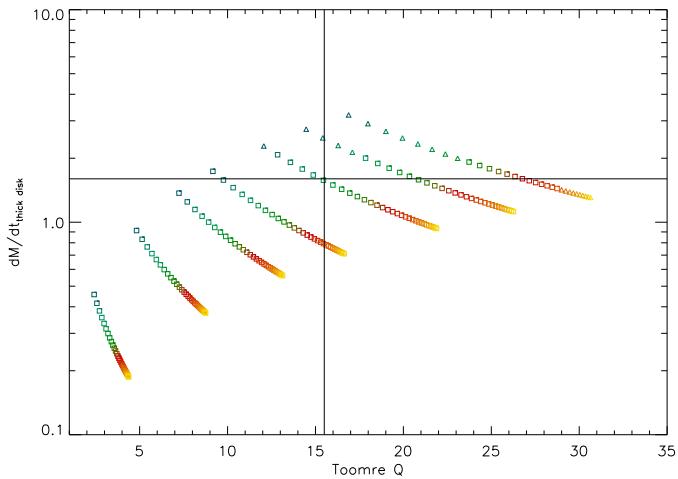


Fig. 3. NGC 1068: mass accretion rate of the thick gas disk (in $M_{\odot} \text{ yr}^{-1}$) as a function of the Toomre Q parameter. Each point corresponds to a given critical radius where the wind sets in and the accretion disk becomes thin. Each line corresponds to a velocity dispersion of $v_{\text{turb}} = 10, 20, 30, 40, 50, 60$, and 70 km s^{-1} (from left to right). The critical radii range from 1 pc (green) to 4 pc (yellow) in steps of 0.1 pc. Triangles: $p_{\text{rad}}/p_{\text{B}} < 0.5$; boxes: $p_{\text{rad}}/p_{\text{B}} \geq 0.5$. The intersection of the solid lines corresponds to the assumed critical radius $r_{\text{wind}} = 1.5 \text{ pc}$ and $v_{\text{turb}} = 50 \text{ km s}^{-1}$.

the thick disk $\dot{M}_{\text{thick disk}}$. We varied the outer radius of the thin disk within reasonable ranges and the velocity dispersion from 10 km s^{-1} to 70 km s^{-1} . The results of these calculations are presented in Figs. 2 and 3. We observe a general trend that the thick disk accretion rate decreases with increasing Q . For each Q a range of $\dot{M}_{\text{thick disk}}$ within about 1 dex leads to viable disk-wind solutions. If the radiation pressure is responsible for the angle of $\sim 30^\circ$ between the polar magnetic fields and the disk normal necessary to drive the wind, we expect that only solutions with $p_{\text{rad}}/p_{\text{B}} > 0.5$ are viable (boxes in Figs. 2 and 3).

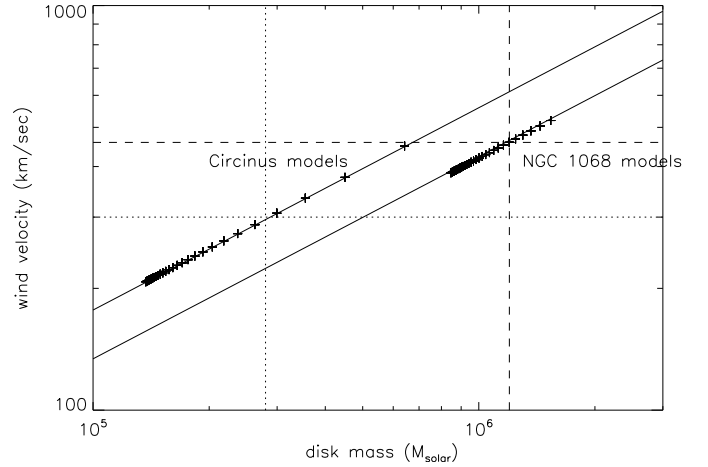


Fig. 4. Terminal wind speed (Eq. (23)) as a function of the disk gas mass within 10 pc for the models described in Sect. 2.8. The dotted and dashed lines indicate the Circinus and NGC 1068 3D models.

This would greatly reduce the number of viable solutions for the Circinus model. For $v_{\text{turb}} = 30 \text{ km s}^{-1}$ and $Q > 50$ no disk-wind configuration is viable, meaning that this kind of accretion disks cannot have a wind. The circumnuclear disk (CND) in the Galactic center with $Q = 100\text{--}200$ (Vollmer et al. 2004) is in this situation.

2.9. Terminal wind speed

The magnetocentrifugal wind has a terminal speed given by Eq. (23). We calculated the terminal wind speed for the models described in Sect. 2.8. The results are presented in Fig. 4. For a given gravitational potential (black hole mass and stellar mass distribution), the terminal wind speed increases with increasing disk gas mass ($v_{\infty} \propto M_{\text{gas}}^{1/2}$). On the other hand, we observe an offset between the relations for Circinus and NGC 1068 which is approximately proportional to the total mass included within 10 pc ($v_{\infty} \propto M_{\text{tot}}^{-1/4}$). As expected, a deeper gravitational potential leads to a higher terminal wind speed. Our model terminal wind speeds are well comparable with those given by Müller-Sánchez et al. (2011; Fig. 27). However, our model does not reproduce the extreme terminal wind speed of $\sim 1000 \text{ km s}^{-1}$ observed in NGC 1068. Since NGC 1068 has a high bolometric luminosity and an Eddington ratio of $\sim 0.2\text{--}0.7$, we suggest that radiation pressure, which is not included in our model, might play an important role for the acceleration of the gas and dust in the wind of NGC 1068.

3. Axisymmetric 3D models

3.1. Density distribution

With the analytical model described in Sect. 2 we were able to construct a model of the 3D gas distribution within a central mass distribution around a central black hole. This 3D model has three ingredients:

- a thick gas disk for $r > r_{\text{wind}}$,
- a thin gas disk for $r < r_{\text{wind}}$, and
- a magnetocentrifugal wind starting at $r = r_{\text{wind}}$.

The transition between the thin and the thick disk is assumed to be sharp, meaning that there is an inner vertical wall which is directly illuminated by the central AGN.

The structure of the thick accretion disk is given in Sect. 2.2. The disk height is determined by the hydrostatic equilibrium

$$\rho v_{\text{turb}}^2 = \rho G M_{\text{dyn}} \frac{H^2}{(r^2 + H^2)^{1.5}}. \quad (38)$$

The vertical density distribution is assumed to be Gaussian $\rho(z) = \rho_0 \exp(-(z/H)^2)$. For simplicity, we assume a smooth disk instead of a clumpy disk. Given the area filling factor of $\Phi_A \sim 0.5$ derived from Eq. (5) for the Circinus and NGC 1068 models, this approximation is acceptable. In a subsequent work we plan to extend the model to include a clumpy gas distribution.

A key ingredient of the model is the transition region between the thick and the thin disk which creates a directly illuminated inner wall of the thick gas and dust disk. Whereas the abrupt drop of the disk height might be exaggerated, we nevertheless expect a rapid decrease of the disk height caused by the onset of the magnetocentrifugal wind.

The inner disk is assumed to have a velocity dispersion of $v_{\text{turb}} = 10 \text{ km s}^{-1}$. Its density is given by

$$\rho = \frac{\Omega^2}{\pi G Q} \frac{v_{\text{turb}}^{\text{thick}}}{(10 \text{ km s}^{-1})}. \quad (39)$$

For the radiative transfer models we added a puff-up to the thin disk. As observed in young stellar objects (e.g., Monnier et al. 2006), the inner rim of the thin disk is puffed up and is much hotter than the rest of the disk because it is directly exposed to the AGN flux (Dullemond et al. 2001; Natta et al. 2001). The puff-up is located directly behind the dust sublimation radius. Within our model, the main reason for its existence is the need for an increased NIR emission of the dust distribution to reproduce available NIR observations, since the dust temperature is elevated at these small distances. The puff-up thus naturally provides the necessary increase of the NIR emission. We do not intend to elaborate a detailed model for a puff-up, which is beyond the scope of this article. The region of increased NIR emission is then obscured by the thick gas and dust disk. We are mainly interested in the latter effect. The puff-up is located at a radius of $r = 0.75 \sqrt{L_{\text{bol}}/(8 \times 10^{44} \text{ erg s}^{-1})} \text{ pc}$, has a maximum height of $h = 0.225 \sqrt{L_{\text{bol}}/(8 \times 10^{44} \text{ erg s}^{-1})} \text{ pc}$, and has a width of one sixth of its radius. For the “best fit” NGC 1068 model the puff-up is located at a radius of $r = 0.50 \sqrt{L_{\text{bol}}/(8 \times 10^{44} \text{ erg s}^{-1})}$, has a maximum height of $h = 0.150 \sqrt{L_{\text{bol}}/(8 \times 10^{44} \text{ erg s}^{-1})} \text{ pc}$, and has a width of one sixth of its radius. The vertical extent increases the solid angle of this structure and therefore leads to a higher fraction of absorbed and reradiated AGN emission at small distances from the central source. The geometry of the puff-ups was chosen ad hoc to reproduce the IR SEDs. They might be created by magnetic or radiation pressure. Alternatively, the inner maser disk might be warped and/or tilted, which would have the same effect on the IR SED (Fig. 9 of Jud et al. 2017).

The wind is assumed to have a density distribution $\rho \propto (r/\sqrt{r^2 + z^2})$ or $\rho \propto (r/\sqrt{r^2 + z^2})^2$. At the footpoint the wind has 1/50 of the density of the disk. This heuristically determined description led to MIR luminosities and visibility amplitudes which are consistent with observations. The wind is located between

$$|H| < \left(\frac{r_0/1 \text{ pc}}{H/r_0 + 0.15}\right)^2 \text{ pc} \text{ and } |H| > \left(\frac{r_0/1 \text{ pc}}{H/r_0 - 0.05}\right)^2 \text{ pc}. \quad (40)$$

This distribution has been designed ad hoc and leads to a hollow wind cone, which is consistent with that of the analytical model

and comparable to the narrow line region cones of Mrk 1066, NGC 4051, and NGC 4151 (Fischer et al. 2013).

All model cubes have the dimension $501 \times 501 \times 501$ pixels. The pixel size Δ is adapted to the bolometric luminosity of the central source in the following way:

$$\Delta = 0.04 \sqrt{L_{\text{bol}}/(8 \times 10^{44} \text{ erg s}^{-1})} \text{ pc}. \quad (41)$$

Thus a gas disk with a high luminosity AGN is more extended than a gas disk with a central source of low luminosity. This ensures that the inner disk radius, the sublimation radius, is resolved in our model cubes.

Figure 5 shows a cut through the density distribution of the Circinus model with $L_{\text{bol}} = 3 \times 10^{43} \text{ erg s}^{-1}$ and the NGC 1068 model with $L_{\text{bol}} = 3 \times 10^{44} \text{ erg s}^{-1}$. The thick disk, thin disk, and the magnetocentrifugal wind are clearly visible. The inner gap of the thin disk is due to the sublimation of dust (Barvainis 1987; Kishimoto et al. 2011).

We note that the models show sharp edges. Moreover, they are radially cut at 2 and 6 pc. These properties influence the IR SEDs (Hönig & Kishimoto 2010) and IR visibility amplitudes. For comparison, we also set up a model of a thick gas disk without a wind (Fig. A.1).

3.2. Radiative transfer

From the dust density distribution discussed in Sect. 3.1, we calculate SEDs as well as images in the near- and mid-infrared with the help of RADMC-3D (Dullemond 2012). The latter is a modular and versatile 3D radiative transfer code relying on the Monte Carlo method. A constant gas-to-dust ratio of 150 (e.g., Draine & Lee 1984; Draine et al. 2007) was assumed. The dust density model is binned onto a spherical, 2D grid. It is illuminated by a central energy source, which is point-like, isotropically emitting with an SED resembling the one of quasars (see discussion in Schartmann et al. 2005), and normalized to the bolometric luminosities of NGC 1068 and the Circinus galaxy. The dust composition is according to a galactic dust model similar to the one employed in Schartmann et al. (2014). Five different grain sizes with a size distribution as in Mathis et al. (1977) are used for each of the three different grain species: silicate and the two orientations of graphite grains with optical properties adapted from Draine & Lee (1984), Laor & Draine (1993), Weingartner & Draine (2001) and Draine (2003). Following a thermal Monte Carlo simulation (Lucy 1999; Bjorkman & Wood 2001), the resulting dust temperature distribution is used to simulate continuum SEDs and images at near- and mid-infrared wavelengths. As the models discussed in this work reach very high optical depths close to the midplane ($\tau_V \sim 10^4$ – 10^6), we use the so-called modified random walk method (Fleck & Canfield 1984; Robitaille 2010) to reduce computation times. In cells of very high optical depth photon packages might end up on a random walk with a very large number of absorption and re-emission or scattering events. This is prevented by using the analytical solution to the diffusion equation within this cell. Min et al. (2009) showed that this results in very good approximations of the radiation transfer in objects with optical depths as high as in our setup.

4. Model results

In this section we use the central extinction to discriminate between type 1 and type 2 objects and compare the model infrared luminosities, SEDs, and point source fractions to observations. We illuminated the density distribution isotropically

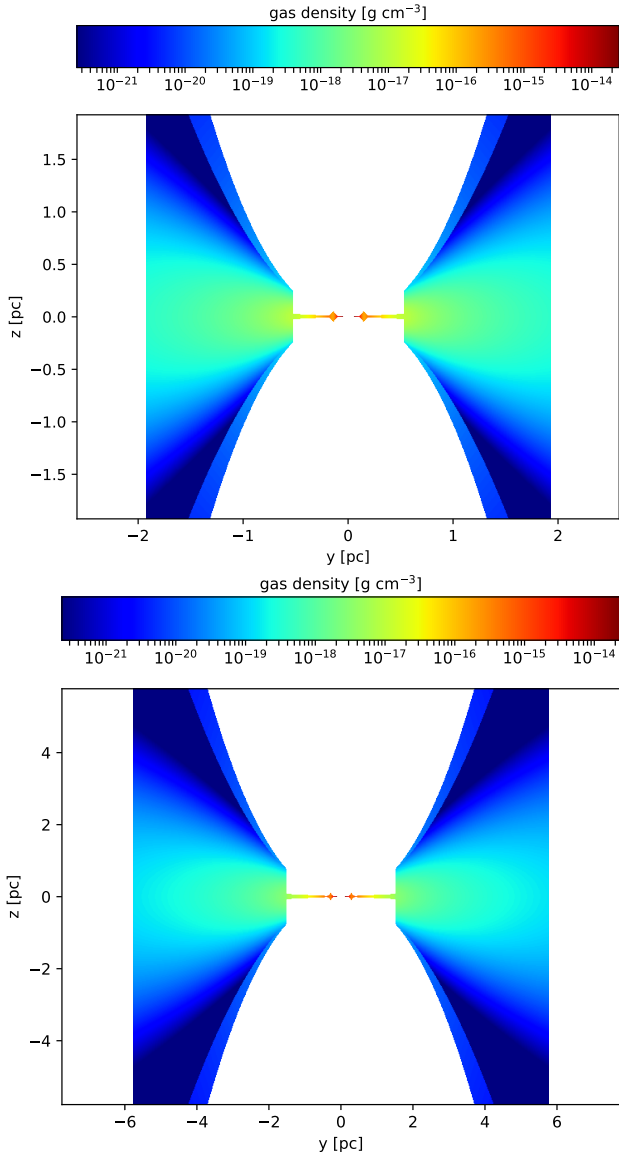


Fig. 5. Density cut through the model cube of the Circinus galaxy (*upper panel*) and NGC 1068 (*lower panel*). The scaling is logarithmic. The thick disk, thin disk, and the magnetocentrifugal wind are clearly visible. The thick gas ring near the inner edge of the thin disk was added ad hoc to enhance the NIR emission.

and with a $\cos(\theta)$ pattern. The inner puff-up is modeled by a Gaussian whose maximum is placed at $2, 3, 4 \times r_{\text{sub}}$, where the sublimation radius (Kishimoto et al. 2007, Eq. (10) of Bartscher et al. 2013) is given by

$$r_{\text{sub}} = 0.175 \times \sqrt{\frac{L_{\text{bol}}}{8 \times 10^{44} \text{ erg s}^{-1}}} \text{ pc}. \quad (42)$$

The FWHM of the Gaussian is half the radius of its maximum. The model with $4 \times r_{\text{sub}}$ represents our basic model.

4.1. Central extinction

The extinction of the central pixel of the model image determines the optical classification between type 1 and type 2 objects. Schnorr-Müller et al. (2016) studied the broad-line region (BLR) of nine nearby Seyfert 1 galaxies. They showed

that type 1.5 objects have central extinctions ≤ 3 mag, whereas type 1.8–1.9 objects have central extinctions between 4 and 8 mag. The extinction of type 2 objects thus exceeds ~ 10 mag (Bartscher et al. 2015 found 15–35 mag). Netzer (2015) argued that the ratio between type 1 (including types 1.8–1.9) and type 2 objects is about one (see also Mateos et al. 2017). This implies a ratio between the disk height and radius of $H/R \sim 0.6$ or an angle between the disk height and the equatorial plane of $\sim 30^\circ$. Since type 1.8/1.9 objects are not necessarily obscured by the torus, but more likely by “foreground” (kpc-scale) dust lanes in the host galaxy (e.g., Prieto et al. 2014), this angle has to be regarded as an upper limit. We are able to check if our model results are consistent with these findings.

The optical depth τ_V as a function of the inclination angle of the gas disk is presented in Fig. 6. Without a wind component, the optical depth is unity for an inclination angle of $\sim 50^\circ$ for all models. We find $\tau_V \sim 50$ for $i = 60^\circ$. In the presence of a wind component the optical depth increases with respect to that of the model without wind at $i = 60^\circ$. Thus, the wind component provides the bulk of the central extinction at these inclinations. We also observed a luminosity-dependence of the increase of the optical depth due to the wind, which can be explained in the following way: since our model cubes always contain 501^3 pixels and the pixel size varies with the square root of the bolometric luminosity, the extent of the cube also increases with $\sqrt{L_{\text{bol}}}$. This leads to a longer sightline through the wind, and thus a higher extinction. This extinction obviously depends on the geometry (opening angle and width) of the wind.

The optical depth at $i < 40^\circ$ also depends on (i) the ratio between the wind density and the disk density at the footpoint of the wind, (ii) the dust absorption coefficient, and (iii) the gas-to-dust ratio of the wind. If, for example, we decrease the ratio between the wind and the disk density from $1/50$ to $1/150$, the central extinction decreases by a factor of 3. For the central extinction, we prefer these models, because they are consistent with a small fraction of type 1i objects (types > 1.5) among the type 1 objects. These models show 1.6 times smaller MIR luminosities and unchanged NIR luminosities. The IR emission distributions of the $1/z$ wind, $1/z^2$ wind, and a wind-to-disk ratio $1/150$ models are equivalent to the first order. In the following, we will use the $1/z$ wind with a wind-to-disk ratio of $1/50$.

We conclude that our model is in broad agreement with existing observations. The observed extinction of type 1.5 objects of ≤ 3 mag and the higher extinction of type 1.8–1.9 objects (between 4 and 8 mag; Schnorr-Müller et al. 2016) might thus well be due to magnetocentrifugal winds. We note that this is compatible with the finding of Stern & Laor (2012) and Schnorr-Müller et al. (2016), that the structure obscuring the BLR exists on scales smaller than the narrow line region.

4.2. Spectral energy distribution (SED)

The spectral energy density distribution for the radiative transfer Circinus model (upper panel of Fig. 5) is presented in Fig. 7 for different inclination angles, together with the observations of Prieto et al. (2010). In order to reproduce the observed silicate absorption at $12 \mu\text{m}$, we added a homogeneous screen of cold dust and varied its optical depth. It turned out that a screen with $\tau_V = 20$ reproduced the silicate feature for both AGN, Circinus and NGC 1068. This optical depth is typical for galactic giant molecular clouds. The observed MIR flux densities at wavelengths $\leq 20 \mu\text{m}$ are well reproduced by the model. The observed FIR flux densities were obtained from large apertures and have thus to be considered as upper limits. The model NIR

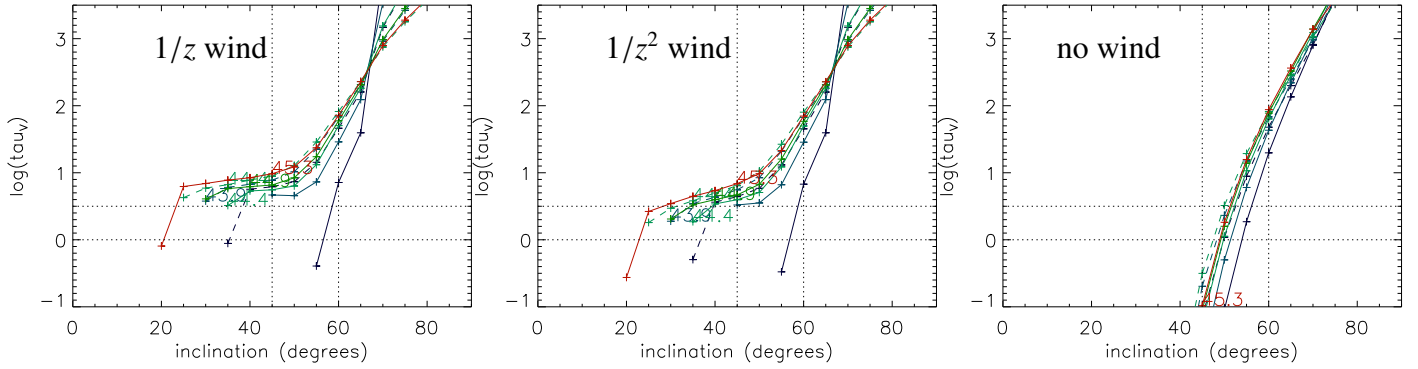


Fig. 6. Optical depth τ_V as a function of the inclination angle of the gas disk. The colors correspond to different bolometric luminosities. *Left panel:* wind with $1/z$ density profile. *Middle panel:* wind with $1/z^2$ density profile. *Right panel:* no wind component. The numbers indicate the logarithm of the bolometric luminosities of the models in erg s^{-1} . The horizontal dotted lines correspond to $\tau_V = 1$ and 3 , i.e., the transition from type 1 to type 2 objects. The vertical dotted lines correspond to the range of inclination angles where the degree of polarized optical emission changes from type 1 to type 2 objects (Marin 2014).

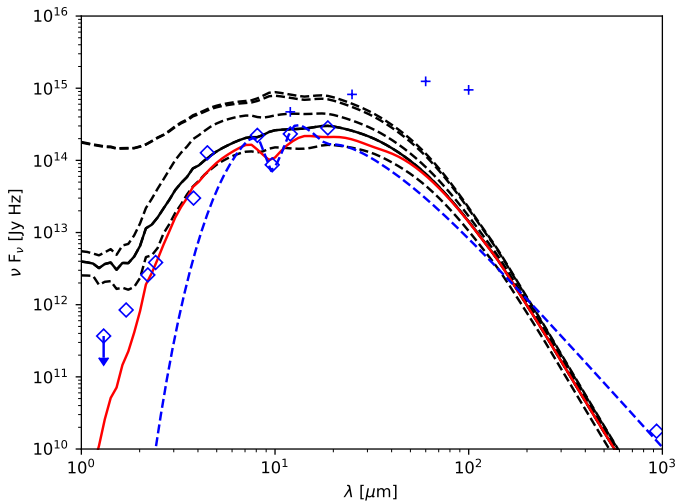


Fig. 7. SED of the radiative transfer Circinus model for different inclination angles of the gas disk (solid red line: best-fit model with $i = 65^\circ$ and with a homogeneous screen of $\tau_V = 20$; solid black line: $i = 65^\circ$ without a homogeneous screen; dashed black lines: $i = 0, 30, 60$, and 90° ; blue dashed line: Tristram et al. 2014 model). Blue diamonds: observations from Prieto et al. (2010). The typical uncertainties are on the order of 10%. Blue pluses: low resolution IRAS photometry. These points can be regarded as upper limits.

emission below $2 \mu\text{m}$ is overestimated by an order of magnitude. It is not excluded that this is due to a much lower intrinsic NIR luminosity. This would imply that the central thick gas ring, as assumed by the present model (see Sect. 3), does not exist in the Circinus galaxy. The observed silicate absorption feature at $12 \mu\text{m}$ is not reproduced by the model without a cold dust screen, because directly illuminated regions of the wind component, which are not extinguished by foreground dust, dominate the emission at this wavelength. The screen has to be located within the nuclear region ($< a$ few pc) since at slightly larger scales the polar region is well visible in optical emission lines such as [OIII] (Fig. 5 of Wilson et al. 2000), which means that there cannot be much dust located in front of the outer parts of the polar wind. Alternatively, the screen might have a larger extent if it becomes clumpy or patchy at higher altitudes.

Wada et al. (2016) used 3D radiation-hydrodynamic simulations to study the structure of a gas disk and an associated outflow around a low-luminosity AGN. Their IR SED is well comparable to our results between 1 and $10 \mu\text{m}$, but has higher

flux densities between 10 and $100 \mu\text{m}$. Motivated by high-quality VLT VISIR MIR imaging, Stalevski et al. (2017) proposed a phenomenological dust emission model for the AGN in the Circinus galaxy consisting of a compact dusty disk and a large-scale dusty cone shell, illuminated by a tilted accretion disk with an anisotropic emission pattern. Our model geometry is closest to their hyperbolic geometry. For a realistic comparison with observations, Stalevski et al. (2017) needed a foreground screen with an optical depth of $\tau_V = 34$, which is consistent with the optical depth of our model screen ($\tau_V = 20$). The resulting IR SED is well comparable to our results.

The spectral energy density distribution for the radiative transfer NGC 1068 model (lower panel of Fig. 5) is presented in Fig. 8 for different inclination angles. The MIR flux densities between $5 \mu\text{m}$ and $15 \mu\text{m}$ are well reproduced by the model. The model $\sim 20 \mu\text{m}$ flux densities are about 50% higher than the observed flux densities. The NIR flux density of the model with an additional screen of $\tau_V = 20$ is more than a factor of ten lower than the observed flux densities. This can be explained by additional stellar continuum emission.

We conclude that our model reproduces the observed IR SED in a satisfactory way. The absence of the silicate absorption feature is due to the absence of sufficient dust absorption of the emission from directly illuminated surfaces of the wind component. A cold dust screen with $\tau_V \sim 20$ can provide the necessary extinction to create the observed silicate absorption features.

4.3. Infrared luminosities

Burtscher et al. (2015) combines two approaches to isolate the AGN luminosity at near-IR wavelengths and relate the near-IR pure AGN luminosity to other tracers of the AGN. They showed that a significant offset exists between type 1 and type 2 sources in the sense that type 1 sources are about ten times brighter in the NIR than in the MIR. We think that the models of the two AGN bracket the range of observed local AGN population in terms of black hole mass, rotation velocity, and bolometric luminosity. Therefore, we assumed a fixed gas distribution for the low and high mass accretion case and illuminate them with different bolometric luminosities. In the following we compared the resulting model MIR and NIR luminosities to observations.

4.3.1. Isotropic illumination

The 3D models described in Sect. 3 were isotropically illuminated by a central AGN with different bolometric luminosities:

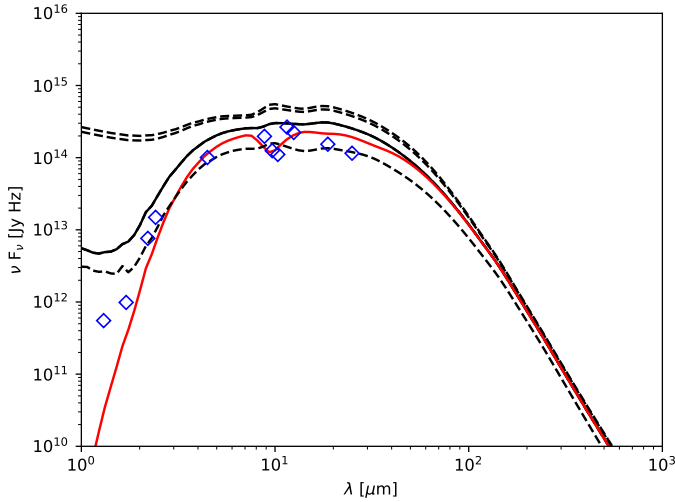


Fig. 8. SED of the radiative transfer NGC 1068 model for different inclination angles of the gas disk (red solid line: best-fit model with $i = 60^\circ$ and with a homogeneous screen of $\tau_v = 20$; black solid line: $i = 60^\circ$ without a homogeneous screen; dashed black lines: $i = 0, 30$, and 90°). Blue diamonds: observations from Prieto et al. (2010). The typical uncertainties are on the order of 10%.

$(\frac{1}{9}, \frac{1}{3}, 1) \times 8 \times 10^{44}$ erg s $^{-1}$ for Circinus and $(\frac{1}{9}, \frac{1}{3}, 1, 3, 9) \times 8 \times 10^{44}$ erg s $^{-1}$ for NGC 1068. For each bolometric luminosity we calculated the MIR and NIR luminosities with the radiative transfer model at 10 μ m and 2 μ m. To be consistent with Bartscher et al. (2015), we use monochromatic luminosities $L_{IR} = \nu \times \int I_\nu dA$, where ν corresponds to the central frequency of the band. To study the contribution of the magnetocentrifugal wind on the MIR and NIR luminosities, we calculated the following three different kinds of models:

1. wind with $1/z$ density profile,
2. wind with $1/z^2$ density profile, and
3. no wind.

Since we observed only minor differences between the MIR/NIR emission of the models with a $1/z$ and a $1/z^2$ wind, we show our results for the $1/z^2$ wind in Appendix B. The model MIR luminosities as a function of the bolometric luminosity are presented in Fig. 9. Without a wind component, the model MIR luminosities are about a factor of three smaller than the bolometric luminosities for type 1 objects. Type 2 objects nevertheless show a smaller ratio between the MIR and the bolometric luminosity compared to type 1 objects (right panel of Fig. 9). The situation changes with the addition of wind component: in type 1 objects the ratio between the MIR and bolometric luminosity is about $\frac{2}{3}$, that of type 2 objects about $\frac{1}{2}$ to $\frac{1}{10}$. Overall, the MIR luminosities of type 2 objects are about a factor of two lower than those of type 1 objects. The differences between the $1/z$ and $1/z^2$ models are minor for the MIR luminosity (~ 0.2 dex). The MIR luminosities are thus approximately proportional to the bolometric luminosity, because the wind component extends to high latitudes where the absorption by the thick gas disk is low even for an inclination angle of 60° . The comparison between the models with and without a wind component shows that the MIR luminosities of the thick gas disk and the wind are comparable. As expected, the exact location of the puff-up does not significantly modify the MIR luminosities (Fig. B.2). The model L_{MIR}/L_{bol} ratios of ≤ 0.5 are significantly higher than the observed ratios of 0.06–0.17 (Gandhi et al. 2009; Asmus et al. 2015). These ratios rely on the L_X/L_{bol} relation found by Marconi et al. (2004). On the other hand, based on high resolution IR

observations of three local type 1 AGN Prieto et al. (2010) found ratios of $L_{MIR}/L_{bol} = 0.12$ – 0.28 . Their bolometric luminosities are directly derived from the SEDs. Thus, our model L_{MIR}/L_{bol} ratios are at least a factor of two higher than the ratio derived from observations. It is expected that a slightly different geometry of the inner wall of the thick gas disk (a convex instead of a plane surface) and a clumpy wind decrease L_{IR}/L_{bol} . We note that an additional screen of optical depth $\tau_v = 20$ (Sect. 4.2) leads to a decrease of the MIR luminosity by a factor of two.

The model NIR luminosities as a function of the bolometric luminosity are presented in Fig. 10. The bulk of the NIR emission is produced close to the inner edge of the thin disk, that is, the sublimation radius, consistent with observations (continuum reverberation mapping: e.g., Suganuma et al. 2006; interferometry: e.g., Kishimoto et al. 2011). Without a wind component, the model NIR luminosities are about 50% higher than those of the model with a wind component for type 1 objects, because the wind provides a nonnegligible NIR extinction. As expected, the NIR luminosities decrease significantly once the inner thin gas disk is hidden by the thick gas disk. We observe a less significant drop of the NIR luminosities for high inclination angles ($i > 65^\circ$) in the presence of a wind. We interpret the additional NIR emission as the contribution of the unobscured basis of the wind to the NIR emission. Whereas the ratio between the NIR and bolometric luminosity is about 1/10 for the basic wind model, it increases by a factor of ~ 1.5 and ~ 2 when the puff-up is located at a $\sqrt{2}$ and 2 times smaller distance from the central black hole (Fig. 11). The increase of the NIR luminosity due to higher dust temperatures is stronger than the decrease due to the smaller area where hot dust can be found.

The NIR luminosities as a function of the MIR luminosities are presented in Fig. 12. As for the previous correlations, the differences between the $1/z$ and $1/z^2$ models are minor. Whereas type 1 objects show NIR/MIR ratios between 0.5 and 1, the NIR luminosities of type 2 models are more than five times smaller than the MIR luminosities. For luminosities smaller than 10^{44} erg s $^{-1}$ and inclination angles between 50° and 60° the MIR/NIR luminosity ratio is about ten. The model with an inner radius located at $2 \times r_{sub}$ (right panel of Fig. 13) reproduces the observations of Bartscher et al. (2015) best.

As a last step, we compared our model results to the correlation between the MIR and the X-ray luminosities (Asmus et al. 2015). These authors found that the MIR–X-ray correlation is nearly linear and within a factor of two; independent of the AGN type and the wavebands used. The observed scatter of the correlation is < 0.4 dex. We calculate the X-ray luminosity by assuming that the intrinsic X-ray luminosities of all models is 1/10 of the bolometric luminosity (Marconi et al. 2004). Assuming that the 1–10 keV emission becomes optically thick at $N \sim 10^{24}$ cm $^{-2}$ (which corresponds to $\tau_v = 500$), the observed X-ray luminosity is then calculated via

$$L_X = \frac{1}{10} \times L_{bol} \exp\left(-\frac{\tau_v}{500}\right). \quad (43)$$

The results are presented in Fig. 14. Since the MIR luminosity integrated over a solid angle of 4π is the reprocessed fraction of the bolometric accretion disk luminosity, it is proportional to the covering factor. On the other hand, the observed MIR luminosity depends on the viewing angle (Fig. 9; a factor of two or more for $i \gtrsim 60^\circ$). It is thus trivial that both wind models reproduce the observed MIR–X-ray correlation within a factor of two. The scatter of the model correlation is determined by the viewing angle through the absorption of the MIR and X-ray emission.

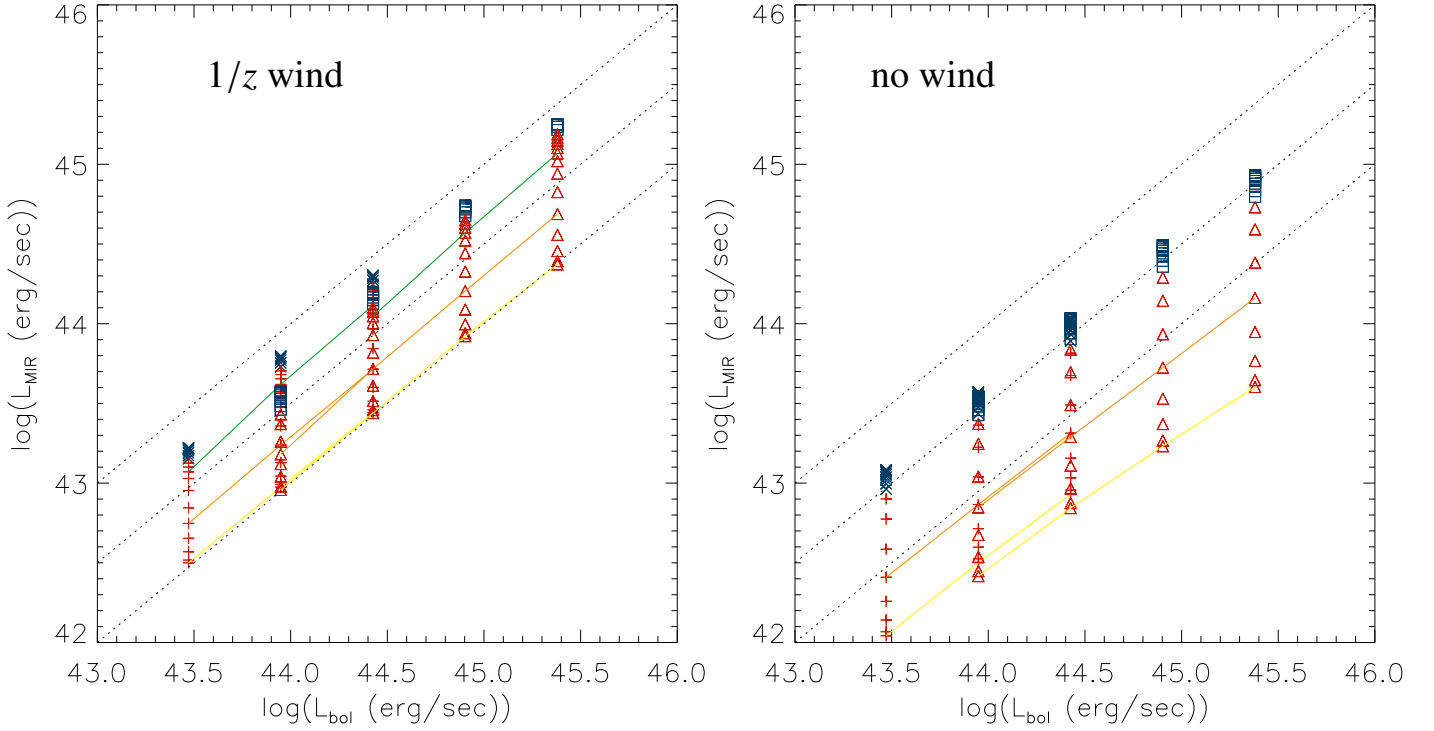


Fig. 9. Model MIR luminosities as a function of the bolometric luminosity. Blue color represents type 1 objects, red represents type 2. The Circinus model is shown with crosses and pluses; NGC 1068 model with squares and triangles. The inclination angles of type 2 objects are indicated: $i = 50^\circ$ (green line), $i = 70^\circ$ (orange line), $i = 90^\circ$ (yellow line). *Left panel:* wind with $1/z$ density profile. *Right panel:* no wind component. The dotted lines correspond to $L_{\text{MIR}} = \xi L_{\text{bol}}$ with $\xi = 1, 1/3$, and $1/10$.

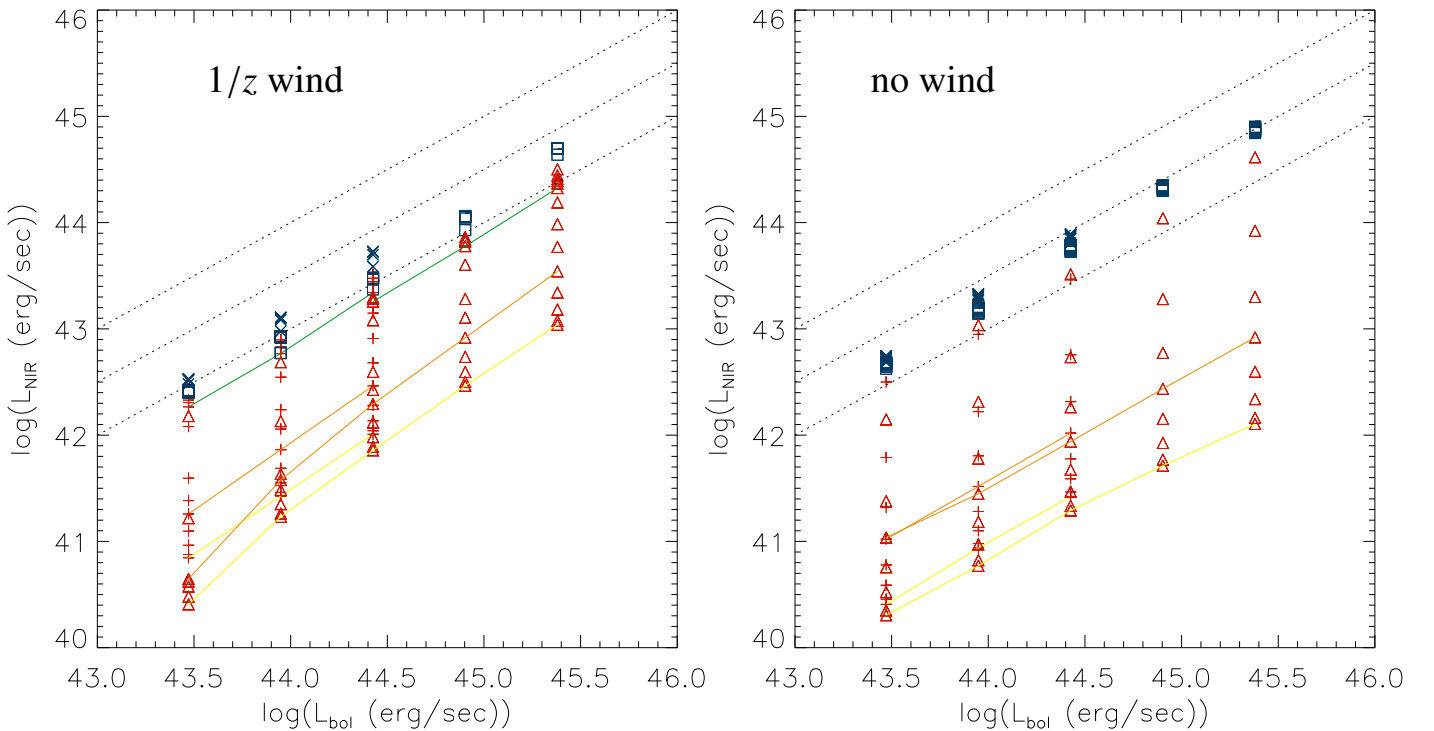


Fig. 10. Model NIR luminosities as a function of the bolometric luminosity. Blue represents type 1, red represents type 2. The Circinus model is shown with crosses and pluses; the NGC 1068 model with squares and triangles. The inclination angles of type 2 objects are indicated: $i = 50^\circ$ (green line), $i = 70^\circ$ (orange line), $i = 90^\circ$ (yellow line). *Left panel:* wind with $1/z$ density profile. *Right panel:* no wind component. The dotted lines correspond to $L_{\text{NIR}} = \xi L_{\text{bol}}$ with $\xi = 1, 1/3$, and $1/10$.

The scatter of the L_{MIR}/L_X ratio is 0.3 dex for the wind model and 0.25 dex for the model without a wind component. If we take into account that the probability of a galaxy that is observed with an inclination angle i is proportional to the solid angle around

that angle (in our case $i \pm 5^\circ$), we obtain a scatter of 0.36 dex and 0.30 dex, respectively. With a variation or scatter of the L_X/L_{bol} ratio of 0.3 dex (Marconi et al. 2004), we obtain a total scatter of 0.42/0.39 dex or 0.47/0.42 dex for the models with and without

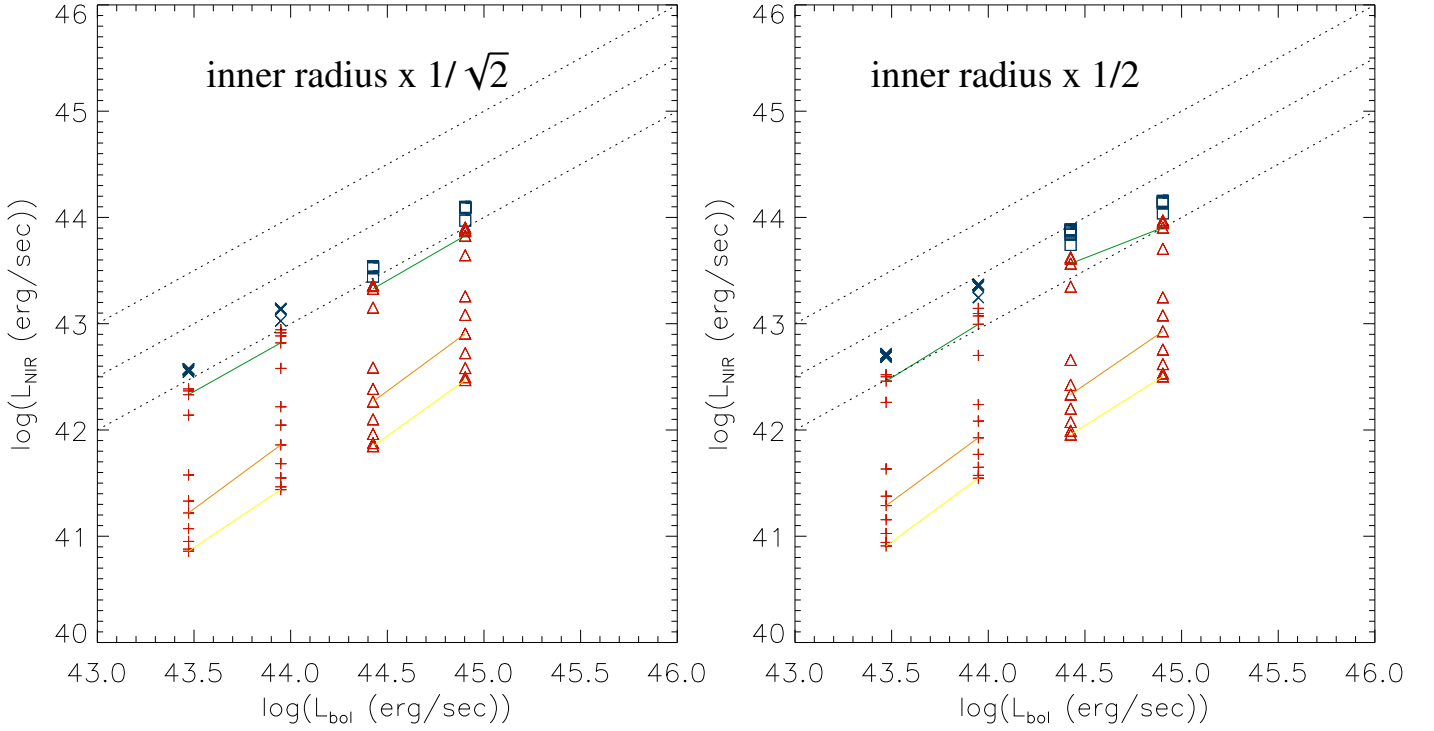


Fig. 11. Model NIR luminosities as a function of the bolometric luminosity for the $1/z$ winds for a $\sqrt{2}$ (left panel) and 2 (right panel) times smaller inner radius of the thin gas disk. The dotted lines correspond to $L_{\text{NIR}} = \xi L_{\text{bol}}$ with $\xi = 1, 1/3$, and $1/10$.

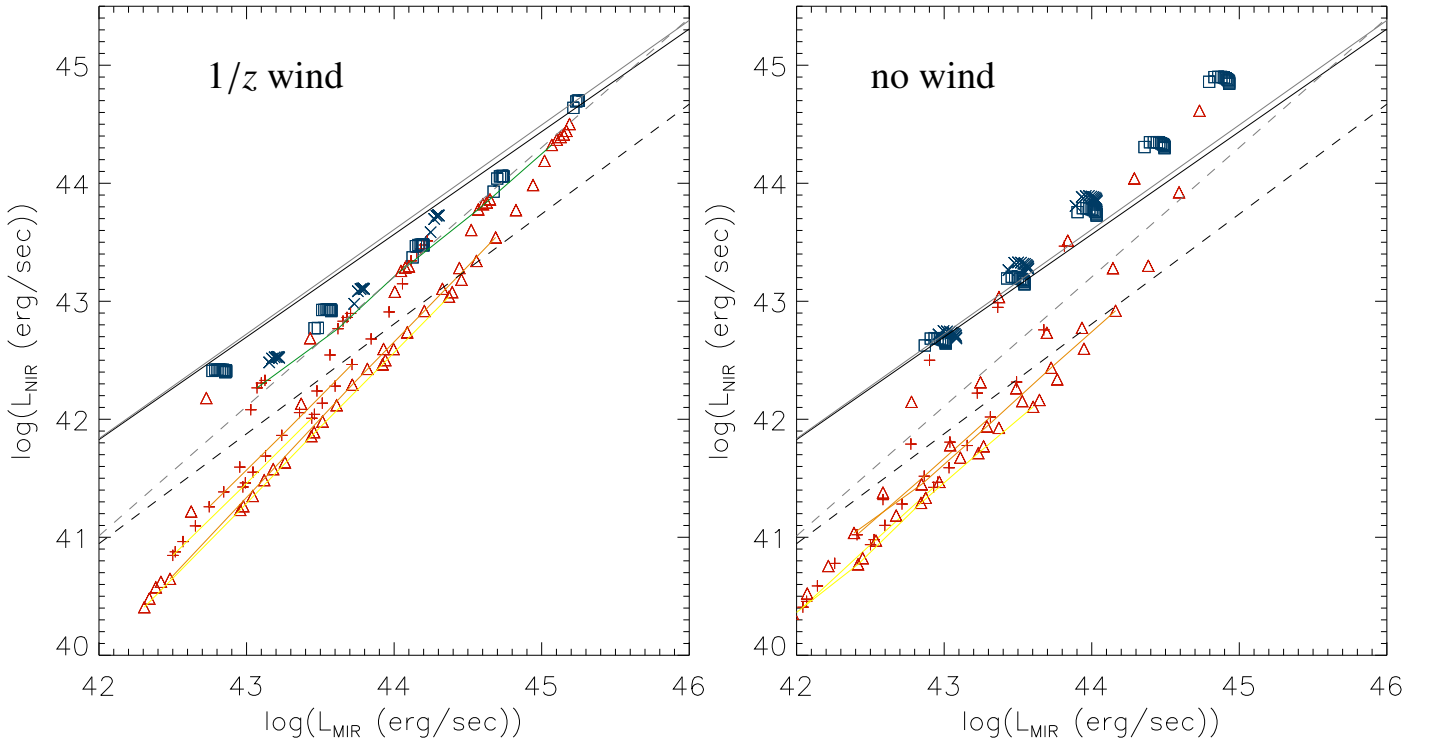


Fig. 12. Model NIR luminosities as a function of the MIR luminosity. Blue represents type 1, red represents type 2. The Circinus model is shown with crosses and pluses; the NGC 1068 model with squares and triangles. The inclination angles of type 2 objects are indicated: $i = 50^\circ$ (green line), $i = 70^\circ$ (orange line), $i = 90^\circ$ (yellow line). Left panel: wind with $1/z$ density profile. Right panel: no wind component. The solid and dashed lines are the relations found by Burtcher et al. (2015) for type 1 and type 2 objects, respectively.

a wind, respectively. Surprisingly, all these values are comparable to that of the observations (0.39 dex; Asmus et al. 2015). The reason for the tightness of the correlation even without a wind component is found in the high column densities of the absorbing disk material that also decreases the X-ray emission together

with the MIR emission. Therefore, the wind component is not mandatory to reproduce the scatter of the $L_{\text{MIR}}-L_{\text{X}}$ correlation.

Only objects with $i \geq 70^\circ$ deviate significantly (more than 0.3 dex) from the MIR–X-ray correlation, meaning that they show much smaller X-ray luminosities due to X-ray absorption

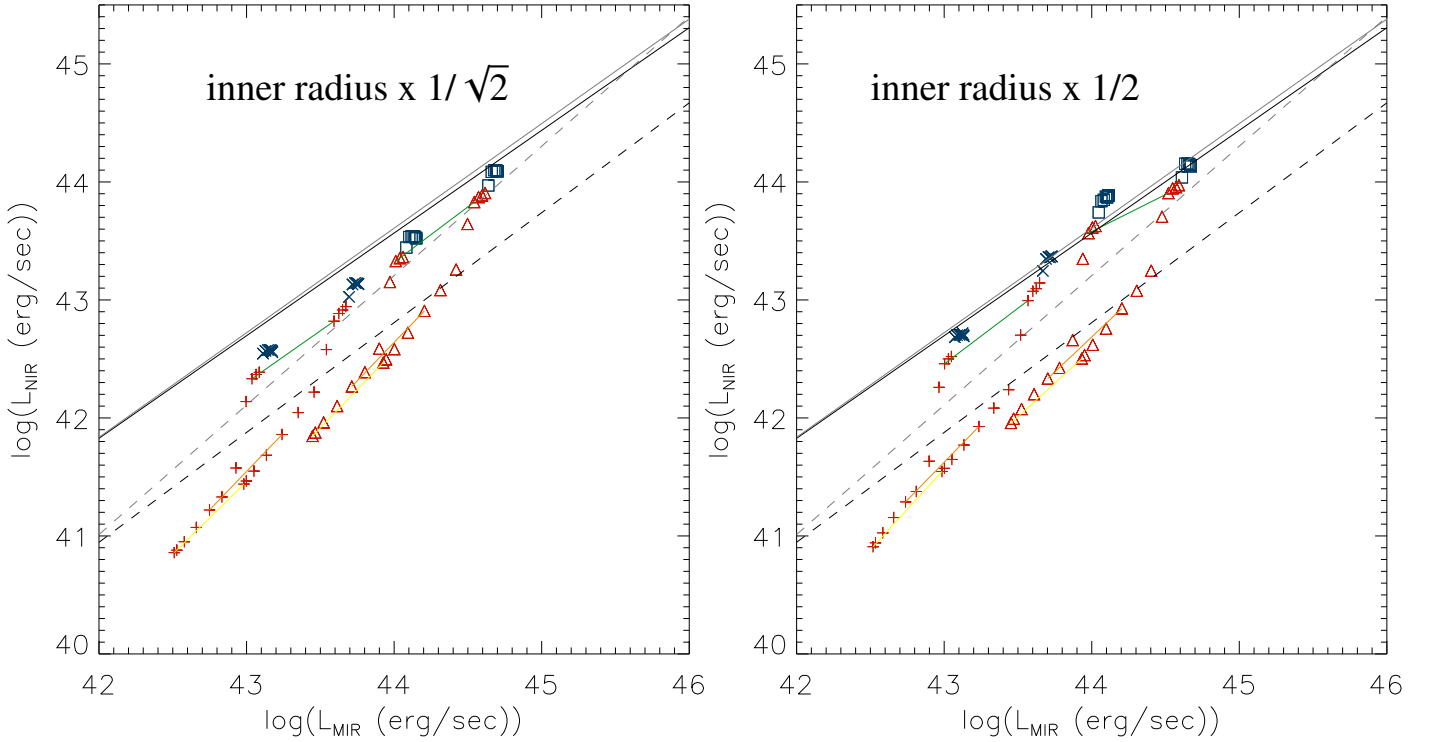


Fig. 13. Model NIR luminosities as a function of the MIR luminosity for the $1/z$ winds for a $\sqrt{2}$ (left panel) and 2 (right panel) times smaller inner radius of the thin gas disk. The solid and dashed lines are the relations found by Burtscher et al. (2015) for type 1 and type 2 objects, respectively.

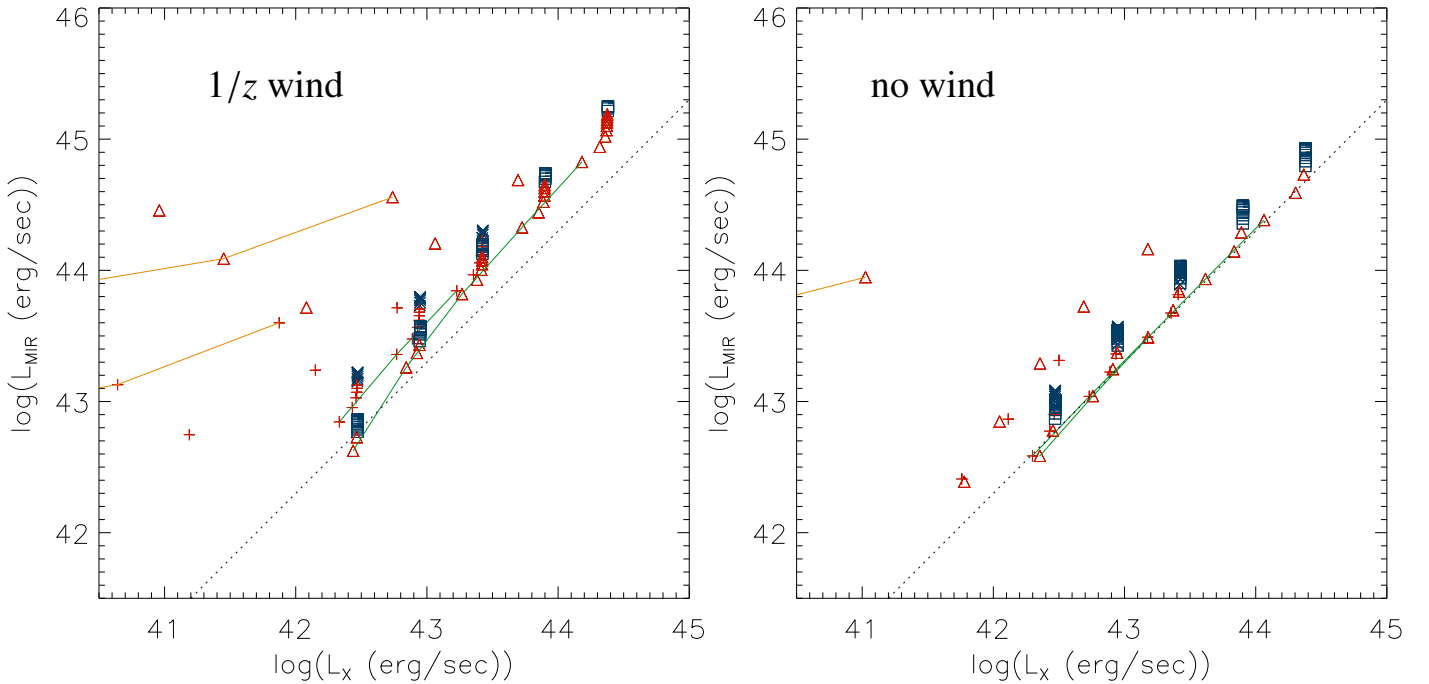


Fig. 14. Model MIR–X-ray correlation. Blue represents type 1, red represents type 2. The Circinus model is shown with crosses and pluses; the NGC 1068 model with squares and triangles. The inclination angles of type 2 objects are indicated: $i = 65^\circ$ (green line), $i = 75^\circ$ (orange line). Left panel: wind with $1/z$ density profile. Right panel: no wind component. The dotted line corresponds to the correlation found by Asmus et al. (2015): $\log(L_{\text{MIR}}) = \log(L_X) + 0.33$.

by the thick gas disk. In terms of solid angle, this means that less than 6% of all objects deviate significantly from the correlation. The same is found for the model without a wind component. By comparing the models with and without wind, it becomes clear that the wind enhances the MIR emission of type 2 objects.

As expected, a smaller distance of the puff-up from the central black hole does not significantly modify the model MIR–X-ray correlation.

The tightness of the MIR–X-ray correlation can be of different origins:

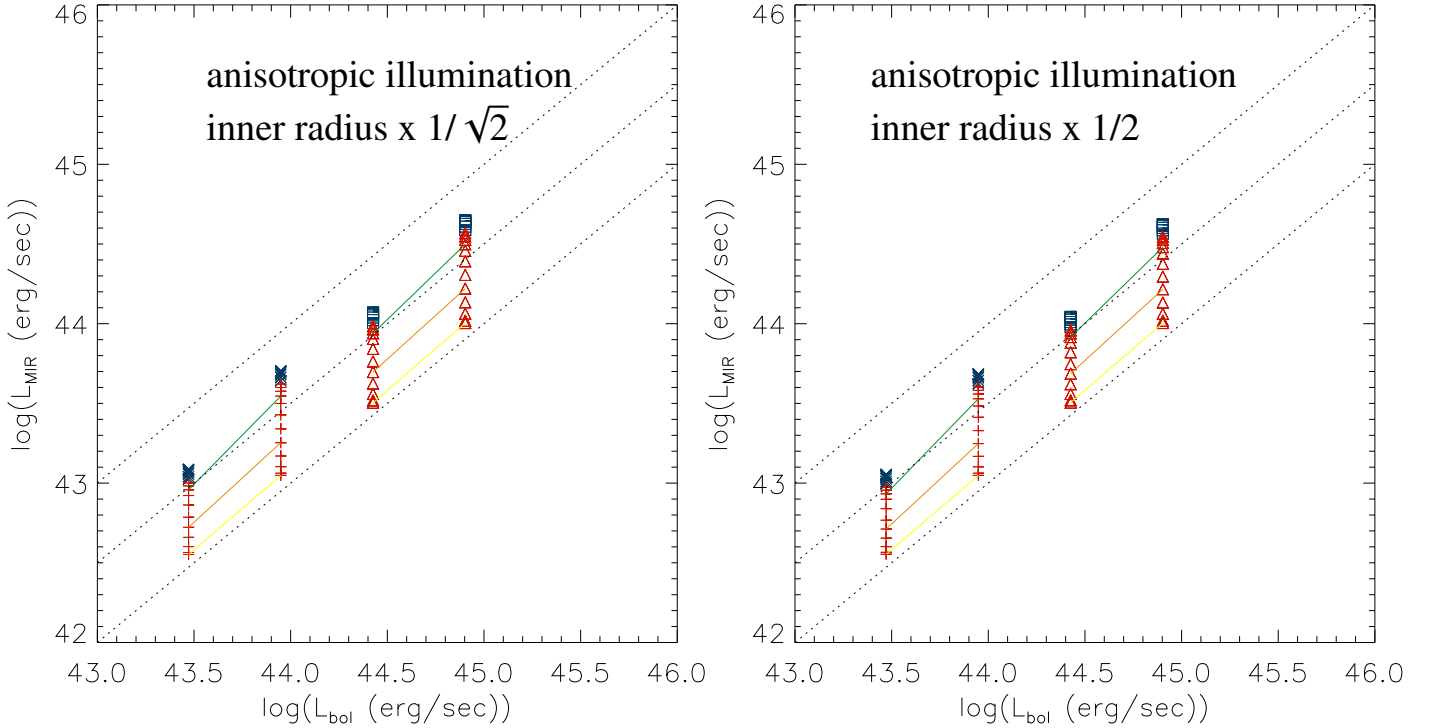


Fig. 15. Model MIR luminosities as a function of the bolometric luminosity for the $1/z$ winds with anisotropic illumination for a $\sqrt{2}$ (left panel) and 2 (right panel) times smaller inner radius of the thin gas disk. The dotted lines correspond to $L_{\text{MIR}} = \xi L_{\text{bol}}$ with $\xi = 1, 1/3$, and $1/10$.

- Extended polar MIR emission caused by a dusty wind (see, e.g., [Asmus et al. 2016](#)) making the total MIR emission more isotropic;
- massive and dense thick gas disk as proposed here. In this case an extended polar MIR emission is not mandatory;
- clumpy models of the gas and dust distribution with and without a wind component are also able to reproduce the observed MIR–X-ray correlation ([Hönig et al. 2011](#); [Hönig & Kishimoto 2017](#)). Clumpiness naturally increases the MIR isotropy;
- the X-ray emission might be mildly anisotropic ([Liu et al. 2014](#); [Sazonov et al. 2015](#); [Yang et al. 2015](#)).
- in the presence of a distribution of covering factors, type 1 or 2 sources will have a lower or higher covering factor respectively, because the probability to observe a certain type depends on the covering factor ([Elitzur 2012](#)). This naturally reduces the difference in IR emission between type 1 and type 2 sources.

We conclude that the density profile of the wind ($1/z$ or $1/z^2$) has a minor influence on the NIR and MIR luminosities. The existence of a wind component leads to MIR luminosities whose dependence on the inclination angle is relatively small. The NIR component stems mostly from the thin gas disk and is thus prone to extinction by the thick gas disk. The relation between the NIR and MIR luminosities (Fig. 13) is comparable to the observed relation ([Burtscher et al. 2015](#); Fig. 9).

4.3.2. Anisotropic illumination

In a second step, we illuminated the gas distribution with a $\cos(\theta)$ pattern which is caused by limb darkening of the hot accretion disk ([Netzer 1987](#)) located at a distance smaller than the dust sublimation radius. The natural consequence is that the thick gas disk and the basis of the wind receive less flux, whereas the upper wind regions receive somewhat more flux. The net

effect is a decreased MIR and NIR luminosity with respect to the isotropic illumination (Fig. 15). For these models, the MIR luminosity is about three times lower than that of the models with isotropic illumination. The ratio $L_{\text{MIR}}/L_{\text{bol}} \sim 1/5$ is still a factor of two higher than the value determined by [Gandhi et al. \(2009\)](#). Again, a screen with $\tau_V = 20$ (Sect. 4.2) leads to MIR luminosities two times lower. Given that the AGN sample of [Gandhi et al. \(2009\)](#) includes also type 2 objects, there is reasonable agreement between our model and observations.

Since the NIR is less affected by the change of the illumination pattern, the NIR to MIR luminosity ratio increases with respect to the models with isotropic illumination (Fig. 16). The model with the puff-up being located at $3 \times r_{\text{sub}}$ (left panel of Fig. 16) reproduces the observations of [Burtscher et al. \(2015\)](#) best.

We conclude that for the population of local AGN observed by [Burtscher et al. \(2015\)](#) the $\cos(\theta)$ illumination seems to be preferred over the isotropic illumination.

4.4. Point source fraction

The detailed geometry of the (sub-)parsec scale dust distribution, that is, the multicomponent structure as well as sizes, elongations and position angles of the components, can be observationally best constrained in the two MIR brightest objects, Circinus and NGC 1068. The basic nuclear dust structure has been determined in another two dozen objects, though ([Burtscher et al. 2013](#), see also [Hönig et al. 2012, 2013](#)). The most straight-forward observable in these objects is the visibility at long baselines, indicating how well a source is resolved on scales of about $6 r_{\text{in}}$ (Fig. 17). This highest-resolution visibility or “point-source fraction” is a robustly measured quantity (uncertainty $\sim 5\%$) and can be compared directly against our disk-wind model (Fig. 18).

The model point source fraction is defined as the flux density in the inner $N r_{\text{in}}$ divided by the total flux density of the image. In

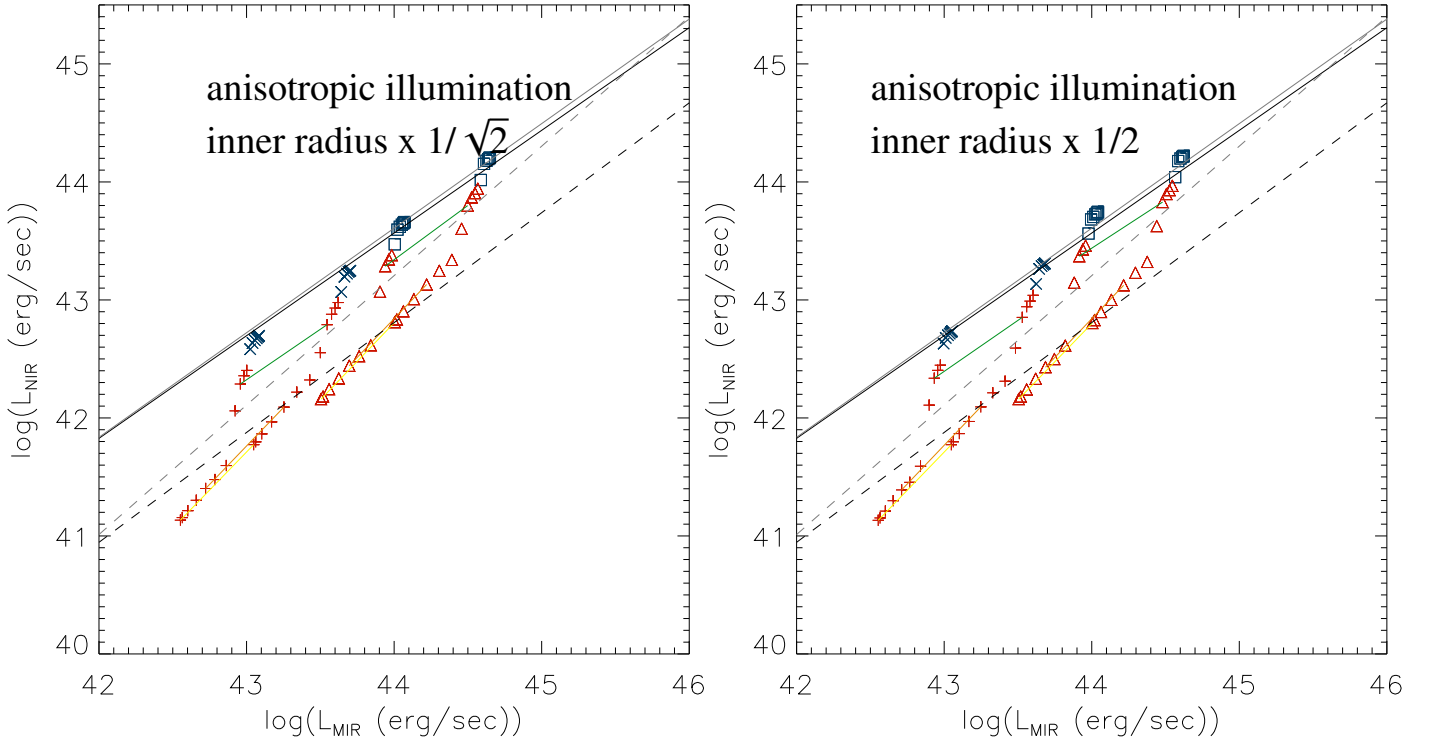


Fig. 16. Model NIR luminosities as a function of the MIR luminosity for the $1/z$ winds with anisotropic illumination for a $\sqrt{2}$ (left panel) and 2 (right panel) times smaller inner radius of the thin gas disk. The solid and dashed lines are the relations found by Burtcher et al. (2015) for type 1 and type 2 objects, respectively.

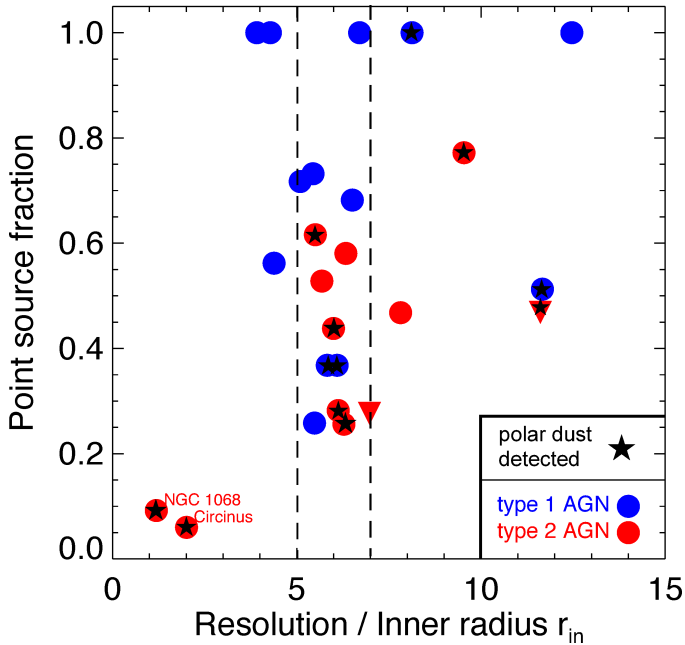


Fig. 17. Point source fraction for the MIR interferometric observations of Burtcher et al. (2013). Only objects around $6 r_{\text{in}}$ should be compared to Fig. 18. Objects with detected extended dust emission are marked with a star. This emission is mostly in polar direction, i.e., the direction of the narrow line region, and was detected on 10 pc-scale (López-Gonzaga et al. 2016 and references therein) and on 100 pc-scale (Asmus et al. 2016), but not for the same objects. We note that the detectability of polar dust emission depends on a number of observational parameters and nondetections do not mean that these AGNs are intrinsically different.

the observations of Burtcher et al. (2013) $N = 6$ for the majority of AGNs of their sample. For all models described in Sect. 4.3.1 we calculated the point source fraction for $N = 6$. In addition, we determined the point source fractions of the Circinus model at $i = 70^\circ$ ($N = 2$) and the NGC 1068 model at $i = 60^\circ$ ($N = 1$). Our model point source fractions of Circinus and NGC 1068 agree with the observed point source fractions.

We see a clear dependence of the point-source fraction on the inclination of the model. In addition, the model point source fraction of type 1 objects depends on the bolometric luminosity, that is, the point source fraction increases with increasing luminosity. In order to see if such a trend also exists in the data of Burtcher et al. (2013), we show the point source fraction as a function of the bolometric luminosity in Fig. 19. The type 1 objects with $r = 6 \times r_{\text{sub}}$ (triangles) indeed reproduce the observed increase of the point source fraction with increasing bolometric luminosity. This is caused by the increase of the sublimation radius with $\sqrt{L_{\text{bol}}}$, whereas the inner illuminated edge of the thick disk and the high-density part of the wind are located at a constant radius. If most of the IR luminosity is produced within an area that is close to the inner edge of the thick disk, an increase of the beam width with a constant size of the major IR emitting region leads to an increasing point source fraction. Once the physical size that corresponds to the resolution (FWHM) of the interferometric observations with the longest baselines is about four times the radius of the inner edge of the thick gas disk, the point source fraction becomes ~ 0.5 .

Point source fractions > 0.7 are only observed in models without a wind, high bolometric luminosities, and $r = 9 \times r_{\text{sub}}$ (Fig. C.1). In type 1 objects with point source fractions close to unity even the thick gas disk is absent. The variety of point source fractions ($0.25 \leq f_p \leq 0.75$) for type 1 and type 2 objects

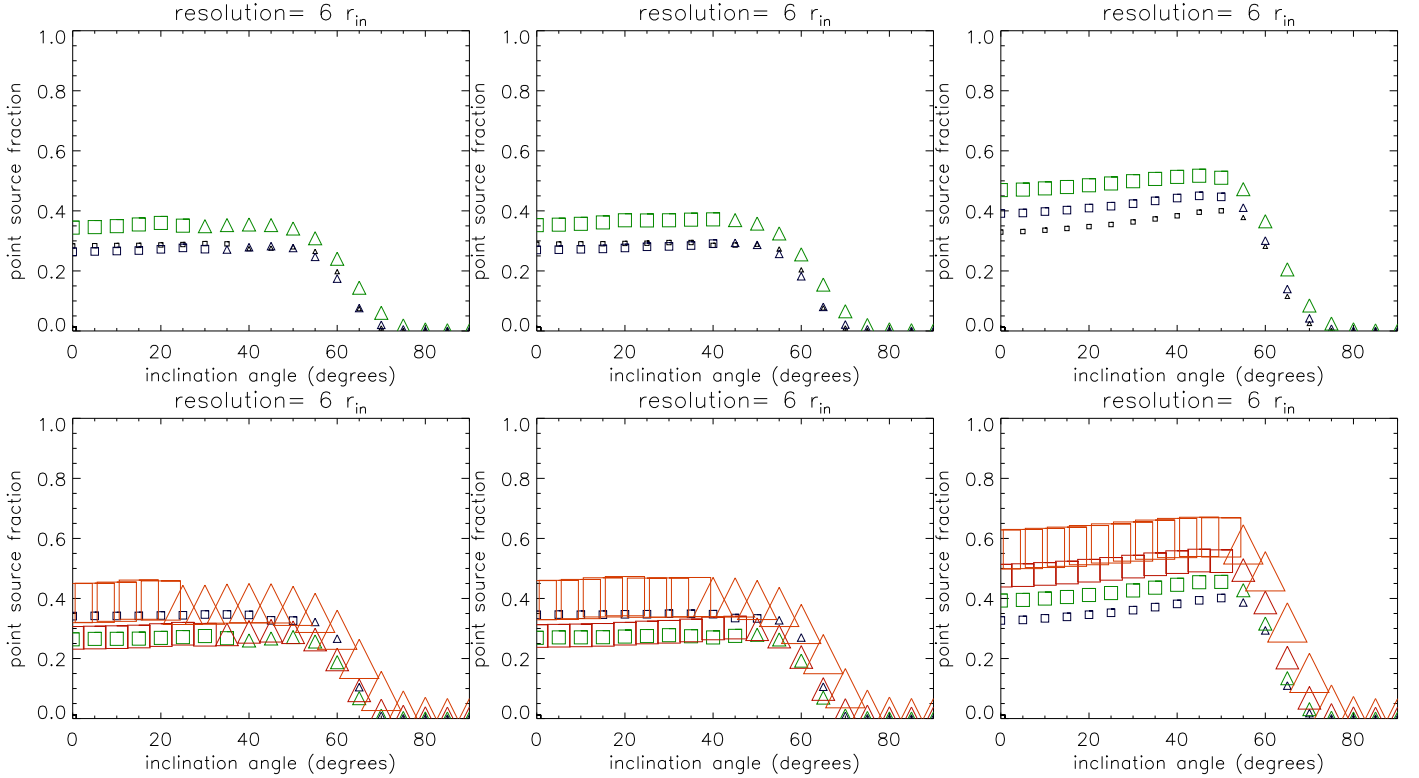


Fig. 18. Point source fraction ($6r_{in}$) for the Circinus model (upper row) and NGC 1068 model (lower row). *Left column:* $1/z$ wind (standard model). *Middle column:* $1/z^2$ wind. *Right column:* no wind. Boxes represent type 1 objects and triangles type 2 objects. The size of the symbols is proportional to the bolometric luminosity.

might thus be caused by luminosity effects for type 1 objects and inclination effects for type 2 objects. Moreover, we argue that observed point source fractions of approximately one (Fig. 17) in type 1 AGNs indicate the absence of a polar wind. In quasars, where strong outflows are detected (e.g., Feruglio et al. 2010), the winds can also have an equatorial geometry (e.g., Elvis 2000).

5. Infrared interferometry

In this section we compare the model visibility amplitudes of the radiative transfer models to existing MIR observations.

5.1. From images to visibility amplitudes

We compared our model images to observations of the actual geometry of the circum-nuclear region. At infrared wavelengths, especially in the MIR atmospheric N band window (8–13 μm), the emission of radio-quiet AGNs is dominated by the thermal radiation of dust. We can therefore directly compare the radiative transfer of our model dust distributions with high-resolution IR observations of AGNs. Since the circum-nuclear dust distributions even in the most nearby AGNs are essentially unresolved with single-dish telescopes, IR long-baseline interferometry is required to probe their geometry. Successful observations of more than two dozen of nearby AGNs have been obtained in the NIR and MIR (see Burtscher et al. 2016 for a recent review). The most detailed studies have been possible with MIDI at the VLTI for the two brightest objects NGC 1068 (López-Gonzaga et al. 2014) and in the Circinus galaxy (Tristram et al. 2014).

The result of these observations are visibility amplitudes, which themselves need to be compared to model images to constrain the actual surface brightness of the (sub-)parsec region.

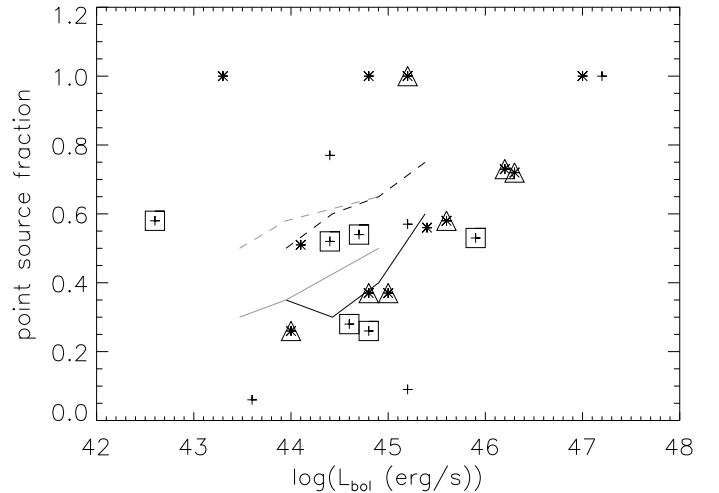


Fig. 19. Observed point source fraction as a function of the bolometric luminosity. Pluses show type 2 objects. Stars show type 1 objects. Triangles show type 1 objects with point source fluxes within $(6 \pm 1) \times r_{sub}$. Squares show type 2 objects with point source fluxes within $(6 \pm 1) \times r_{sub}$. The dark solid line is the NGC 1068 model with $r = 6 \times r_{sub}$. The gray solid line is the NGC 1068 model with $r = 9 \times r_{sub}$. The dark dashed line is the Circinus model with $r = 6 \times r_{sub}$. The gray dashed line is the Circinus model with $r = 9 \times r_{sub}$.

To be closer to observations, we compare the MIDI observations directly to visibilities derived from the model images of our disk-wind model. The visibility amplitudes are computed from the model images by means of a Fourier transform with proper scaling. To facilitate the comparison between model images and observed visibility data, we have created a Python class,

Table 3. Circinus models.

Model	Illumination	Spatial scaling	Inclination	χ^2	$\chi^2/\chi^2_{\text{Tristram}}$	Fig.
Tristram et al. (2014)	–	1.0	–	11 681	1.0	D.1
Radiative transfer model	isotropic	1.0	70°	29 637	2.5	20
RT model with corotating helical wind	isotropic	1.0	70°	25 159	2.2	22

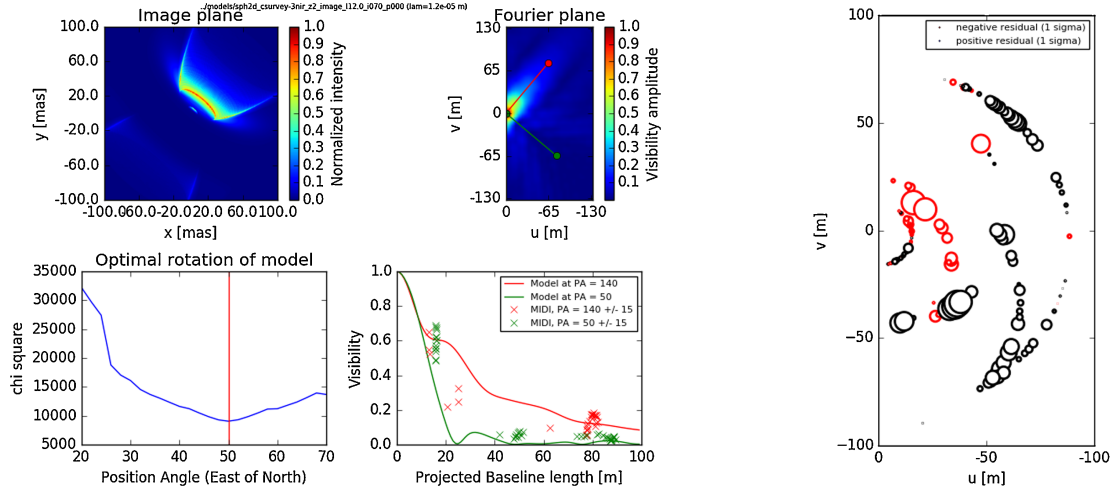


Fig. 20. Radiative transfer model for Circinus. *Upper left panel:* image at 12 μm . *Upper middle panel:* visibility amplitudes. *Lower left panel:* χ^2 as a function of position angle. *Lower middle panel:* visibility amplitudes as a function of projected baseline length (solid lines: model, crosses: observations). *Right panel:* difference between the model and observed visibility amplitudes (red: (model-observations) > 0, black: (model-observations) < 0). The size of the rings is proportional to the value of the residual.

*img2vis*⁴. This class takes a model image with a given pixel scale and wavelength, converts it into visibility amplitudes (on the so-called (u, v) plane) and compares the results with observations given as an “OIFITS” file. With the uncertainties associated to the visibility amplitudes, the χ^2 of each model is calculated.

For each AGN we calculated the following model series

1. symmetric radiation transfer (RT) model with $1/z$ wind and puff-ups at $2, 3, 4 \times r_{\text{sub}}$ and isotropic illumination,
2. symmetric RT model with $1/z$ wind and puff-ups at $2, 3, 4 \times r_{\text{sub}}$ and $\cos(\theta)$ illumination,
3. symmetric RT model with $1/z$ wind and a helical wind component (Sect. 5.2.3).

For each model series we varied the inclination angle (0° – 90°) and the spatial scaling (0.5, 0.75, 1.0, 1.25, and 1.5).

5.2. Application of the model

In the following we compare our model series of the Circinus galaxy and NGC 1068 with IR-interferometry observations. All model images were produced at wavelengths of 8, 9, 10, 11, and 12 μm . Since our model does not contain an intrinsic silicate absorption feature and this seems to pose a problem for NGC 1068 at 9 μm (an exceedingly high χ^2 compared to the χ^2 at the other wavelengths), we decided to calculate the corresponding χ^2 only at 8, 10, 11, and 12 μm .

5.2.1. Circinus

For each model series, we selected the model with the lowest χ^2 (Table 3). All RT model χ^2 are normalized with that of the Tristram et al. (2014) model: χ^2_{rel} . The best-fit model has

⁴ Available for download at <https://github.com/astroleo/img2vis>

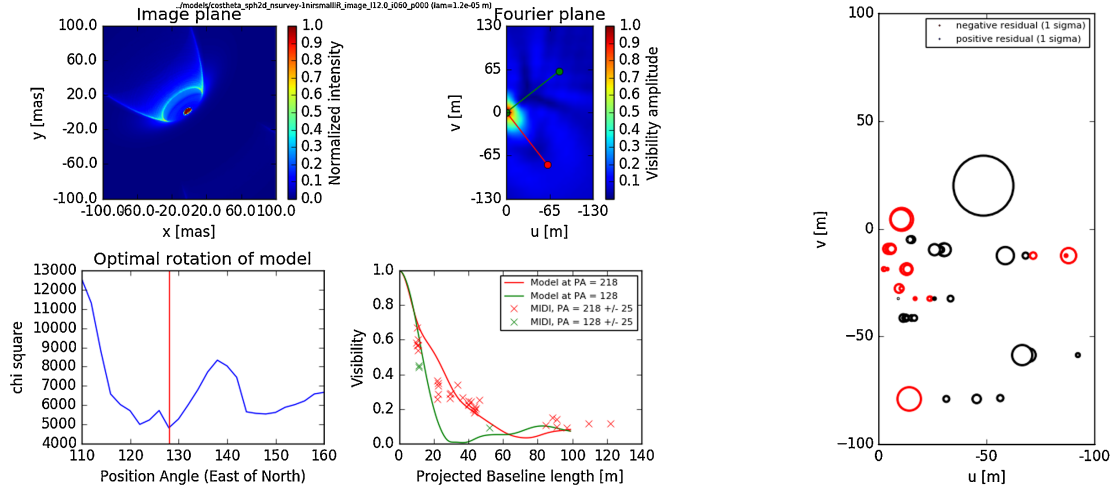
an isotropic illumination, an inclination angle of $i = 70^\circ$ and $\chi^2_{\text{rel}} = 2.5$. In Fig. 20 we show the comparison for our standard model (including a $1/z$ wind). For comparison, Fig. D.1 shows the result for the Tristram et al. (2014) model. The corresponding comparisons at 8 μm and 10 μm are shown in Figs. D.2 and D.3. We show only the negative u axis of the Fourier plane since the Fourier transform of a real-valued image is axis-symmetric. To find the best-fitting solution, we rotate the model image in position angle (lower-left plot). Two cuts through the model image (“radial plots”) with according observations are shown in the lower-middle plot and a comparison of the residuals on the (u, v) plane is shown on the right.

Overall, the model reproduces the observed visibility amplitudes in an acceptable way. In particular, the disk and wind model is able to explain the observed two-component structure which can be seen in the radial plots: the visibilities drop quickly up to a baseline length of about 20 m (indicating a large structure, here represented by the wind component) and then show some “wiggles” (modeled by the thin disk component). The range of observed visibilities at a baseline length just short of 20 m corresponds to different observed position angles and indicates a significant elongation of the large-scale component.

We conclude that the symmetric RT model reproduces the available interferometric observations in an acceptable way. Our model has a physical background with four components (puff-up, thin disk, thick disk, and wind component) whose extent and orientation cannot be varied. On the other hand, the Tristram et al. (2014) model contains three independent Gaussian components (but they also fitted the differential phases). We believe that a factor of two between the χ^2 of our model and that of Tristram et al. (2014) is acceptable. We derived an inclination angle of $i = 70^\circ$. Since the maser disk is most probably seen edge-on ($i = 90^\circ$), it must be tilted or warped with respect to the thick gas disk.

Table 4. NGC 1068 models.

Model	Illumination	Spatial scaling	Inclination	χ^2	$\chi^2/\chi^2_{\text{López-Gonzaga}}$	Fig.
López-Gonzaga et al. (2014)	—	1.0	—	6286	1.0	D.4
Radiative transfer model	$\cos(\theta)$	1.25	60°	17871	2.8	21
RT model with corotating helical wind	$\cos(\theta)$	1.25	60°	17239	2.7	23

**Fig. 21.** Same as Fig. 20 for the NGC 1068 radiative transfer model at $12\ \mu\text{m}$. The puff-up of the inner thin disk is located at $r = 3 \times r_{\text{sub}}$.

5.2.2. NGC 1068

As for Circinus, we selected the model with the lowest χ^2 (Table 4). All RT model χ^2 are normalized with that of the López-Gonzaga et al. (2014) model. The best-fit model has a $\cos(\theta)$ illumination, an inclination angle of $i = 60^\circ$ and $\chi^2_{\text{rel}} = 2.8$ (Fig. 21). For comparison, Fig. D.4 shows the result for the López-Gonzaga et al. (2014) model. The corresponding comparisons at $8\ \mu\text{m}$ and $10\ \mu\text{m}$ are shown in Figs. D.5 and D.6. The thick gas disk of NGC 1068 is thus less inclined than that of Circinus, the relative χ^2 is comparable to that of Circinus. The inclination angle derived from the model is significantly different from the inclination angle derived by the fitting of the IR SED with a clumpy torus model (Hönig et al. 2008; $i = 90^\circ$). Since the inner thin disk, and especially its inner puff-up is visible in the model image, the exact location of the puff-up is important. It turned out that a radius of $r = 3 \times r_{\text{sub}}$ leads to the lowest χ^2_{rel} . This is consistent with the location of the puff-up determined by the IR luminosities (Sect. 4.3).

To investigate the influence of the wind component on the visibilities, we re-calculated the radiative transfer of our best-fit model with a dust-free wind, which is devoid of IR emission. The χ^2 of this model is 1.6 times higher than that of the model with a dusty wind. Most importantly, the emission distribution in the UV plane of the model with a dust-free wind is significantly more extended than that of the dusty wind model and observations, mainly in the polar direction but also in the direction of the disk plane. Our model is close to model 1 of López-Gonzaga et al. (2014): their first component corresponds to the inner part of the thin disk disk, their second component to the inner rim of the thick disk and the base of the wind. A part of their third component potentially corresponds to emission of the wind cone at higher altitudes. Since our model is symmetric, we can only speculate that the bulk of the emission of the third component of the López-Gonzaga et al. (2014) model is caused

by an asymmetric illumination of the hollow wind cone as modeled for Circinus by Stalevski et al. (2017).

We conclude that the symmetric RT model reproduces the available interferometric observations in an acceptable way. The comparison with the model of López-Gonzaga et al. (2014) shows why our RT model is quite successful: the two almost parallel components with comparable sizes, the inner component being brighter are well reproduced by our models. The inner component being closer to the central engine is naturally warmer than the outer component, as it is observed in NGC 1068 by López-Gonzaga et al. (2014).

5.2.3. Helical wind components

Motivated by the fact that the large-scale components of the $10\ \mu\text{m}$ interferometric observations are not orthogonal to the smaller-scale (disk) components in the Circinus galaxy (Tristram et al. 2014) and NGC 1068 (López-Gonzaga et al. 2014), we set up an additional helical distribution of the wind. The basic picture is that disk clumps are elevated as entities by the wind and transported upward. During the clump ejection, the clump is rotating and sheared. This naturally leads to a helical structure. In fact, a main characteristic of magnetocentrifugal winds is high rotation velocities. The wind corotates with the disk until the Alfvén radius. Our prescription for the helical outflow has three open parameters: (i) the thickness, (ii) the winding, and (iii) the azimuthal angle of the footpoint of the spiral. We varied all three parameters to investigate their influence on the $10\ \mu\text{m}$ maps. We made simplified radiative transfer models for these helical structures and added them to the full RT models.

Adding a helical wind component to break axis-symmetry decreases χ^2 for both galaxies. The addition of a corotating helical wind to the RT model of Circinus leads to a decreased χ^2_{rel} of 2.2 (Fig. 22). This decrease is small, but significant. Since χ^2 depends on the exact wind geometry which is highly uncertain,

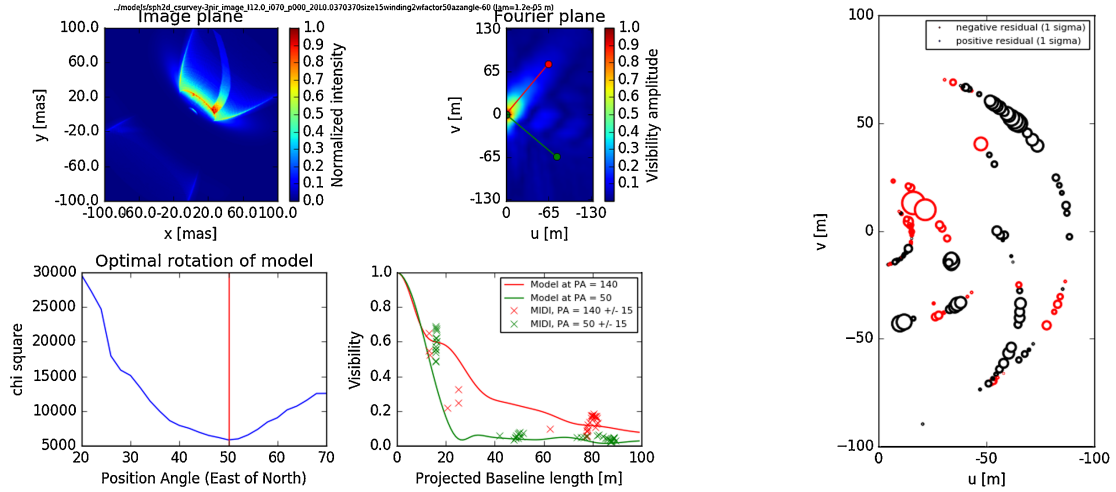


Fig. 22. Same as Fig. 20 for the Circinus radiative transfer model with an additional corotating helical wind component.

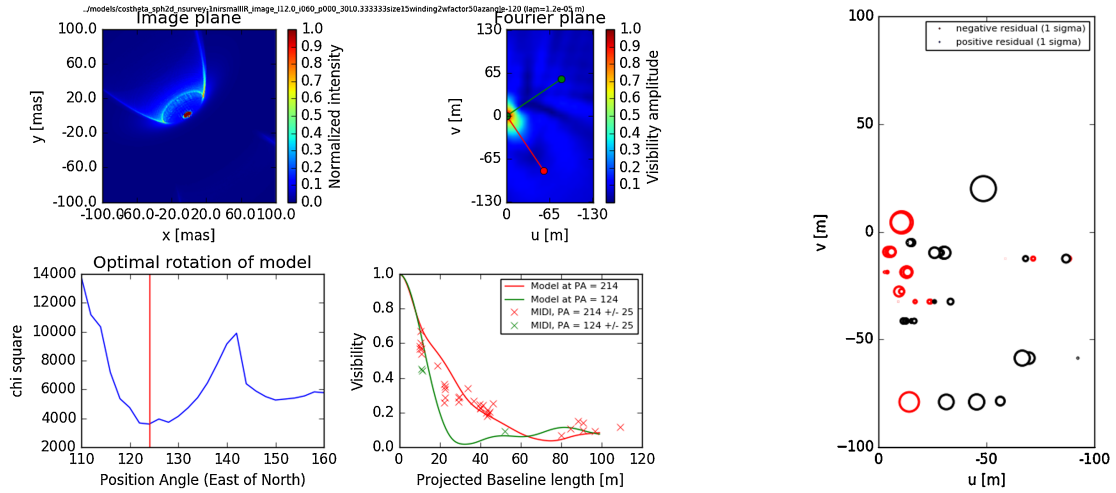


Fig. 23. Same as Fig. 20 for the NGC 1068 radiative transfer model with an additional corotating helical wind component.

one should not overinterpret the models with a helical wind component. As shown by [Tristram et al. \(2014\)](#), such an asymmetric wind component is needed for Circinus. Alternatively, a tilted $\cos(\theta)$ illumination might also lead to an asymmetric MIR emission distribution.

We show the minimum χ^2 RT model for NGC 1068 with an additional corotating wind component in Fig. 23. The addition of a corotating helical wind to the RT model results in a mostly decreased χ^2_{rel} of 2.7. The comparison of the residuals of the symmetric to the helical wind models shows that mainly the most northern visibility decreased significantly.

We conclude that the addition of a helical wind improves the resemblance of the model with respect to the interferometric observations by a small but significant amount in Circinus. For the NGC 1068, the addition of a helical wind does not lead to a significantly better resemblance.

6. Optical polarization

Since the unified model of AGN is based on the observation of optical polarization in nearby Seyfert galaxies ([Antonucci & Miller 1985](#); [Antonucci 1993](#)), we decided to run polarized radiative transfer simulations to investigate whether our models of the Circinus galaxy and NGC 1068 are consistent with archival

polarization data. We confined ourselves to the near-infrared, optical and ultraviolet bands as: 1) the code used to achieve our simulations only works from the X-ray band to the near-infrared (upper limit: $\sim 1 \mu\text{m}$), and 2) most of the past spectropolarimetric measurements were taken between the U and J bands. We used the Monte Carlo radiative transfer code STOKES ([Goosmann & Gaskell 2007](#); [Marin et al. 2012, 2015](#)) and built our 3D models of the Circinus galaxy and NGC 1068 according to Sect. 3.1. In STOKES, the 3D RT model is made of a finite number of discrete geometrical wedges of constant density with sharp edges. Therefore, the vertical density distribution of the thick gas disk is assumed to be constant due to numerical limitations. To mimic a Gaussian vertical density distribution, we decided to increase the thick disk opening angle within the model uncertainties by 30% for Circinus and NGC 1068. This indeed lead to a better agreement with observations. We accounted for the screen of cold dust with $\tau_V = 20$ presented in Sect. 4.2 that is used to reproduce the silicate feature for both AGN. To do so, we included in the 3D model a physical slab of dust which was placed beyond the border of the thick disk, at a distance of 10 pc from the central black hole for Circinus and NGC 1068. Since the screen is optically thick, a larger distance to the central black hole does not influence our results. The projected screen size was 5 pc for NGC 1068 and 2 pc for Circinus. Due to the large optical

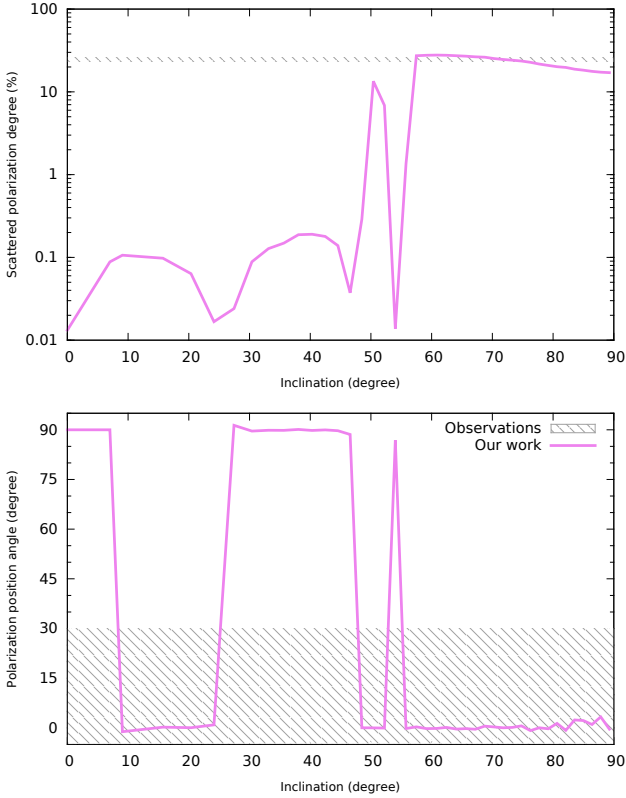


Fig. 24. Wavelength-integrated near-infrared and optical polarization of the Circinus 3D model as a function of inclination. The observed properties are indicated as hatched regions. *Upper panel:* degree of linear polarization as a function of the inclination angle of the gas disk. *Lower panel:* polarization position angle. The polarization results from electron and Mie scattering in the Circinus 3D model.

thickness of the slab, photons are mainly absorbed. The polarization of the few photons that travel through the entire dust screen is not expected to be strongly altered since forward scattering has a minimum impact on the polarization of optical light. For the electron density distribution we assumed that the electrons are co-spatial with the dust grains, with an optical depth of $\tau_V < 1$. We verified that the electron densities are in agreement with observations, that is, the polar electron density lies between 10^3 and 10^6 cm^{-3} , and the equatorial electron density is at least 10^7 cm^{-3} (Blandford et al. 1990). The spectral band of investigation was set from 1125 to 9775 Å, and we looked at the resulting polarization for all inclinations.

6.1. Circinus

Our wavelength-integrated results for the Circinus 3D model are shown in Fig. 24. The magenta lines represent the polarization (top: polarization degree; bottom: polarization position angle) as a function of inclination angle and the shaded areas correspond to the observed polarization regardless of inclination. The degree of linear polarization is rather low at type-1 inclinations due to the dominant amount of unpolarized radiation coming from the continuum source and seen in transmission through the polar region. The net degree of polarization is thus less than 0.2% and shows a polarization position angle mainly equal to 90°, as expected from atlases of type-1 AGN (e.g., Smith et al. 2002). However, the polarization angle rotates from 90° to 0° when the observer’s line-of-sight matches the wind half-opening

angle ($i \sim 15^\circ$). Multiple scattering within the medium induces a variation in polarization angle as photon reprocessing happens in the polar region, decreasing the net polarization in this range of inclinations. Once the line-of-sight of the observer is below the wind half-opening angle ($i > 20^\circ$), the degree of polarization decreases with increasing inclination until a depolarization effect happens at $i \sim 52^\circ$, where the polarization position angle rotates again from 90° to 0°. This transition is due to the predominance of polar scattering as the equatorial thin disk polarization becomes obscured by the optically-thick base of the wind. The fraction of photons that undergoes equatorial scattering in the inner regions becomes weaker and reprocessing in the polar wind dominates the total emission. The rotation of the polarization angle indicates the transition from equatorial-scattering dominated (type-1 AGN) to polar-scattering dominated emission (type-2 AGN). A sudden change of the polarization position angle, associated with a local minima in polarization degree, happens at an inclination of 53°; this feature is only due to the finite edges of the models. With a Gaussian vertical density distribution this feature would disappear. At inclination angles larger than 65°, the observer’s line-of-sight is completely obscured by the equatorial thick disk and electron and Mie scattering in the polar wind dominates. The polarization degree is then plateauing at ~20% until a 90° inclination due to the dust screen that obscures the base of the polar winds. Compared to observations, our model is able to reproduce both, the observed degree and angle of polarization, at inclinations $i \geq 68^\circ$. This is in agreement with the nucleus inclination derived from MIR interferometric observations (Sect. 5.2), and also in agreement with the inclination angle derived by Fischer et al. (2013) for the same object.

We thus fixed the inclination of the observer to 68° and plotted in Fig. 25 the wavelength dependence of the near-infrared and optical polarization properties of the Circinus model. We also report the observations made by Oliva et al. (1998); Alexander et al. (2000), and Ruiz et al. (2000) on the plot. The observed polarization degree has been corrected for host galaxy depolarization and starburst light dilution following the method presented in Marin (2014). Our results are consistent within 1σ with the estimated amount of scattered polarization⁵ from the modeling achieved by Oliva et al. (1998). Our model is in agreement with the observation of the scattered continuum of the Circinus galaxy in the 5000–6500 Å band, where spectropolarimetry is available. The dependence of the polarization degree, decreasing from the optical to the near-IR band, is due to the important contribution of dust obscuration by the screen. It would be necessary to extend the wavelength coverage of the code to investigate whether our results also agree with infrared data, but the tendency of the model curve seems to be in agreement with observations. The polarization position angle is also consistent with observations and we do not expect any rotation of the angle with wavelength upward 1 μm, because Mie and Thomson scattering will remain the main reprocessing processes until 2 μm.

6.2. NGC 1068

The case of NGC 1068 is more complex. The determination of the inclination angle of the thick disk with different methods led to different results: kinematical modeling of the NLR bicone yielded $i = 85\text{--}90^\circ$ (Das et al. 2006; Müller Sánchez et al. 2009); MIR interferometry (López-Gonzaga et al. 2014) yielded an axis

⁵ About 25% at all optical wavelengths, see Oliva et al. (1998).

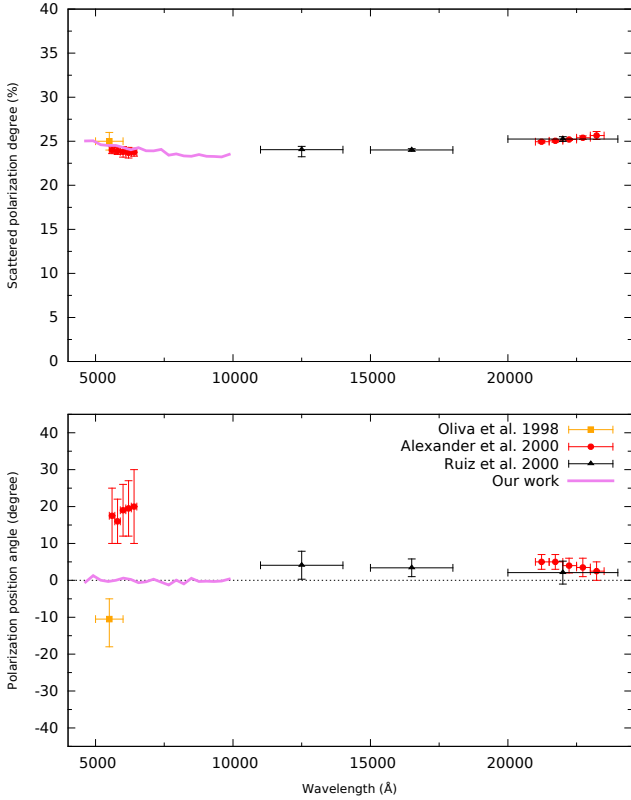


Fig. 25. Wavelength dependence of the optical polarization properties of the Circinus 3D model ($i = 68^\circ$; magenta) compared to observations.

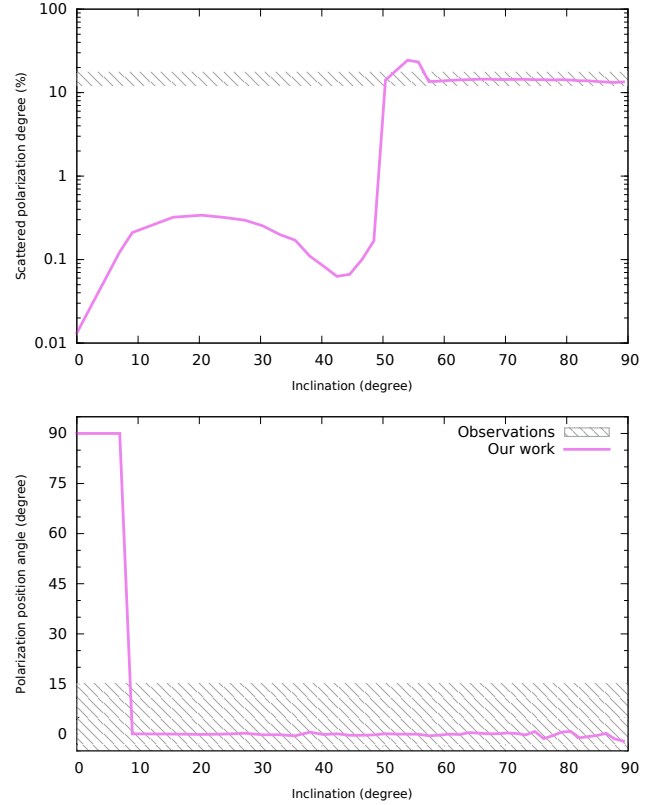


Fig. 26. Same as Fig. 24 for the NGC 1068 3D model, with the addition of the ultraviolet polarization.

ratio of the compact component 1 of 7 mas/20 mas = 0.35, which translates to an inclination angle of 70° if one assumes that the emission of the MIR interferometry component 1 comes from a thin disk. If the emission of the MIR interferometry component 1 stems from the inner rim of the thick gas disk, the inclination angle can be lower, such as $i \sim 60^\circ$. We prefer an inclination angle of the thick gas disk of $i \sim 60^\circ$, because this naturally explains the first two components found by López-Gonzaga et al. (2014): component 1: inner thin disk with puff-up; component 2: inner rim of the thick disk.

The results for NGC 1068 are presented in Fig. 26. Similarly to our previous polarization modeling, the magenta line is the inclination-dependent polarization and the shaded area corresponds to the observed polarization. Regarding the type-1 polarization signatures, we find a similar behavior of both the degree and angle of polarization with inclination with respect to the Circinus galaxy 3D model; the differences are due to the moderately different geometry and density profile of the polar wind. The polarization position angle is equal to 90° at polar inclinations, then rotates when the observer's viewing angle coincides with the half-opening angle of the wind. At this particular inclination range, the degree of polarization rises up to 0.3%, which is usual for type-1 AGNs. Once the viewing angle is below the wind's lower boundary, obscuration by the extended dust screen covers the signature of the equatorial thin disk and the polarization position angle remains 0° . The transition between type-1 and type-2 signature occurs between $i \sim 45^\circ$, a lower angle than that found for Circinus. It is only at an inclination of $\sim 50^\circ$ that the model reproduces both, the observed polarization degree and position angle. This value is in agreement with our interferometric results ($i = 60^\circ$; Sect. 5.2), yet significantly different from the inclination derived from the methods that consist of mapping

and modeling the radial velocities of the [OIII] emission region in AGN (Das et al. 2006; Müller-Sánchez et al. 2011) and of IR SED fitting (Hönig et al. 2008).

To be consistent with our results from the MIR interferometric observations, we fixed the inclination of the observer to 60° and plotted in Fig. 27 the wavelength dependence of the ultraviolet, optical and near-infrared polarization properties of the NGC 1068 model. Archival Lick 3 m and HST polarimetric observations of NGC 1068, corrected for starburst light, are reported on the plot (Miller & Antonucci 1983; Antonucci & Miller 1985; Code et al. 1993). For an inclination angle of $i = 60^\circ$ the model is within the expected polarization levels and its polarization position angle is similar to what was reported by observations for NGC 1068. The wavelength-dependence of the scattered polarization indicates a dust origin and the gradient of the degree of polarization with respect to wavelength is due to the dust mixture itself. We used a standard Milky Way composition for the dust grains (Mathis et al. 1977) but the real mineralogy and size distribution of extragalactic dust grains is poorly constrained. Assuming a different size distribution of silicates and graphite would lead to variations of the polarization degree in the UV-optical band. A more rigorous exploration of the polarized signal of AGN is thus mandatory to better constrain our dust prescriptions.

Tension still persists between the NLR bicone axis inclination, which translates into a disk inclination of $\sim 80^\circ$, and our inferred inclination of the inner thick gas disk of $\sim 60^\circ$. In the following we show that both inclination angles have not to be identical. The NLR bicone has a height of ~ 100 pc with an outflow velocity of $\sim 1000 \text{ km s}^{-1}$ (Müller-Sánchez et al. 2011). This gives a timescale of 10^5 yr. The dynamical timescale of the inner edge of the thick gas disk which determines the inclination angle

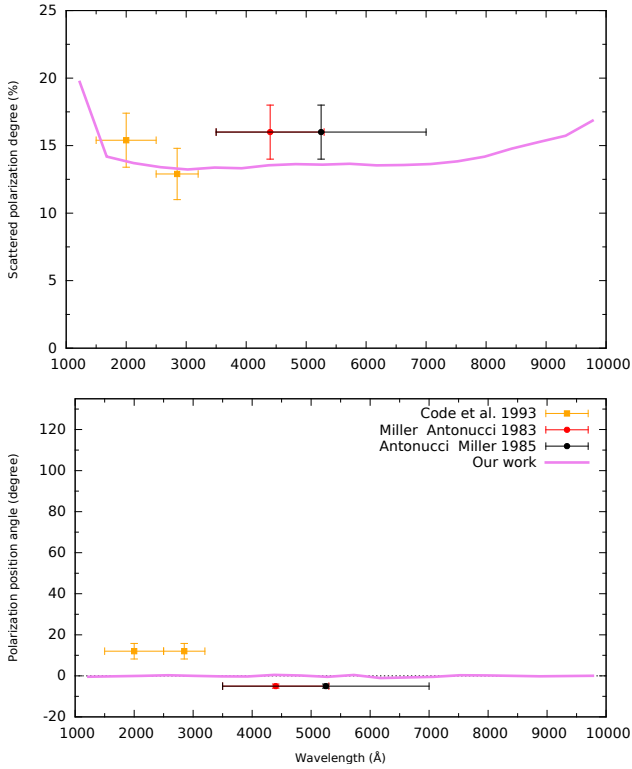


Fig. 27. Same as Fig. 25 for the NGC 1068 3D model ($i = 60^\circ$), including the ultraviolet band.

of the wind is $\Omega = 1.5 \text{ pc}/(170 \text{ km s}^{-1}) \sim 10^4 \text{ yr}$ (see Table 1). Hence, given the different timescales, the inclination angle of the bicone has not necessarily to be that of the present thick gas disk in such a lively environment.

We conclude that our models of the Circinus galaxy and NGC 1068 are able to reproduce both, the polarization dichotomy between type-1 and type-2 AGN and the observed polarization levels. The model is slightly degenerated as variations in the line-of-sight or in optical depth of the wind will change the final degree of polarization, but the values used here are in very good agreement with observational results from the literature.

7. Conclusions

Recent IR high-resolution imaging and interferometry showed that the dust distribution is frequently elongated along the polar direction of an AGN (Hönig et al. 2012, 2013; Tristram et al. 2014; López-Gonzaga et al. 2014, 2016; Asmus et al. 2016). In addition, recent interferometric CO(6–5) observations revealed a bipolar outflow in a direction nearly perpendicular to the nuclear disk (Gallimore et al. 2016). It thus appears that a nuclear molecular and dusty outflow or wind plays an important role for the overall gas flows in the vicinity ($r < 10 \text{ pc}$) of the central black hole.

We developed a model scenario for the inner $\sim 30 \text{ pc}$ of an AGN which takes into account the recent observational progress (Fig. 1). Our view of an AGN is from outside in. The structure of the gas within this region is entirely determined by the gas inflow from larger scales. We assumed a rotating gas disk between about one and ten parsec. External gas accretion adds mass and injects energy via gas compression into this gas disk. Since all observed gas disks are thick (Davies et al. 2007; Vollmer et al. 2008), we assumed that the energy injection via external accretion

drives turbulence. If the energy injection or gas compression timescale is shorter than the turbulent dissipation timescale, the gas compression is adiabatic, gas clouds are overpressured, star formation is suppressed, and the disk becomes thick (Vollmer & Davies 2013). The behavior of the gas within $\sim 10 \text{ pc}$ is set by the gas mass and the mass accretion rate of the massive thick disk which is located at radii beyond $\sim 1 \text{ pc}$. Our thick gas disks are assumed to be strongly magnetized via equipartition between the turbulent gas pressure and the energy density of the magnetic field. In our massive and strongly magnetized thick disks the outflow rate due to magnetocentrifugal forces dominates that due to radiation pressure (Sect. 2.1). The strong magnetic field associated with this thick gas disk plays a major role in driving a magnetocentrifugal wind (Blandford & Payne 1982) at a distance of $\sim 1 \text{ pc}$ from the central black hole (Sect. 2.6). Once the wind is launched, it is responsible for the transport of angular momentum and the gas disk can become thin. A magnetocentrifugal wind is also expected above the thin disk (Sect. 2.3). Radiation pressure might play a significant role for the launching of the wind by bending the field lines to an angle $\gtrsim 30^\circ$ from the polar axis within the inner edge of the thick disk, but is not included in our model.

We identify the thin disk at radii $< 1 \text{ pc}$ with the observed maser disks in AGN (e.g., Greenhill et al. 2003). The inner edge of the dusty maser disk is determined by the dust sublimation radius (Barvainis 1987). The dust-free gas disk continues right to the central black hole. The mass accretion rate decreases when the gas approaches the central black hole: it is about $1 M_\odot \text{ yr}^{-1}$ for the thick gas disk, $< 0.5 M_\odot \text{ yr}^{-1}$ for the thin disk, and $\sim 0.1 M_\odot \text{ yr}^{-1}$ for the accretion disk very close to the central black hole. This implies the existence of a strong BLR wind. The luminosity of the AGN is then set by the mass accretion rate of the central accretion disk \dot{M}_{final} via $L_{\text{bol}} = 0.1 \dot{M}_{\text{final}} c^2 = 6 \times 10^{44} (\dot{M}_{\text{final}} / (0.1 M_\odot \text{ yr}^{-1})) \text{ erg s}^{-1}$.

We extended the description of a turbulent thick gas disk developed by Vollmer & Davies (2013) by adding a magnetocentrifugal wind which starts at a given radius $r_{\text{wind}} \simeq 0.5\text{--}2 \text{ pc}$ (Sect. 2). The structure and outflow rate of this wind is determined by the properties of the thick gas disk assuming energy equipartition between the turbulent and magnetic energy densities. We assumed that the outflow rate of the wind above the thin disk is comparable to that of the wind starting from the thick disk. Since angular momentum of the thin disk is removed by the magnetocentrifugal wind, the mass accretion rate of the thin disk is directly linked to the wind outflow rate (Eq. (35)). We also assumed conservation of mass flux (Eq. (36)). Viable wind models are calculated by varying turbulent velocity dispersion of the thick disk and the wind radii r_{wind} (Sect. 2.8).

In a second step, we built 3D density cubes based on the analytical model of a thick disk, magnetocentrifugal wind, and thin disk. We added a puff-up to the thin disk, close to the dust sublimation radius, as observed in young stellar objects. All density distributions are smooth. The model parameters were adjusted to reproduce available observations of the Circinus galaxy and NGC 1068. These two AGN bracket the range of local AGNs in terms of black hole mass, rotation velocity, and bolometric luminosity.

We assumed $1/z$ and $1/z^2$ density profiles for the wind. In addition to the axis-symmetric model, we added a helical wind component to the model cubes (Sect. 5.2.3). These structures were illuminated by a central source (isotropic or $\cos(\theta)$ illumination) of different bolometric luminosities and 2D radiative transfer calculations were performed. We calculated the MIR and

NIR luminosities, the central extinctions, SEDs, and point source fractions of these model series for varying inclination angles (Sect. 4). In a third step, we calculated MIR visibility amplitudes and compared them to available observations (Sect. 5). All models assume smooth gas and dust distributions. We are mainly interested in the thick gas disk and the transition between the thick and thin gas disks involving a magnetocentrifugal wind. The detailed geometry of the inner thin gas disk is not subject of this article.

We conclude that within our model assumptions

1. magnetocentrifugal winds starting from a thin and thick gas disk are viable in active galaxy centers (Sect. 2.8); radiation pressure is expected to only play an important role above the inner thin disk making the wind more equatorial there (Sect. 2.1),
2. thick gas disks with high Toomre parameters ($Q \gtrsim 40$) and low mass accretion rates ($\dot{M} \lesssim 0.1 M_{\odot} \text{ yr}^{-1}$) cannot have a magnetocentrifugal wind (e.g., the circumnuclear disk in the galactic center; Sect. 2.8),
3. the outflow scenario can account for the elongated dust structures, outer edges of the thin maser disks, and molecular outflows observed in local AGN; it helps to decrease the mass accretion rate from the outer thick gas disk to the innermost accretion disk around the central black hole,
4. the model terminal velocities are consistent with observations (Sect. 2.9),
5. a key ingredient of the model is the transition region between the thick and the thin disk which creates a directly illuminated inner wall of the thick gas and dust disk (Sect. 3.1; Fig. 5),
6. based on the comparison between the MIR and NIR luminosities to observations of local AGN (Burtscher et al. 2015), a $\cos(\theta)$ illumination is preferred over an isotropic illumination,
7. our model $L_{\text{MIR}}/L_{\text{bol}}$ ratios are at least a factor of two higher than the ratio derived from observations; it is expected that a slightly different geometry of the inner wall of the thick gas disk and a clumpy wind decrease $L_{\text{MIR}}/L_{\text{bol}}$,
8. about half of the MIR luminosity is emitted by the wind (Sect. 4.3); the inclination angle has thus a minor impact on the MIR luminosity; this makes the MIR – intrinsic X-ray correlation possible,
9. the wind or outflow can in principle account for a significant fraction of the central optical extinction (Sect. 4.1),
10. for a realistic comparison with observations of Circinus and NGC 1068, a puff-up of the inner edge of the thin disk near the dust sublimation radius and a local foreground screen of $A_V \sim 20$ are needed;
11. the IR SEDs of Circinus and NGC 1068 are reproduced by our models in a satisfactory way (Sect. 4.2); the exact form of the SED depends on the structure of the inner thin disk (puff-up, warp, tilt),
12. the point source fraction of type 2 objects mainly depends on inclination, that of type 1 objects on bolometric luminosity (Sect. 4.4); a point source fraction >0.7 in type 1 AGNs indicates the absence of a wind and/or outflow; for point source fraction of about one even the thick disk is absent,
13. our Circinus and NGC 1068 models reproduce available MIR interferometric observations in an acceptable way (Sect. 5); the basic geometry of our model is thus consistent with observations; an asymmetric wind component or a tilted $\cos(\theta)$ illumination as suggested by Stalevski et al. (2017) is needed for Circinus to better reproduce observations,
14. the second, disk-like component identified from MIR interferometric observations by Tristram et al. (2014) might correspond to the inner wall of the thick gas disk; the first, small-scale component of López-Gonzaga et al. (2014) to the thin maser disk with an inner puff-up,
15. we derive inclination angles of $i = 70^\circ$ and $i = 60^\circ$ for Circinus and NGC 1068, respectively; the inner thin maser disk are probably tilted or warped with respect to the thick gas disks,
16. our Circinus and NGC 1068 models are consistent with available optical polarization data.

Our thick disk, wind, thin disk model is thus a promising scenario for local Seyfert galaxies. The model is completed by an inner puff-up of the thin disk, as observed in YSOs, and a local foreground screen with $\tau_V \sim 20$. In a subsequent work we will have a look at the differential phases derived from the MIR interferometric observations. These differential phases represent important additional constraints on the model. Moreover, we plan to progress from our smooth to a clumpy model to investigate the influence of clumpiness on our results.

Acknowledgements. We would like to thank the anonymous referee for helping to significantly improve this article. L.B. was supported by the DFG grant within the SPP 1573 “Physics of the interstellar medium”.

References

- Alexander, D. M., Heisler, C. A., Young, S., et al. 2000, *MNRAS*, **313**, 815
- Antonucci, R. 1993, *ARA&A*, **31**, 473
- Antonucci, R. R. J., & Miller, J. S. 1985, *ApJ*, **297**, 621
- Asmus, D., Gandhi, P., Hönic, S. F., Smette, A., & Duschl, W. J. 2015, *MNRAS*, **454**, 766
- Asmus, D., Hönic, S. F., & Gandhi, P. 2016, *ApJ*, **822**, 109
- Barvainis, R. 1987, *ApJ*, **320**, 537
- Beck, R. 2015, *A&ARv*, **24**, 4
- Bjorkman, J. E., & Wood, K. 2001, *ApJ*, **554**, 615
- Blandford, R. D., & Payne, D. G. 1982, *MNRAS*, **199**, 883
- Blandford, R. D., Netzer, H., Woltjer, L., Courvoisier, T. J.-L., & Mayor, M. 1990, *Active Galactic Nuclei*, **97**
- Burtscher, L., Meisenheimer, K., Tristram, K. R. W., et al. 2013, *A&A*, **558**, A149
- Burtscher, L., Orban de Xivry, G., Davies, R. I., et al. 2015, *A&A*, **578**, A47
- Burtscher, L., Hönic, S., Jaffe, W., et al. 2016, *Proc. SPIE*, **9907**, 99070R
- Chan, C.-H., & Krolik, J. H. 2016, *ApJ*, **825**, 67
- Chan, C.-H., & Krolik, J. H. 2017, *ApJ*, **843**, 58
- Code, A. D., Meade, M. R., Anderson, C. M., et al. 1993, *ApJ*, **403**, L63
- Das, V., Crenshaw, D. M., Kraemer, S. B., & Deo, R. P. 2006, *AJ*, **132**, 620
- Davies, R. I., Müller Sánchez, F., Genzel, R., et al. 2007, *ApJ*, **671**, 1388
- Dobbs, C. L., & Pringle, J. E. 2013, *MNRAS*, **1187**
- Dorodnitsyn, A., Kallman, T., & Proga, D. 2016, *ApJ*, **819**, 115
- Draine, B. T. 2003, *ApJ*, **598**, 1026
- Draine, B. T., & Lee, H. M. 1984, *ApJ*, **285**, 89
- Draine, B. T., Roberge, W. G., & Dalgarno, A. 1983, *ApJ*, **264**, 485
- Draine, B. T., Dale, D. A., Bendo, G., et al. 2007, *ApJ*, **663**, 866
- Dullemond, C. P. 2012, *Astrophysics Source Code Library*, [record ascl:1202.015]
- Dullemond, C. P., Dominik, C., & Natta, A. 2001, *ApJ*, **560**, 957
- Elitzur, M. 2006, *New Ast.*, **50**, 728
- Elitzur, M. 2012, *ApJ*, **747**, L33
- Elvis, M. 2000, *ApJ*, **545**, 63
- Everett, J. E. 2005, *ApJ*, **631**, 689
- Feruglio, C., Maiolino, R., Piconcelli, E., et al. 2010, *A&A*, **518**, L155
- Fischer, T. C., Crenshaw, D. M., Kraemer, S. B., & Schmitt, H. R. 2013, *ApJS*, **209**, 1
- Fleck, J. A., Jr. & Canfield, E. H. 1984, *J. Comput. Phys.*, **54**, 508
- Gallimore, J. F., Elitzur, M., Maiolino, R., et al. 2016, *ApJ*, **829**, L7
- Gandhi, P., Horst, H., Smette, A., et al. 2009, *A&A*, **502**, 457
- García-Burillo, S., Combes, F., Ramos Almeida, C., et al. 2016, *ApJ*, **823**, L12
- Gaskell, C. M. 2009, *New Ast.*, **53**, 140
- Goosmann, R. W., & Gaskell, C. M. 2007, *A&A*, **465**, 129
- Greenhill, L. J. 1998, *IAU Colloq. 164: Radio Emission from Galactic and Extragalactic Compact Sources*, **144**, 221

- Greenhill, L. J., & Gwinn, C. R. 1997, *Ap&SS*, **248**, 261
- Greenhill, L. J., Henkel, C., Becker, R., Wilson, T. L., & Wouterloot, J. G. A. 1995, *A&A*, **304**, 21
- Greenhill, L. J., Gwinn, C. R., Antonucci, R., & Barvainis, R. 1996, *ApJ*, **472**, L21
- Greenhill, L. J., Booth, R. S., Ellingsen, S. P., et al. 2003, *ApJ*, **590**, 162
- Güsten R., Genzel R., Wright M. C. H. et al., 1987, *ApJ*, **318**, 124
- Hicks, E. K. S., Davies, R. I., Malkan, M. A., et al. 2009, *ApJ*, **696**, 448
- Hönig, S. F., & Kishimoto, M. 2010, *A&A*, **523**, A27
- Hönig, S. F., & Kishimoto, M. 2017, *ApJ*, **838**, L20
- Hönig, S. F., Prieto, M. A., & Beckert, T. 2008, *A&A*, **485**, 33
- Hönig, S. F., Leipski, C., Antonucci, R., & Haas, M. 2011, *ApJ*, **736**, 26
- Hönig, S. F., Kishimoto, M., Antonucci, R., et al. 2012, *ApJ*, **755**, 149
- Hönig, S. F., Kishimoto, M., Tristram, K. R. W., et al. 2013, *ApJ*, **771**, 87
- Jud, H., Schartmann, M., Mould, J., Bartscher, L., & Tristram, K. R. W. 2017, *MNRAS*, **465**, 248
- Keating, S. K., Everett, J. E., Gallagher, S. C., & Deo, R. P. 2012, *ApJ*, **749**, 32
- Kishimoto, M., Hönig, S. F., Beckert, T., & Weigelt, G. 2007, *A&A*, **476**, 713
- Kishimoto, M., Hönig, S. F., Antonucci, R., et al. 2011, *A&A*, **536**, A78
- Konigl, A., & Pudritz, R. E. 2000, *Protostars and Planets IV*, 759
- Krolik J. H., & Begelman M. C., 1988, *ApJ*, **329**, 702
- Lamy, H., & Hutsemékers, D. 2004, *A&A*, **427**, 107
- Laor, A., & Draine, B. T. 1993, *ApJ*, **402**, 441
- Lin, M.-Y., Davies, R. I., Bartscher, L., et al. 2016, *MNRAS*, **458**, 1375
- Liu, T., Wang, J.-X., Yang, H., Zhu, F.-F., & Zhou, Y.-Y. 2014, *ApJ*, **783**, 106
- Lodato, G., & Bertin, G. 2003, *A&A*, **398**, 517
- López-Gonzaga, N., Jaffe, W., Bartscher, L., Tristram, K. R. W., & Meisenheimer, K. 2014, *A&A*, **565**, A71
- López-Gonzaga, N., Bartscher, L., Tristram, K. R. W., Meisenheimer, K., & Schartmann, M. 2016, *A&A*, **591**, A47
- Lopez-Rodriguez, E., Packham, C., Jones, T. J., et al. 2015, *MNRAS*, **452**, 1902
- Lucy, L. B. 1999, *A&A*, **344**, 282
- Maiolino, R., & Rieke, G. H. 1995, *ApJ*, **454**, 95
- Marconi, A., Risaliti, G., Gilli, R., et al. 2004, *MNRAS*, **351**, 169
- Marin, F. 2014, *MNRAS*, **441**, 551
- Marin, F., & Goosmann, R. W. 2013, *MNRAS*, **436**, 2522
- Marin, F., Goosmann, R. W., Gaskell, C. M., Porquet, D., & Dovčiak M. 2012, *A&A*, **548**, A121
- Marin, F., Goosmann, R. W., & Gaskell, C. M. 2015, *A&A*, **577**, A66
- Mateos, S., Carrera, F. J., Barcons, X., et al. 2017, *ApJ*, **841**, L18
- Mathis, J. S., Rimpl, W., & Nordsieck, K. H. 1977, *ApJ*, **217**, 425
- Matt, G. 2000, *A&A*, **355**, L31
- McKee, C. F., Li, P. S., & Klein, R. I. 2010, *ApJ*, **720**, 1612
- Meijerink, R., & Spaans, M. 2005, *A&A*, **436**, 397
- Michel, F. C. 1969, *ApJ*, **158**, 727
- Miller, J. S., & Antonucci, R. R. J. 1983, *ApJ*, **271**, L7
- Min, M., Dullemond, C. P., Dominik, C., de Koter, A., & Hovenier, J. W. 2009, *A&A*, **497**, 155
- Monnier, J. D., Berger, J.-P., Millan-Gabet, R., et al. 2006, *ApJ*, **647**, 444
- Moorwood, A. F. M., Lutz, D., Oliva, E., et al. 1996, *A&A*, **315**, L109
- Müller Sánchez, F., Davies, R. I., Genzel, R., et al. 2009, *ApJ*, **691**, 749
- Müller-Sánchez, F., Prieto, M. A., Hicks, E. K. S., et al. 2011, *ApJ*, **739**, 69
- Natta, A., Prusti, T., Neri, R., et al. 2001, *A&A*, **371**, 186
- Netzer, H. 1987, *MNRAS*, **225**, 55
- Netzer, H. 2015, *ARA&A*, **53**, 365
- Netzer, H., Lani, C., Nordon, R., et al. 2016, *ApJ*, **819**, 123
- Oliva, E., Marconi, A., Cimatti, A., & di Serego Alighieri, S. 1998, *A&A*, **329**, L21
- Pier, E. A., Antonucci, R., Hurt, T., Kriss, G., & Krolik, J. 1994, *ApJ*, **428**, 124
- Prieto, M. A., Reunanen, J., Tristram, K. R. W., et al. 2010, *MNRAS*, **402**, 724
- Prieto, M. A., Mezcuca, M., Fernández-Ontiveros, J. A., & Schartmann, M. 2014, *MNRAS*, **442**, 2145
- Pringle J. E., 1981, *ARA&A*, **19**, 137
- Pudritz, R. E., & Norman, C. A. 1983, *ApJ*, **274**, 677
- Pudritz, R. E., & Norman, C. A. 1986, *ApJ*, **301**, 571
- Ramos Almeida, C., Martínez González, M. J., Asensio Ramos, A., et al. 2016, *MNRAS*, **461**, 1387
- Robitaille, T. P. 2010, *A&A*, **520**, A70
- Roth, N., Kasen, D., Hopkins, P. F., & Quataert, E. 2012, *ApJ*, **759**, 36
- Ruiz, M., Alexander, D. M., Young, S., et al. 2000, *MNRAS*, **316**, 49
- Sani, E., Davies, R. I., Sternberg, A., et al. 2012, *MNRAS*, **424**, 1963
- Sazonov, S., Churazov, E., & Krivonos, R. 2015, *MNRAS*, **454**, 1202
- Schartmann, M., Meisenheimer, K., Camenzind, M., Wolf, S., & Henning, T. 2005, *A&A*, **437**, 861
- Schartmann, M., Wada, K., Prieto, M. A., Burkert, A., & Tristram, K. R. W. 2014, *MNRAS*, **445**, 3878
- Schnorr-Müller, A., Davies, R. I., Korista, K. T., et al. 2016, *MNRAS*, **462**, 3570
- Smith, J. E., Young, S., Robinson, A., et al. 2002, *MNRAS*, **335**, 773
- Stalevski, M., Asmus, D., & Tristram, K. R. W. 2017, *MNRAS*, **472**, 3854
- Stern, J., & Laor, A. 2012, *MNRAS*, **426**, 2703
- Suganuma, M., Yoshii, Y., Kobayashi, Y., et al. 2006, *ApJ*, **639**, 46
- Tristram, K. R. W., Bartscher, L., Jaffe, W., et al. 2014, *A&A*, **563**, A82
- Veilleux, S., & Bland-Hawthorn, J. 1997, *ApJ*, **479**, L105
- Vollmer, B., & Beckert T. 2002, *A&A*, **382**, 872
- Vollmer, B., & Davies, R. I. 2013, *A&A*, **556**, A31
- Vollmer, B., & Duschl, W. J. 2001, *A&A*, **367**, 72
- Vollmer, B., Beckert, T., & Duschl, W. J. 2004, *A&A*, **413**, 949
- Vollmer, B., Beckert, T., & Davies, R. I. 2008, *A&A*, **491**, 441
- Wada, K. 2012, *ApJ*, **758**, 66
- Wada, K., Meurer, G., & Norman, C. A. 2002, *ApJ*, **577**, 197
- Wada, K., Papadopoulos, P. P., & Spaans, M. 2009, *ApJ*, **702**, 63
- Wada, K., Schartmann, M., & Meijerink, R. 2016, *ApJ*, **828**, L19
- Wardle, M., & Koenigl, A. 1993, *ApJ*, **410**, 218
- Weingartner, J. C., & Draine, B. T. 2001, *ApJ*, **548**, 296
- Wilson, A. S., Shopbell, P. L., Simpson, C., et al. 2000, *AJ*, **120**, 1325
- Yang, H., Wang, J., & Liu, T. 2015, *ApJ*, **799**, 91

Appendix A: Thick disk model without a wind

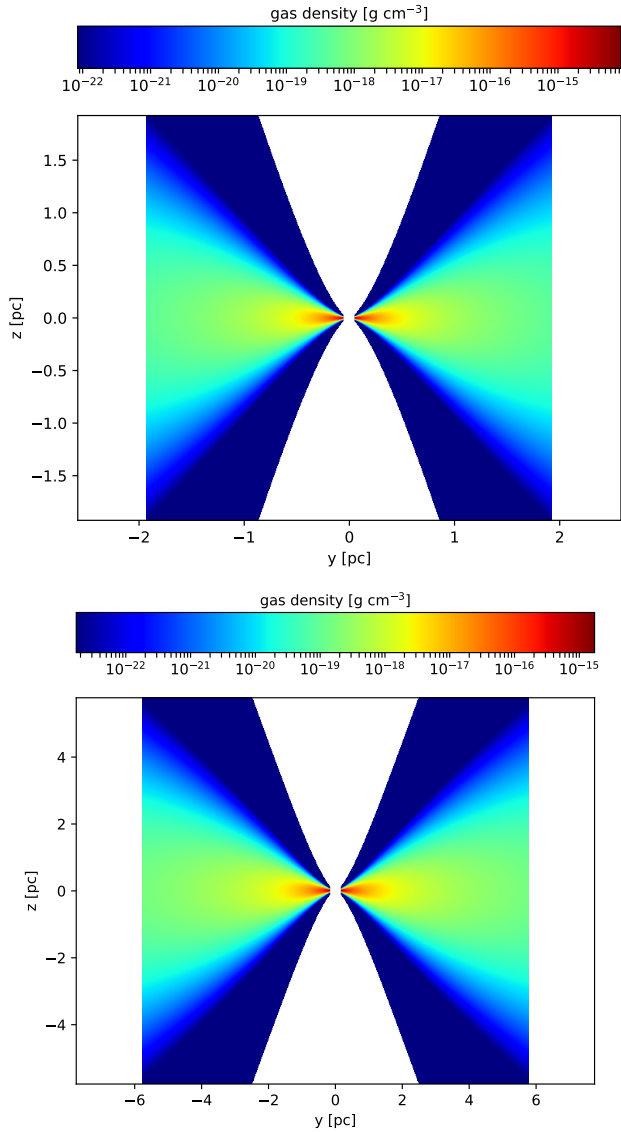


Fig. A.1. Thick disk model without a wind. Density cut through the model cube of the Circinus galaxy (*upper panel*) and NGC 1068 (*lower panel*). The transfer function is logarithmic.

Appendix B: MIR and NIR emission of the $1/z^2$ wind model

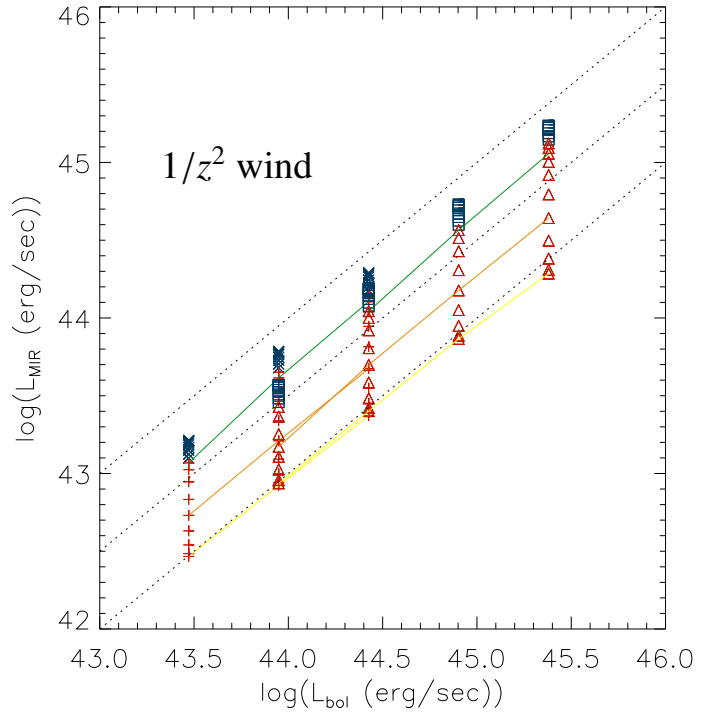


Fig. B.1. Model MIR luminosities as a function of the bolometric luminosity. Blue color represents type 1 objects, red represents type 2. The Circinus model is shown with crosses and pluses; the NGC 1068 model by squares and triangles. The inclination angles of type 2 objects are indicated: $i = 50^\circ$ (green line), $i = 70^\circ$ (orange line), $i = 90^\circ$ (yellow line).

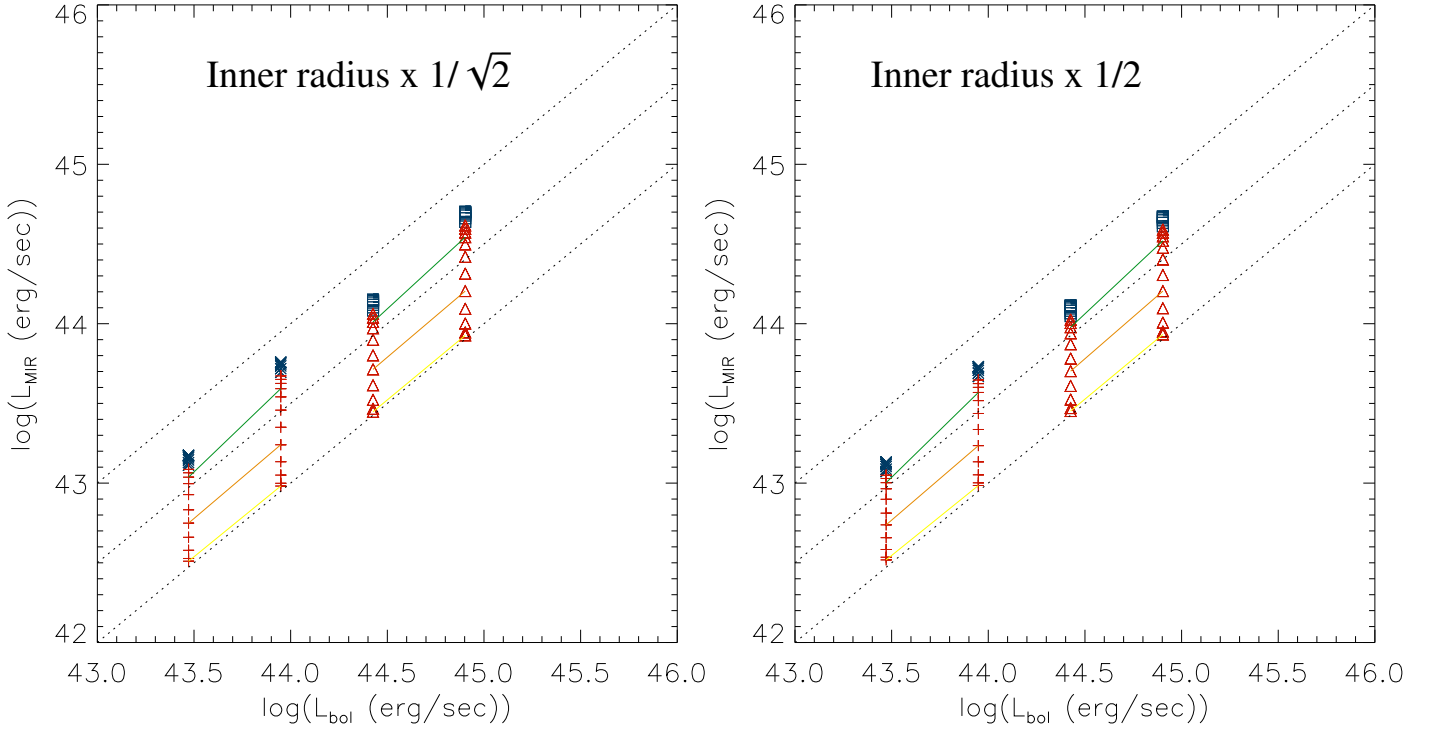


Fig. B.2. Model MIR luminosities as a function of the bolometric luminosity for the $1/z$ winds for a $\sqrt{2}$ (left panel) and 2 (right panel) times smaller inner radius of the thin gas disk (compare to Fig. 9).

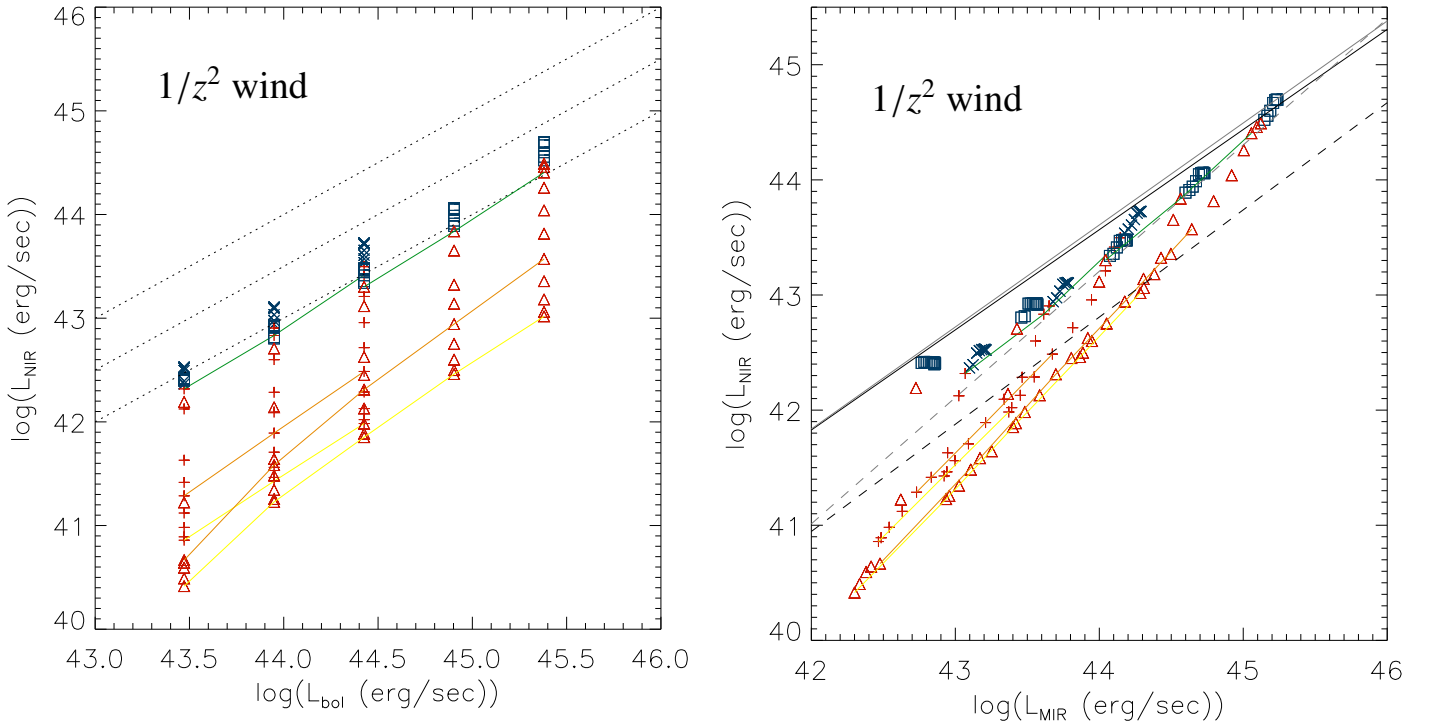


Fig. B.3. Model NIR luminosities as a function of the bolometric luminosity. Blue represents type 1 objects, red represents type 2. The Circinus model is shown by crosses and pluses; the NGC 1068 model by squares and triangles. The inclination angles of type 2 objects are indicated: $i = 50^\circ$ (green line), $i = 70^\circ$ (orange line), $i = 90^\circ$ (yellow line).

Fig. B.4. Model NIR luminosities as a function of the MIR luminosity. Blue represents type 1 objects, red represents type 2. The Circinus model is shown by crosses and pluses; NGC 1068 model by squares and triangles. The inclination angles of type 2 objects are indicated: $i = 50^\circ$ (green line), $i = 70^\circ$ (orange line), $i = 90^\circ$ (yellow line).

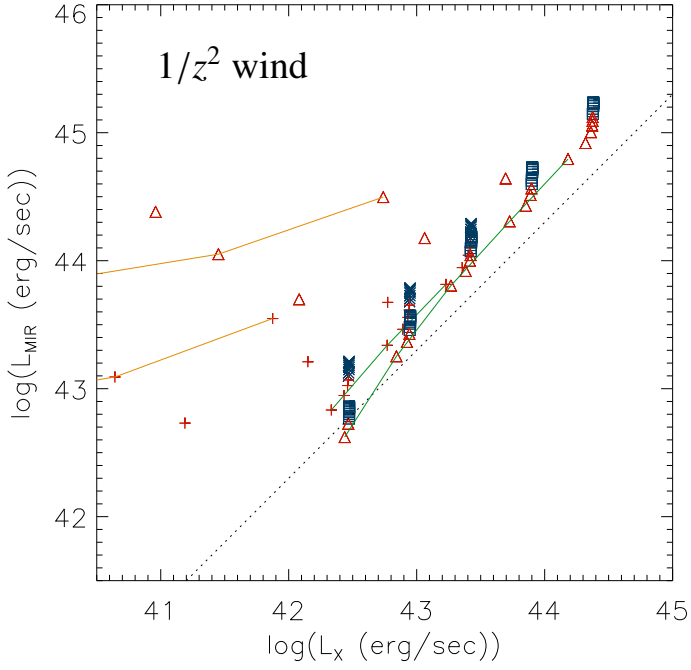


Fig. B.5. Model MIR–X-ray correlation. Blue represents type 1 objects, red represents type 2. The Circinus model is shown by crosses and pluses; NGC 1068 model by squares and triangles. The inclination angles of type 2 objects are indicated: $i = 65^\circ$ (green line), $i = 75^\circ$ (orange line). The dotted line corresponds to the correlation found by [Asmus et al. \(2015\)](#): $\log(L_{\text{MIR}}) = \log(L_X) + 0.33$.

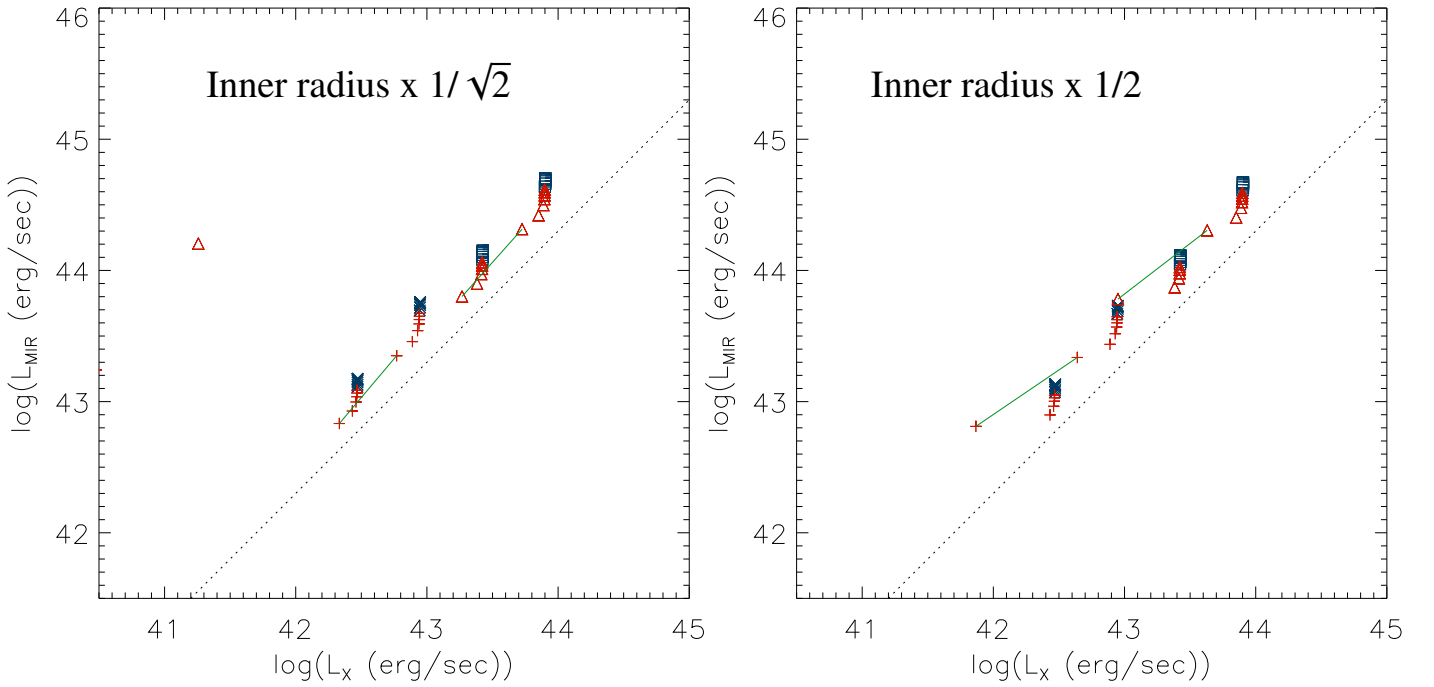


Fig. B.6. Model MIR–X-ray correlation for the $1/z$ winds for a $\sqrt{2}$ (left panel) and 2 (right panel) times smaller inner radius of the thin gas disk (compare to Fig. 14).

Appendix C: Point source fraction

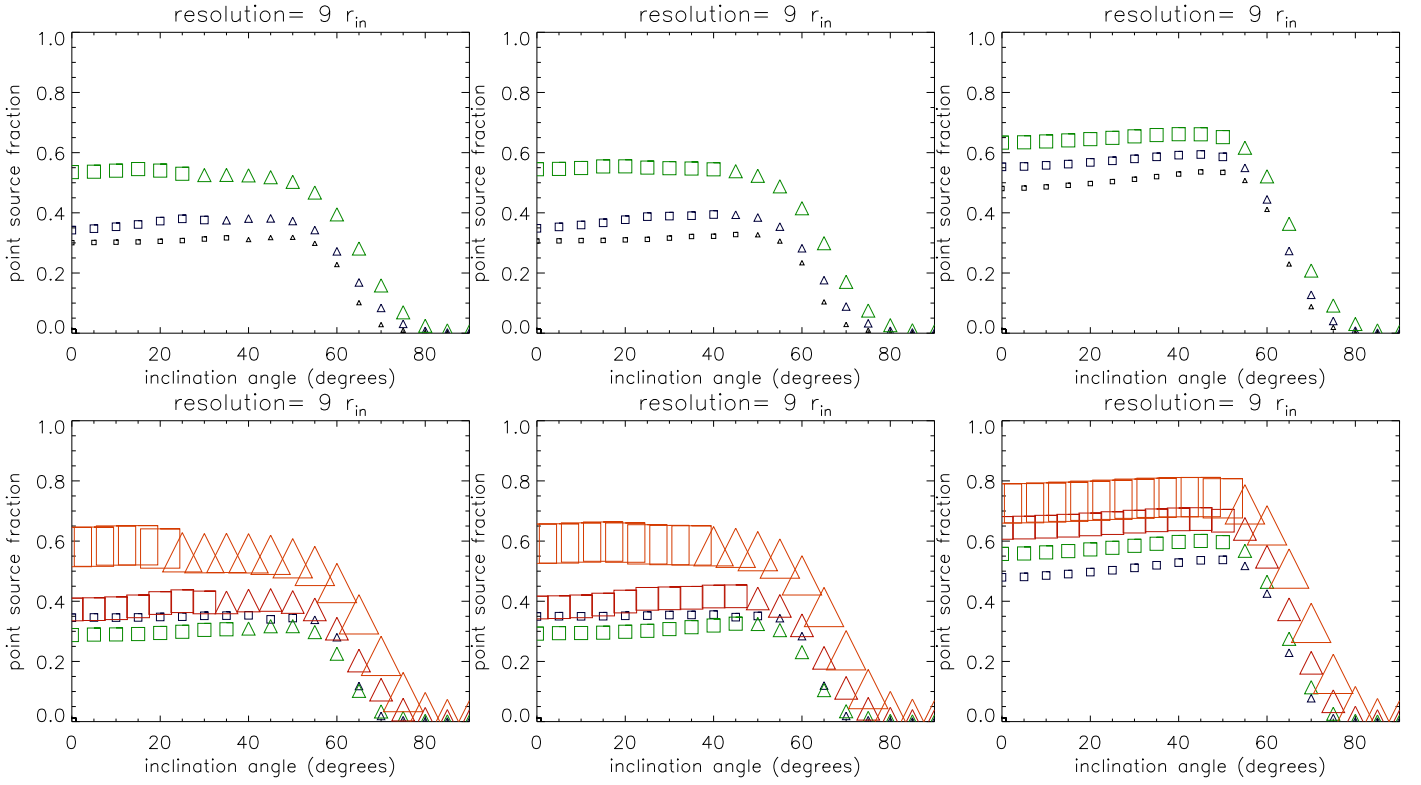


Fig. C.1. Point source fraction ($9r_{in}$) for the Circinus model (upper row) and NGC 1068 model (lower row). *Left column:* $1/z$ wind (standard model); *middle column:* $1/z^2$ wind; *right column:* no wind. Boxes: type 1 objects; triangles: type 2 objects. The size of the symbols is proportional to the bolometric luminosity.

Appendix D: Model interferometry

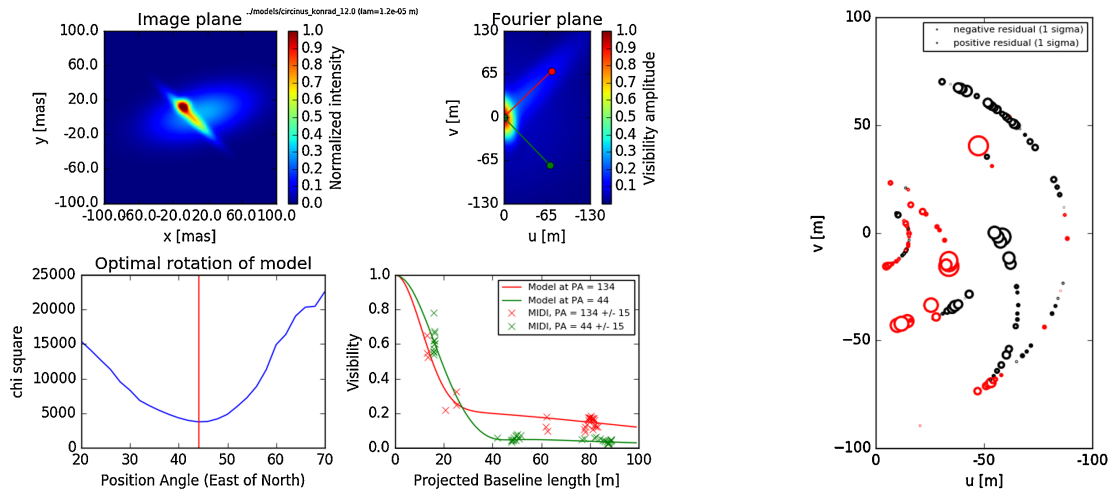


Fig. D.1. Tristram et al. (2014) Circinus model. *Upper left panel:* image at $12 \mu\text{m}$; *upper middle panel:* visibility amplitudes; *lower left panel:* χ^2 as a function of position angle; *lower middle panel:* visibility amplitudes as a function of projected baseline length (solid lines: model, crosses: observations); *right panel:* difference between the model and observed visibility amplitudes (red: (model-observations) > 0 , black: (model-observations) < 0). The size of the rings is proportional to the value of the residual.

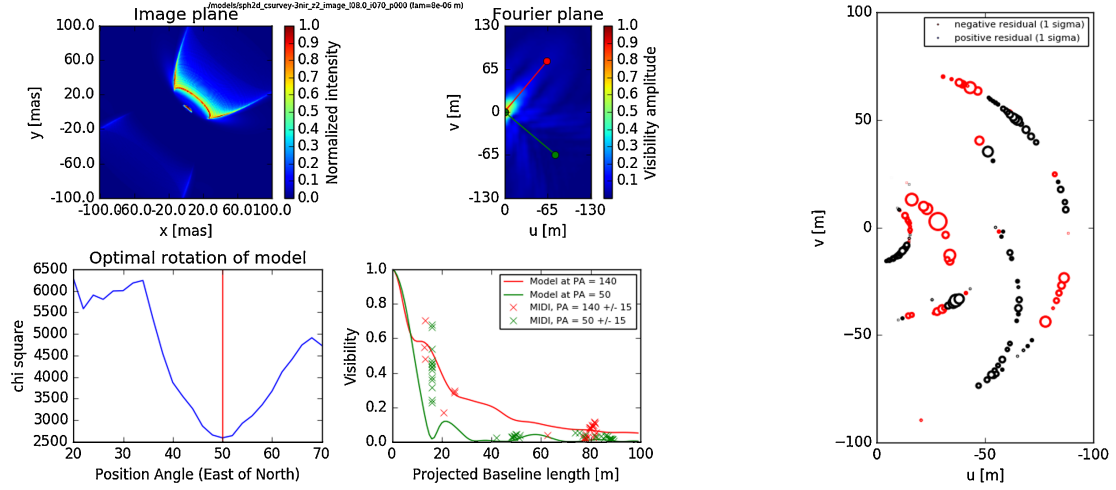


Fig. D.2. Same as Fig. 20 for the Circinus radiative transfer model at $8\ \mu\text{m}$.

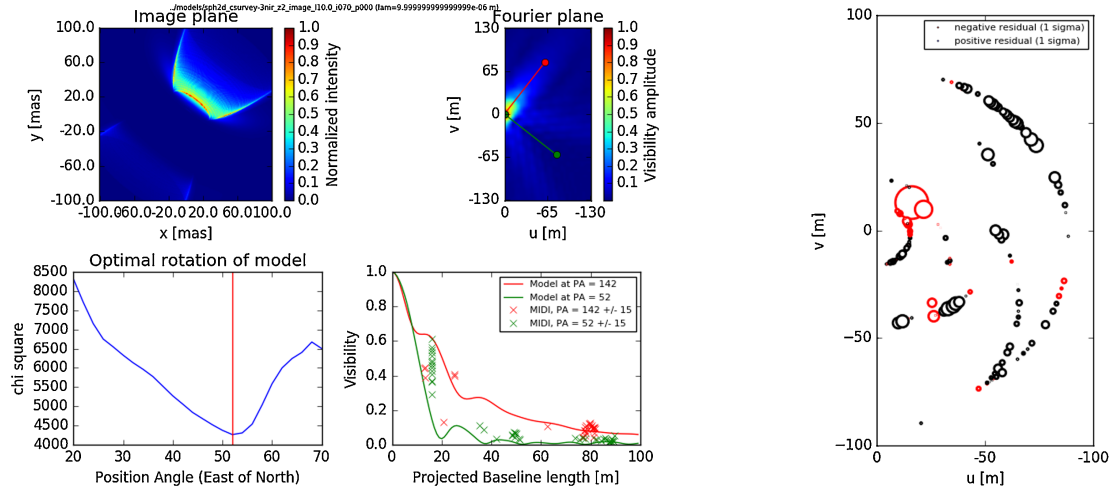


Fig. D.3. Same as Fig. 20 for the Circinus radiative transfer model at $10\ \mu\text{m}$.

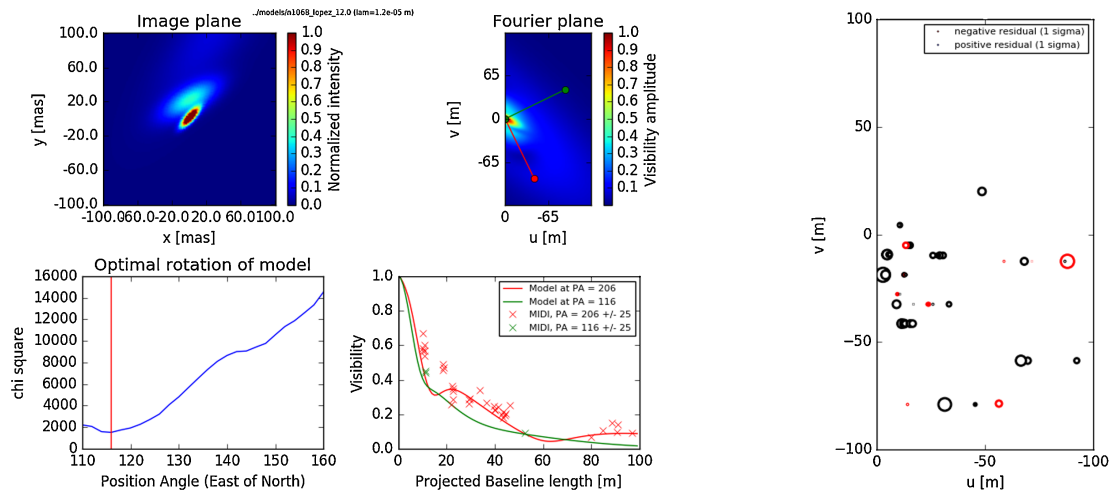


Fig. D.4. NGC 1068. Same as Fig. D.1 for the López-Gonzaga et al. (2014) NGC 1068 model. All three components are included. The third, extended component is barely visible in the *left panel*, but contributes to the visibilities at short baselines.

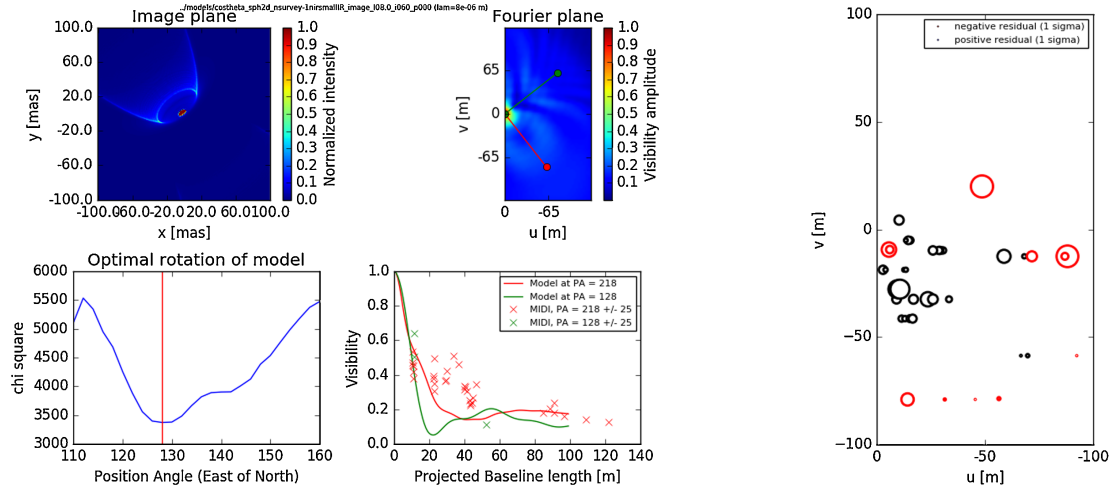


Fig. D.5. Same as Fig. 21 for the NGC 1068 radiative transfer model at $8\ \mu\text{m}$. The puff-up of the inner thin disk is located at $r = 3 \times r_{\text{sub}}$.

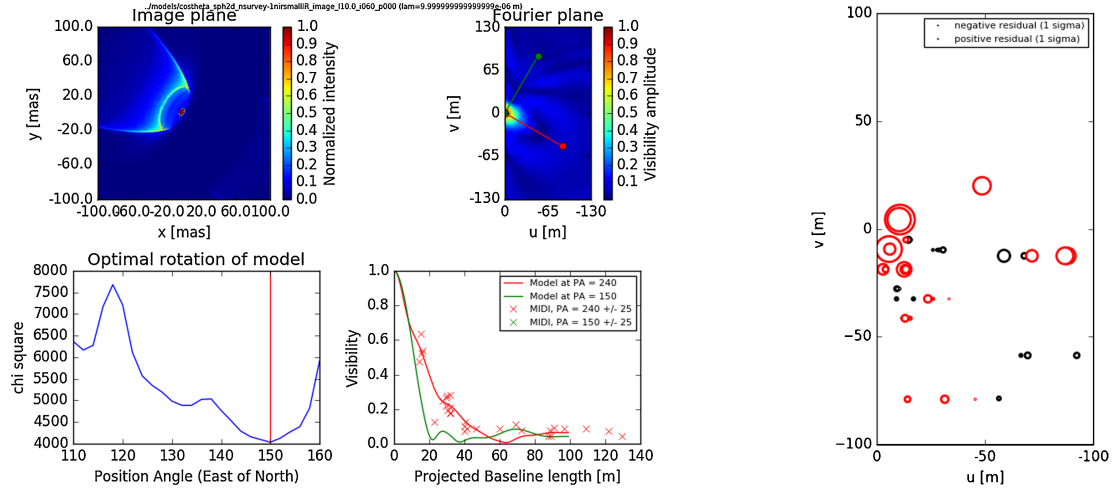


Fig. D.6. Same as Fig. 21 for the NGC 1068 radiative transfer model at $10\ \mu\text{m}$. The puff-up of the inner thin disk is located at $r = 3 \times r_{\text{sub}}$. There are no observed MIDI visibilities for a position angle of 150° .